SEISMIC ANALYSES OF THE CRUST AND MOHO BENEATH THE FORELAND FOLD AND THRUST BELT OF THE SOUTHERN URALS, RUSSIA

A Thesis

Presented to

The Graduate Faculty of The University of Akron

In Partial Fulfillment

of the Requirements for the Degree

Master of Science

Charles Spurr

December, 2015

SEISMIC ANALYSES OF THE CRUST AND MOHO BENEATH THE FORELAND FOLD AND THRUST BELT OF THE SOUTHERN URALS, RUSSIA

Charles A. Spurr

Thesis

Approved:

Advisor
Dr. David N. Steer

Faculty Reader
Dr. John A. Peck

Faculty Reader
Dr. Shanon Donnelly

Department Chair
Dr. James McManus

Accepted:

Dean of the College
Dr. Chand K. Midha

Interim Dean of the Graduate School
Dr. Chand K. Midha

Date

ABSTRACT

Analysis of reprocessed URSEIS'95 explosive source reflection data confirmed previous geophysical and geologic findings and provided new information about the crust and Moho beneath the Ural fold and thrust belt. Advanced reprocessing of the shot gathers generated an improved image of the crust and Moho that was used to more accurately interpret crustal structures and the geometry of the Moho. Velocity pushdown was eliminated as a major factor affecting the depth of the Moho. Manual migration of Moho reflections better constrained the depth and orientation of the Moho. Modelling of ray traces was used to confirm reflector associations. These analyses confirm the interpretations that the Moho dips east into the root of the Ural Mountains where it becomes non-reflective.

Laminated, laterally discontinuous Moho reflections imaged beneath the fold and thrust belt are interpreted to be the result of mafic sills emplaced during the Proterozoic. The dip of the Moho is interpreted to be the result of these sills being subducted and deformed along with the basement of the East European Craton during the Paleozoic collisional stage of Ural Wilson cycle. The transition from reflective to diffuse, non-reflective Moho has been identified beneath the fold and thrust belt. Furthermore, the non-reflective nature of the Moho closer to the root can be explained if the crust and sills were carried to depths greater than 50 km and converted into eclogite.

ACKNOWLEDGEMENTS

I would like to begin by thanking my thesis advisor, Dr. David N. Steer for offering me this project and providing insite throughtout the entire process. I greatly appreciate the myriad of meetings and revisions he has provided during my thesis track.

I would like to thank my committee members Dr. John Peck and Dr. Shannon Donnelly for being readers, providing knowledge, and offering advice that would improve my thesis. I also greatly appreciate the advice offered to me by Dr. Caleb Holyoke and all of the technical assistance from Thomas Quick. I would also like to thank the geoscience department's administrative assistant, Elaine Butcher for help with my thesis formatting, class and meeting scheduling, and offering advice along the way.

In addition, I would like to thank my peers and fellow University of Akron graduate students for all of their help and support over the last 2 years. I want to especially recognize Carl Medvid, Mike Anderson, Chris Biro, and Stephanie Mitchell.

Lastly, I want to thank my family and friends for everything they have done for me. Their encouragement and support has helped me attain my goals.

TABLE OF CONTENTS

Page

LIST OF FIGURES

LIST OF TABLES

CHAPTER I

INTRODUCTION

Studying a well preserved orogen provides geoscientists an opportunity to learn more about its geologic history and process of formation. The Uralian orogeny in Russia is an example of a late Paleozoic collision of the East European craton, the Siberian craton, and other accreted terrains (Hamilton, 1970). The cratons and associated terrains that comprise the Urals appear to have remained relatively intact since they formed, thus providing a chance to study the tectonic evolution of the continents and their structural features (Juhlin et al., 2007).

In order to evaluate the deep structure and tectonic history of the Ural Mountains, several geologic and geophysical experiments were completed during the mid-1990's (Brown et al., 2008). A combination of wide angle seismic and reflection seismic experiments imaged the crust and upper mantle providing information about the transition between the crust and the mantle (i.e. Moho) and evidence of a preserved crustal root in the Ural Mountains (Berzin et al., 1996; Carbonell et al., 1996; Echtler et al., 1996; Knapp et al., 1996; Steer et al., 1996). The seismic experiments were backed by additional surface geology, thermochronology, and geochronology studies that assisted in constraining the tectonic evolution of the Urals (Brown et al., 1997; Perez-Estaun et al., 1997). Specifically, the URSEIS (Ural Reflection Seismic Experiment and Integrated Studies) was completed across the southern Urals (Figure 1) and provided a remarkable image of the Moho beneath this portion of the mountains (Steer et al., 1996). According to the reflection experiment, the southern Ural Mountains appear to have a well preserved

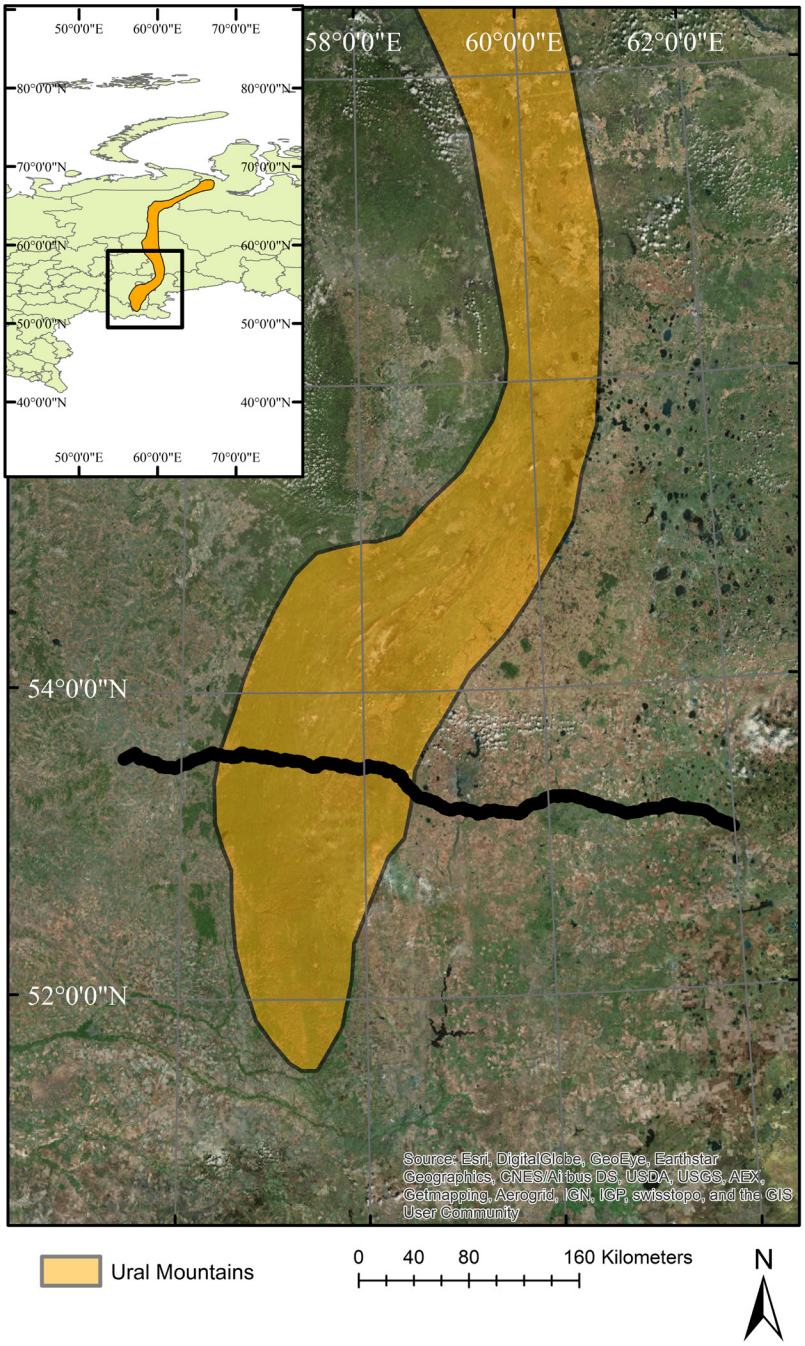

Figure 1. A terrain map showing the location of the URSEIS transect in the southern Ural Mountans, Russia.

suture and an apparent lack of widespread extensional features (Steer et al., 1998). The southern Urals are unlike other Paleozoic mountains chains that experienced later extension during their post-orogenic breakup phases (Alvarez-Morrron, 2002).

Based on age constraints, the Ural Mountains formed at approximately the same time as the Appalachian and Variscide orogens. However; the Appalachians and Variscides have since undergone a cycle of post mountain building collapse (Cook et al., 1979; Meissner et al., 1987). This process of mountain building and collapse (Figure 2) which involves the closure and opening of ocean basins is known as the Wilson cycle (Fichter, 2000). The Urals have an intact structure which is similar to those observed in stable cratons such as the Baltic and Canadian shields where the crustal roots appear to be preserved based on topographic relief and deep Moho boundaries with a depressed nature (BABEL Working Group, 1990; Henstock et al., 1998). In contrast, the Appalachian's and Variscide's collapses are interpreted based on a flat, shallow Moho and the Atlantic Ocean basin that formed in between (Cook et al., 1979; Meissner et al., 1987; Nelson et al., 1987). The difference between collapsed and intact orogens can be seen when comparing their crustal structure such as that of the southern Urals and the Appalachians (Figure 3). The crustal material in the mountains may differ but similarities are observed when comparing the overall structure of the modern Urals to the ancient Appalachians. Furthermore, the geometry of the Moho especially appears to differ based on the state of the orogeny (i.e., modern Urals versus modern Appalachians). The Moho in the modern Appalachian basin is interpreted to be relatively flat, only shallowing toward the oceanic crust, whereas the Moho in the southern Urals is depressed and becomes deeper into the crustal root (Berzin et al., 1996; Marshak, 2011).

The state of the Moho imaged throughout the Southern Ural Mountains, like the Moho interpreted beneath the Alleghenian Orogeny (Figure 3), appears preserved since Paleozoic times. Original processed URSEIS reflection data from the fold and thrust

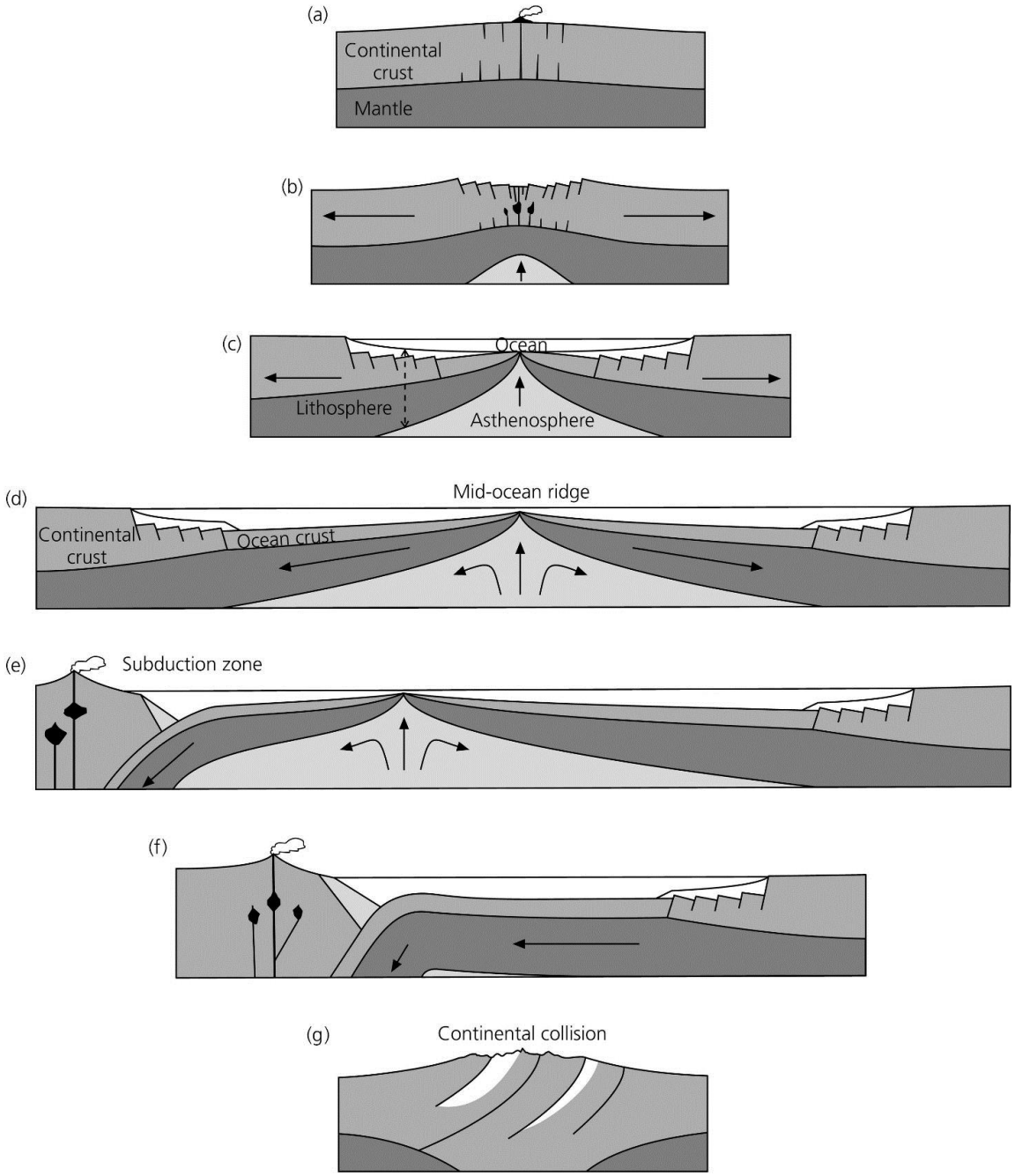

Figure 2. Events that occur during the Wilson Cycle. (a) Crust prior to rifting (b) Rifting, faulting, and subsidence (c) Seafloor spreading begins. (d) The ocean basin grows, sediments are deposited. (e) New subduction begins to close ocean basin. (f) Rift is subducted and landmasses converge (g) the landmasses collide to form a mountain range. The new combined landmasses should eventually collapse and repeat the cycle. A full cycle is complete once a new ocean basin has formed (modified from Stein, 2014).

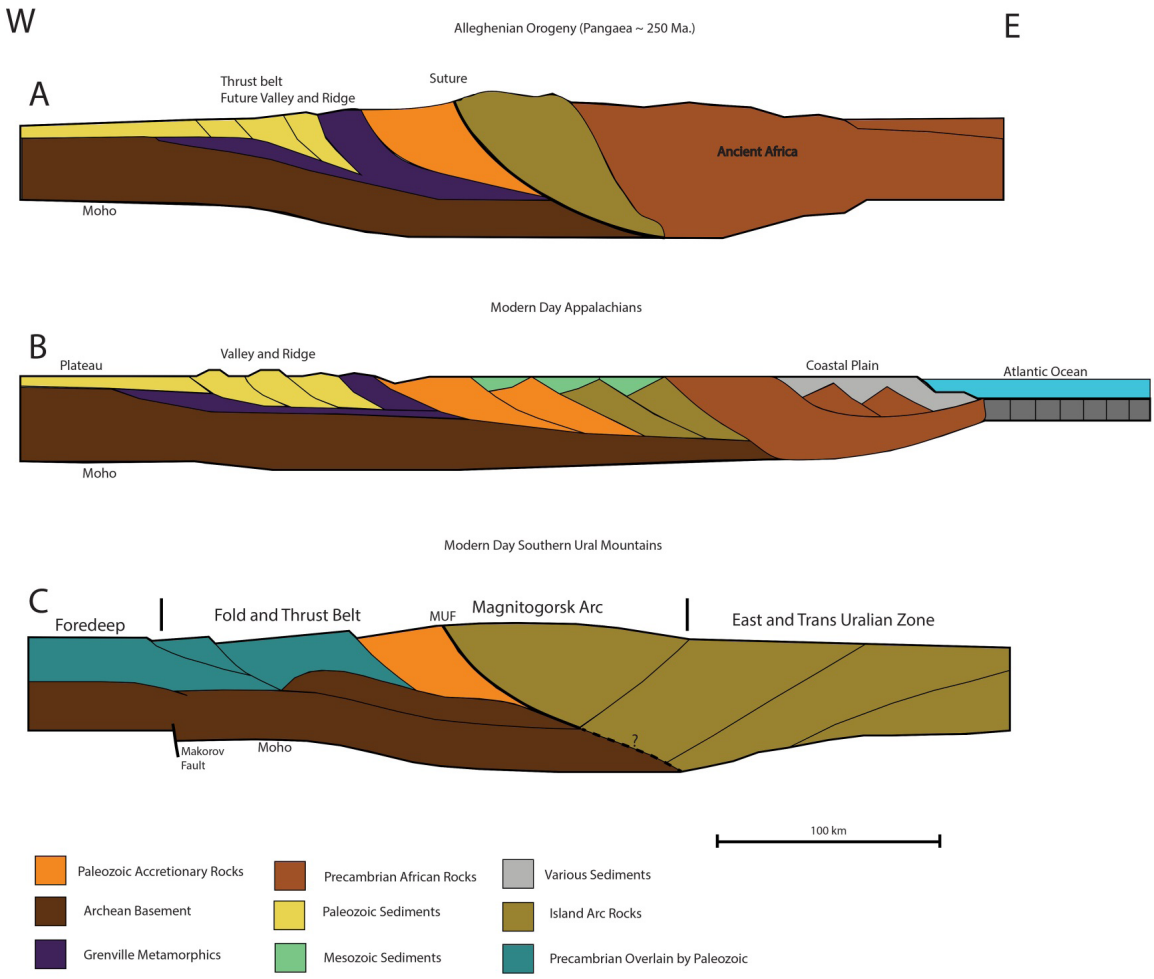

Figure 3. The different crustal structure and Moho of the Appalachians and southern Urals. A) An interpreted structure of the Appalachians from Pangaea ~250 Ma after the Alleghenian orogeny. Note the high relief, suture, and deep crustal root. B) Modern structure of the Appalachians. Notice the reduced relief, relatively flat, shallow Moho, and Atlantic Ocean to the east. C) Interpretation of the modern day southern Urals. Note the crustal root, Main Uralian Fault (MUF) suture, and deep Moho. Additionally note how the modern Urals (C) and ancient Appalachians (A) appear to have similar overall geometry (After Berzin et al., 1996; Marshak, 2011)

belt shows a deep, curved Moho interpreted as part of the southern Ural's eclogitized crustal root (Berzin et al., 1996; Knapp et al., 1998; Steer et al., 1998). Reprocessing of the seismic data was intended to provide new information about the Moho beneath the fold and thrust belt that would aid in new interpretations and improve the overall understanding of the tectonic evolution of the southern Urals.

Study Area

The Ural Mountains are a north-south oriented mountain chain which extends over 3000 km from the Kara Sea in the North to the Caspian Sea in the south (Figure 4). The Urals display a characteristic west–east zonation of a collisional orogeny, similar to that of the entire Ural Mountain chain (Puchkov, 2013). The southern Urals contain many well defined rock outcrops, modest elevations less than 1500 meters above sea level (a.s.l), and low structural disruptions (i.e. gentle hills, low relief) which are characteristics that are particularly suitable for both structural and geophysical studies (Spadea and D'Antonio, 2006). Studies done in the Urals separate the mountains into six longitudinal zones that are categorized by their tectonic units which include the Uralian Foredeep, West-Uralian zone, Central-Uralian zone, Main Uralian fault, Tagil-Magnitogorsk zone, East Uralian zone, and Trans-Uralian zone (Sokolov, 1992; Puchkov, 2013). Among these zones, the west and central encompass the fold and thrust belt in the Southern Urals west of the Main Uralian fault (Figure 5). The fold and thrust belt runs perpendicular to the front of the orogeny and continent arc suture where it widens to 120 km and becomes a west verging, imbricated basement stack that terminates to the South of the Ziliair Nappe and Kraka Klippe (Figure 5). Closer to the Zilair Nappe and Kraka Klippe, the thrust belt thins to 20 km, becomes less deformed, and poorly exposed (Brown et al., 1999).

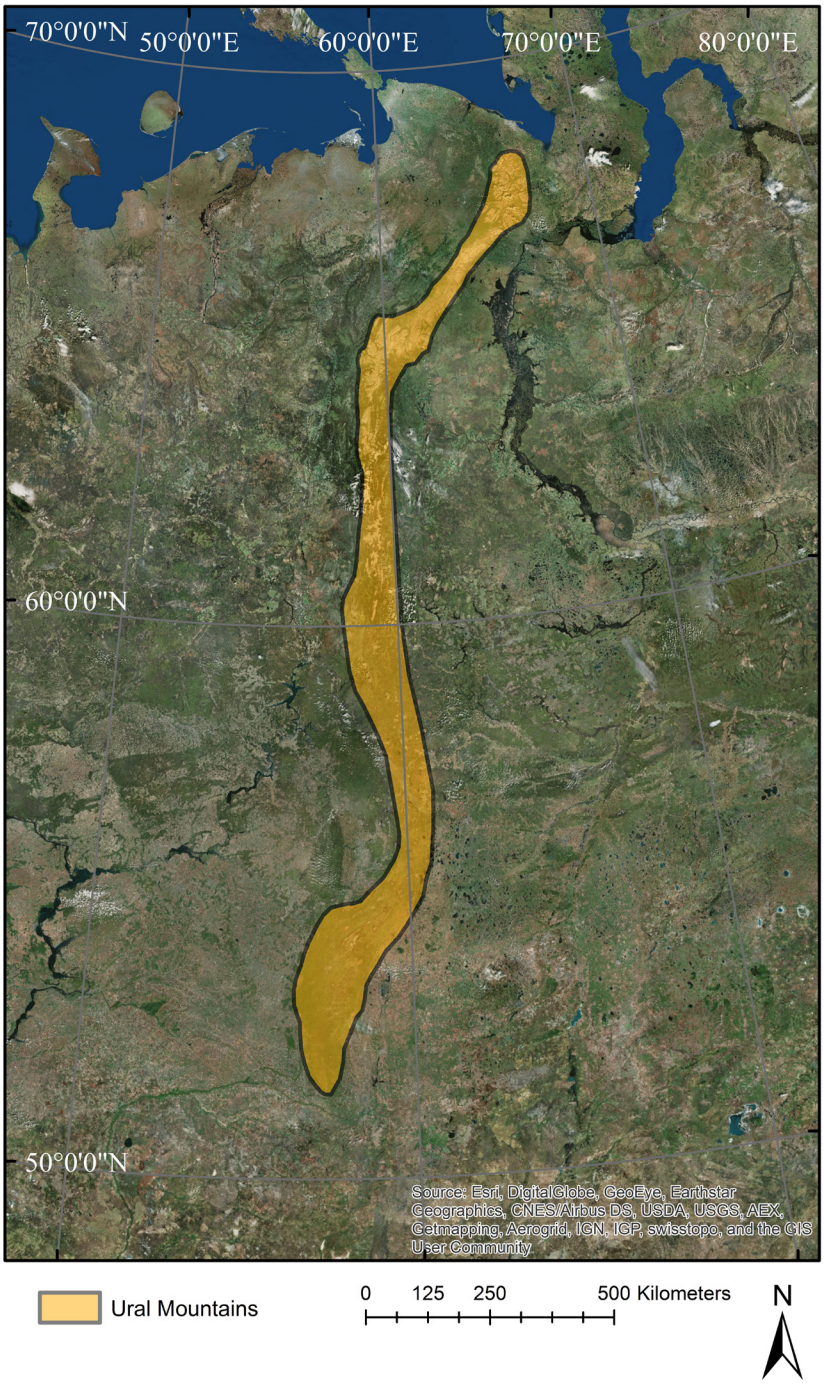

Figure 4. A terrain map showing the location of the Ural Mountains in Russia.

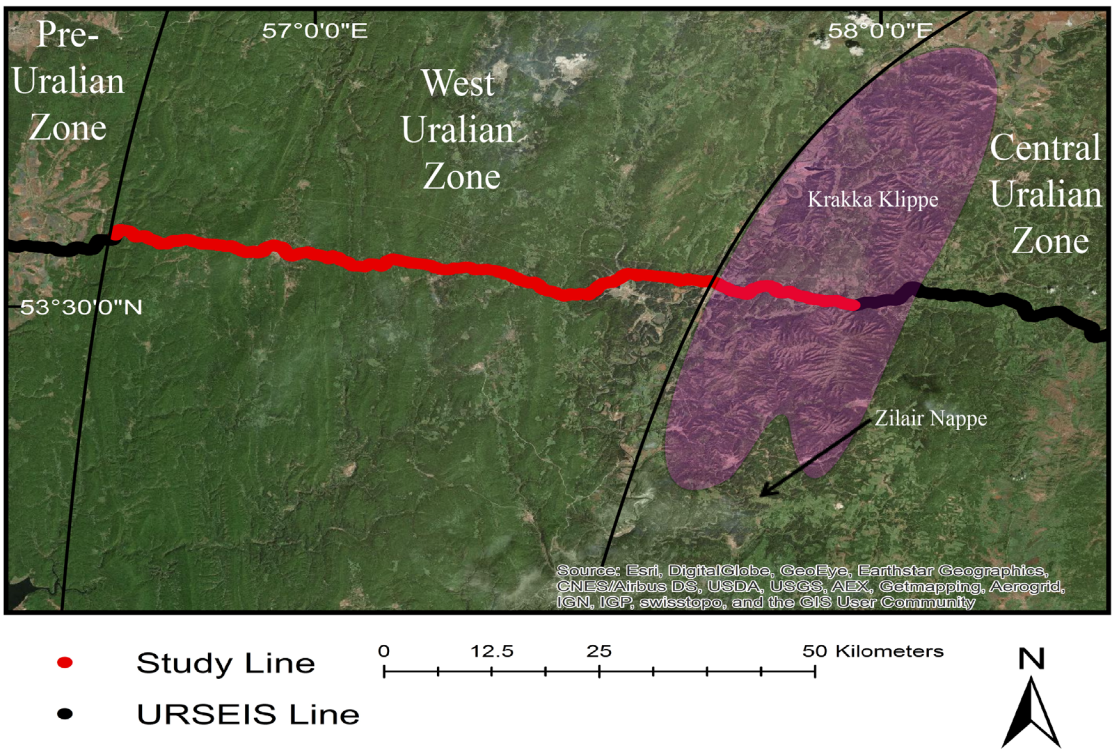

Figure 5. The study line located in the fold and thrust belt of the southern Ural Mountains. The tectonic zones and URSEIS transect are shown. The Kraka Klippe and Zilair Nappe (rock units exposed south of the klippe) are highlighted in the Central Zone.

Tectonic History

The structural units observed in the fold and thrust belt are well preserved and have provided sufficient information for geologists to reconstruct the Ural's tectonic development from intra-oceanic convergence in the early Paleozoic to an arc–continent collision in the late Paleozoic (Spadea and D'Antonio, 2006; Puchkov, 2013). Prior to the intra-oceanic convergence, continental rifting, continental breakup, and seafloor spreading during the early Paleozoic created the passive continental margin of Baltica; now known as the East European craton (Kashubin et al., 2006). The later tectonic events that built the Ural Mountain belt, including intra-oceanic convergence in the early Devonian to the final continental collision in the late Permian, are consistent with the stages of the Wilson cycle (Puchkov, 2013).

Mountain building in the Urals occurred in various stages similar to those of the Wilson Cycle (Figure 6). The first two pertinent stages involved the rifting of Baltica and the formation of a passive margin and ocean basin in the Ordovician (Puchkov, 2013). This was followed by closure of the Paleo-Ural Ocean began in the Early Devonian (Figure 6.A). Eastward subduction of the oceanic crust east of Baltica created the Magnitogorsk arc during the early Devonian (Matte, 2006). Eventually, subduction of the oceanic crust to the east closed the Paleo-Ural Ocean and accreted the Magnitogorsk Volcanic arc onto Baltica (Brown et al., 2004). Subduction of the Baltic continental crust (Figure 6.B) beneath the Magnitogorsk arc continued into the late Devonian after the collision with Baltica (Chemenda et al., 1997; Puchov, 2013). Deep subduction of the continental crust during the late Devonian (Figure 6.B) caused failure of the crust which began to detach into a slab (Chemenda et al., 1997). The subducting continental crust also caused an underthrusting of the Magnitogorsk arc which descended into the mantle while

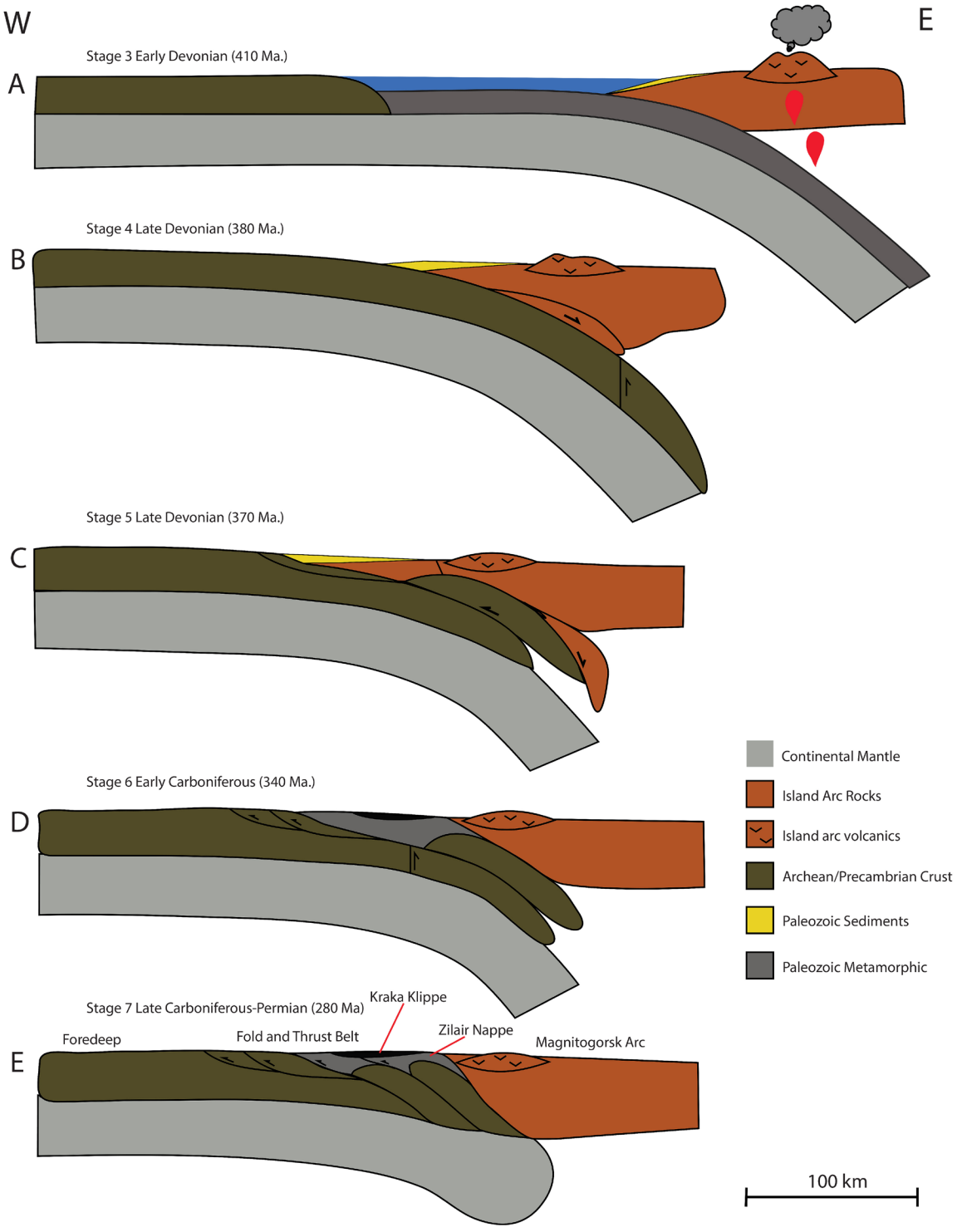

Figure 6. Evolutionary tectonic model for southern Urals located within the region of the fold and thrust belt. (Based on Chemenda et al., 1997; Matte, 2006; Puchkov, 2013). Each stage represents a portion of the Ural Wilson Cycle.

scraping off crust and mantle slivers in front of the arc (Chemenda et al., 1997; Matte, 2006).

Exhumation of a continental slab occurred during the late-collisional stage (Figure 6.C) that began in the Late Devonian (Chemenda et al., 1997). The exhumed slab combined with mantle slivers and crust, contacted overlying arc rocks and sediment, and began to build and deform to the west of the Magnitogorsk arc (Chemenda et al., 1997;). Exhumation of a second continental crust slab (Figure 6.D) is part of the later stage and occurred in the Early Carboniferous (Chemenda et al., 1997). This stage also involved activation of west verging thrusts which were responsible for deforming and metamorphosing the Paleozoic accretionary wedge and allochthons (Krakka Klippe; Zilair Nappe) west of the Magnitogorsk arc (Brown et al., 1997; Chemenda et al., 1997; Brown et al., 1999). Rocks in the accretion and thrust belt all deformed due to uplift, faulting, and the west verging thrusts during the late Devonian and Carboniferous (Brown et al., 1997; Puchkov, 2013). The majority of deformation in the thrust belt was attributed to the collision processes reactivating faults that existed in the Precambrian rocks prior to formation of Uralide structures (Perez-Estaun et al., 1997; Brown et al., 1999).

The final stage of Ural Mountain building in the Permian (Figure 6.E) resulted in what is essentially the modern state of the fold and thrust belt. Accretionary complexes (Krakka Klippe; Zilair Nappe) are now underlain by both of the deformed continental crust slabs and the boundary between the crust and mantle (Moho) appears to be flexed beneath the fold and thrust belt (Berzin et al., 1996; Matte, 2006).

As a result of the mountain building, the modern overall structural architecture of the thrust and fold belt is that of a West verging, basement cored imbricate thrust system (Brown et al., 2004). The crust in the fold and thrust belt is thought to be comprised of the East European Archean basement rocks beneath nearly 19 km of highly deformed Riphean and Vendian rock much older than the orogeny (Skripiy and Yunusov, 1989).

Furthermore, the Precambrian and Paleozoic strata in the accretion to the east are comprised of metamorphosed continental margin sediments, ophiolite massifs, and high pressure rocks overlain by Lower Carboniferous sediments (Zonenshain et al., 1990; Brown et al., 1997; Tryggvason et al., 2001; Diaconescu and Knapp, 2002; Brown et al., 2008).

Data Acquisition

The data used in this study were collected during the URSEIS'95 project. The study was completed along a 465 km transect in the southern Urals located at latitude 54^{o} N that crossed perpendicular to the mountains (Steer et al., 1996). An Input-Output seismic data system (model II) with 360 channels was used to record the data in a roll along configuration (Figure 7.A). Each station consisted of a group of ten geophones in an array designed to reduce ground roll. The geophone groups were placed at 50 m spacing providing an 18 km total recording spread. The seismic charges ranged from 40-160 kg but were nominally 80 kg. The first shot was detonated on one end of the line and recorded for 68 seconds with a 4 millisecond sampling rate (Figure 7.A, shot 1). This was followed by a second shot detonated on the opposite end of the same line and recorded for another 68 seconds (Figure 7.A, shot 2). The acquisition line was then moved three kilometers (Figure 7.A, black line) and the same shot process was repeated for the next two shots (Figure 7.A, shot 3 and 4). This process was repeated every 3 kilometers along the entire length of the URSEIS study line (Steer et al., 1998).

Over 70 shots along nearly 100 km of the URSEIS transect were detonated within the fold and thrust belt, imaging both the crust and mantle to depths of at least 60 s TWT. Due to terrain limitations, the acquisition line throughout the fold and thrust belt was crooked (Figure 7.B) compared to the rest of the URSEIS acquisition line.

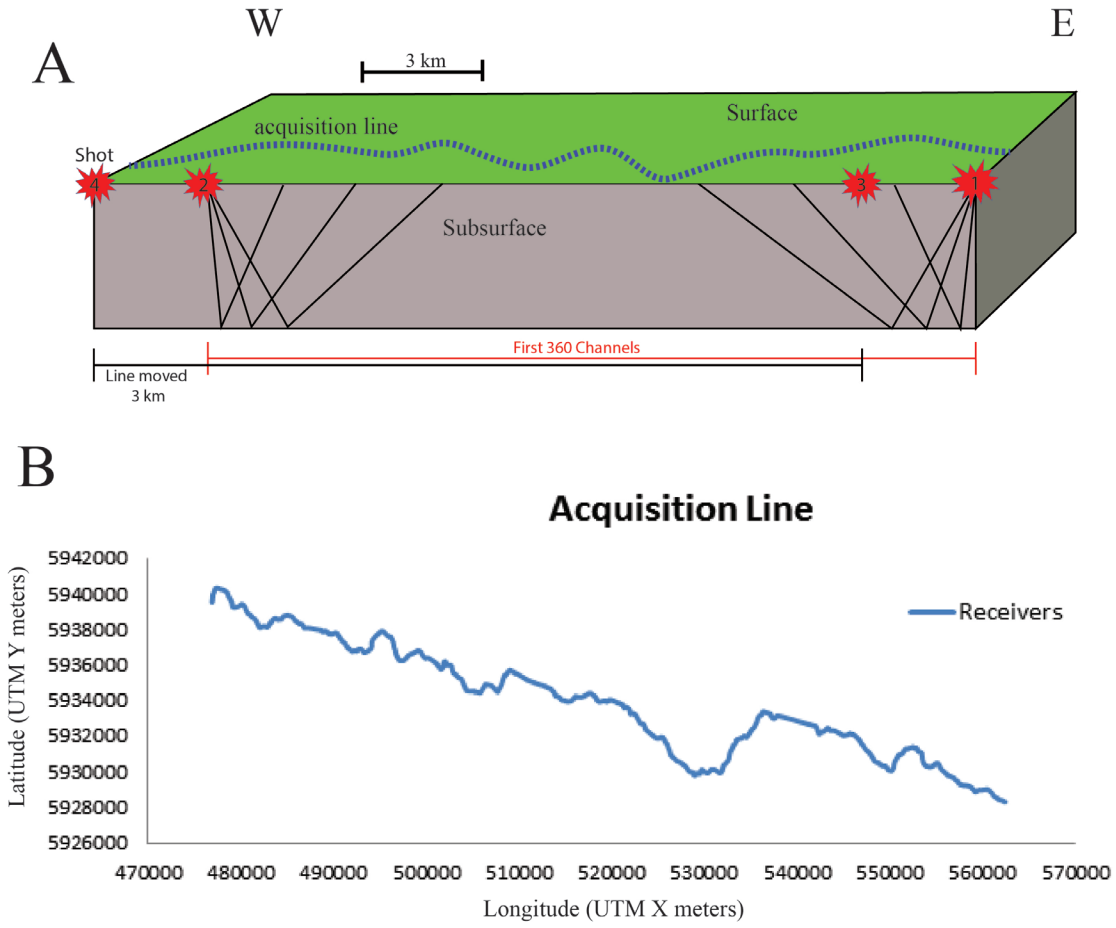

Figure 7. The method of data collection in the fold and thrust belt. (A) A diagram showing the roll along configuration used during the URSEIS'95 experiment. (B) A graph showing the aerial view of the geometry of the receiver line used in the fold and thrust belt. UTM X and Y coordinates for each receiver have been plotted.

CHAPTER II

METHODS

Seismic Reflection Processing

A total of 68 out of the 70+ shots imaging the fold and thrust belt were reprocessed in this study. The upper 20 seconds of each shot were used to ensure the entire crust and Moho were imaged. Noisy high amplitude traces were deleted, surgical mutes were applied where necessary, and top mutes were manually entered for each shot.

Several pre-stack and post-stack seismic reflection processing techniques were used to improve the image of the crust and Moho beneath the fold and thrust belt (Table 1).These processing techniques were conducted using GEDCO Vista 12.0.

Filtering and Amplitude Recovery

Filtering removes unwanted noise from the data (Yilmaz, 2001). A variety of Ormsby low and high pass filter frequencies, between the geophone cutoff of 5 Hz and the Nyquist frequency (62.5 Hz), were tested on each shot in order to determine frequency ranges that would most effectively enhance reflections and degrade noise. All test filters were applied one shot at a time and then compared side by side before moving to the next shot. A difference function compared each filters output to the unfiltered data in order to view changes made by the filter. One filter (10-15 45-55 Hz) which showed the optimum

Table 1. Seismic processing flow and associated parameters.

Processing	Parameters
Prestack	
Trace Editing	Noisy/dead traces
Surgical muting	Manually as needed
Top muting	Manually by inspection
Band-pass filtering	Ormsby 10 15 45 55 Hz
Automatic Gain Control	2500 milliseconds
F-K filter	Designed using F-K spectrum window
Time variant spectrum balance	5 Hz slope
Spherical Divergence	6.5 km/s
Refraction and Elevation Statics	6.5 km/s 350 m Datum
Crooked Line Binning	500 m X Bin
	40 m Y Bin
Spiking Deconvolution	40 ms operator length
Interactive velocity analysis	5500 - 8500 m/s
Residual Statics	Stack power optimization
Normal Moveout Correction	velocity function
CMP stack	No normalization
Post Stack	
F-X Deconvolution	Levinson-Durban
Kirchoff Migration	RMS velocity function

difference which most effectively removed noise without degrading reflectors was applied to all shots (Figure 8).

A user selected F-K spectrum filter was created using an interactive F-K spectrum window. A rejection window for the filter was created based on predicted F-K regions for typical groundroll (Figure 9). Original data was compared to F-K filtered data which verifies the removal of groundroll (Figure 10).

Automatic gain control (AGC) and spherical divergence were applied to recover lost amplitude and enhance reflections throughout the data (Yilmaz, 2001). The effects are best observed when comparing filtered data to data processed with these two techniques (Figure 11). AGC corrected for the difference between high amplitude first arrivals and weaker reflections in the lower crust by computing the mean absolute value amplitude of a trace within a specified time window (2500 ms) and multiplying the amplitude at the center of the window by the ratio of desired RMS amplitude to mean amplitude (Yilmaz, 2001). The 2500 ms window was chosen after first testing and comparing time windows between 500 and 5000 ms in steps of 500 ms. Spherical divergence was applied to recover amplitude lost by increasing depth using a velocity function that corrects the amplitude of wavelets that become degraded as the radius of the spherical source wave diverges further from the source (Yilmaz, 2001). A velocity of 6.5 km/s was chosen for the time constant velocity function based on Ural crustal velocities (Carbonell et al., 2000). Time variant spectrum balancing was applied to improve the gain of frequencies throughout the data, thus improving resolution of deeper reflections and removing some additional noise (Yilmaz, 2001). The effects of time variant spectrum balancing can be observed when comparing the data (Figure 12).

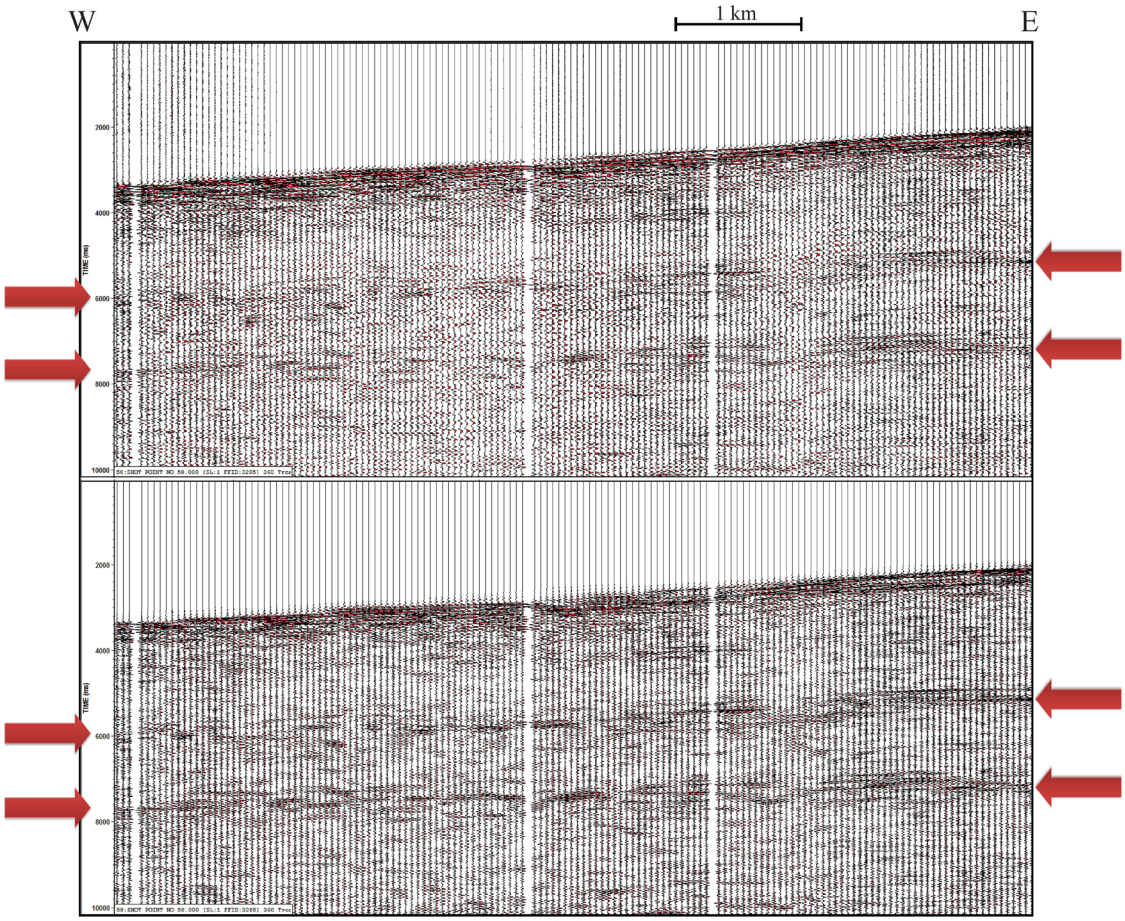

Figure 8. Unfiltered data (top) and data filtered (bottom) with a user selected Ormsby bandpass filter (10-15 45-55 Hz). Notice enhancement of deeper reflections (red arrows, bottom).

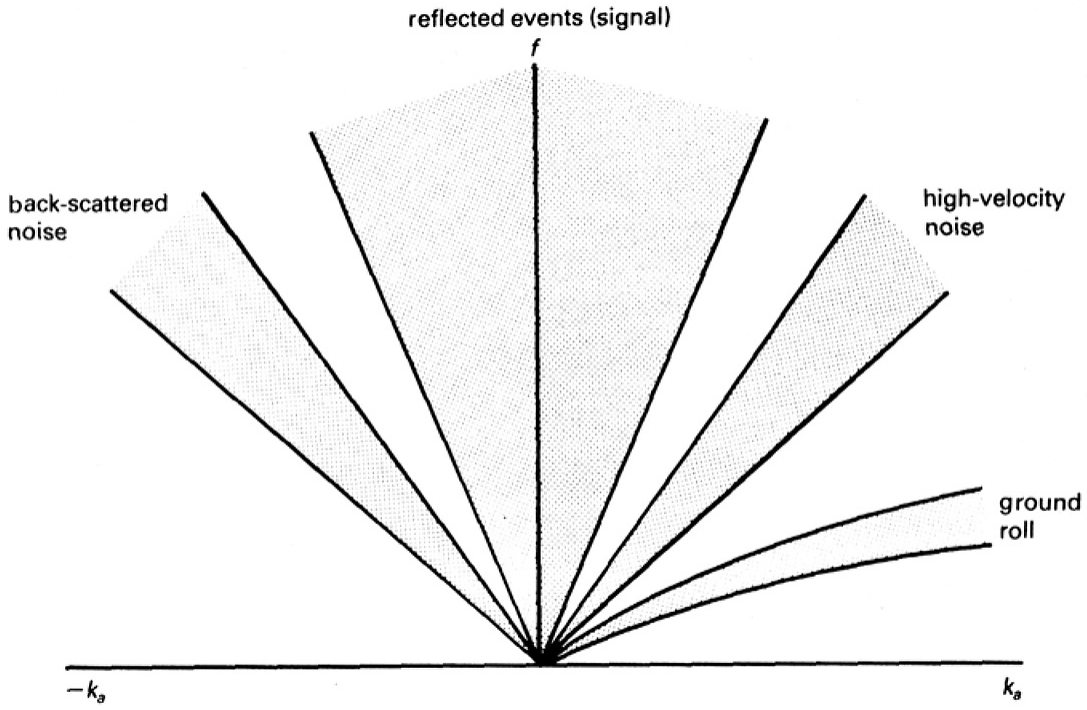

Figure 9. Relative locations of groundroll, high velocity noise, and back-scattered noise in an F-K spectrum window (from Marquez, 2014). This diagram was used as a guide to select the rejection window for the F-K filter.

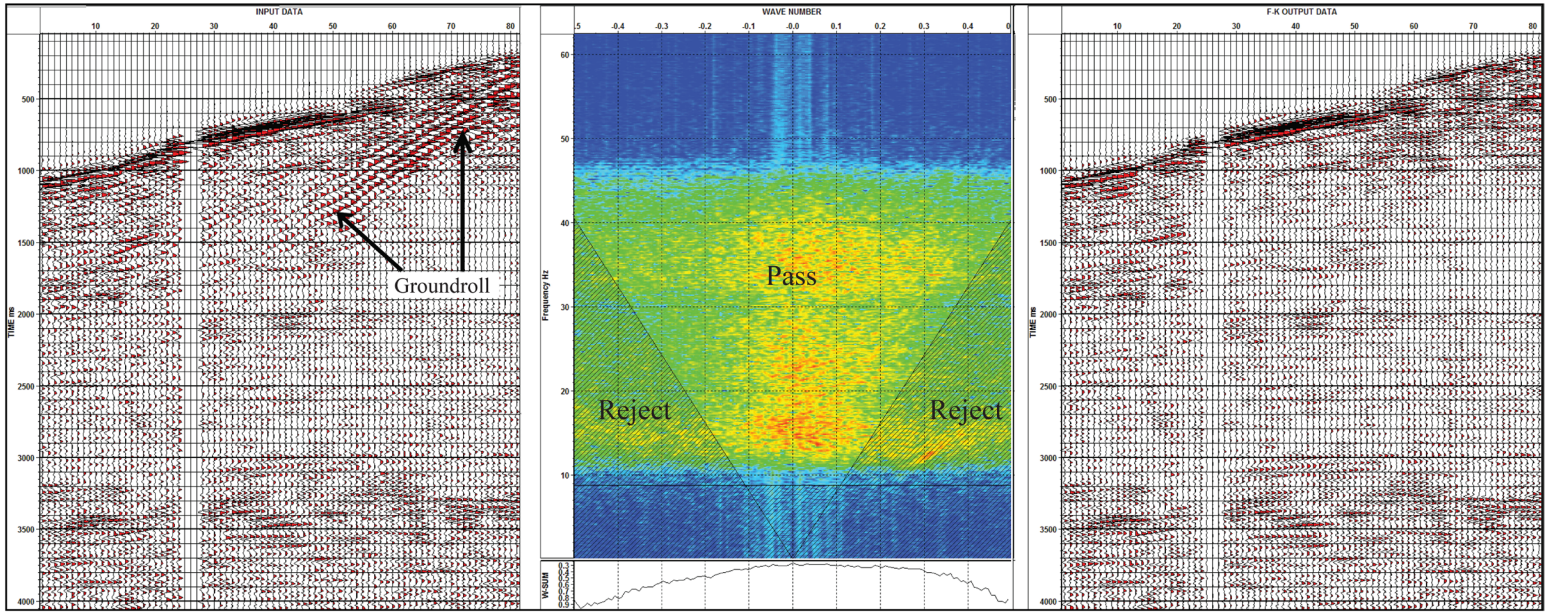

Figure 10. Removal of groundroll as a result of the applied F-K filter. (A) Raw data input. (B) The F-K spectrum with the user defined filter parameters. (C) Data output with F-K filter applied. Groundroll has been reduced.

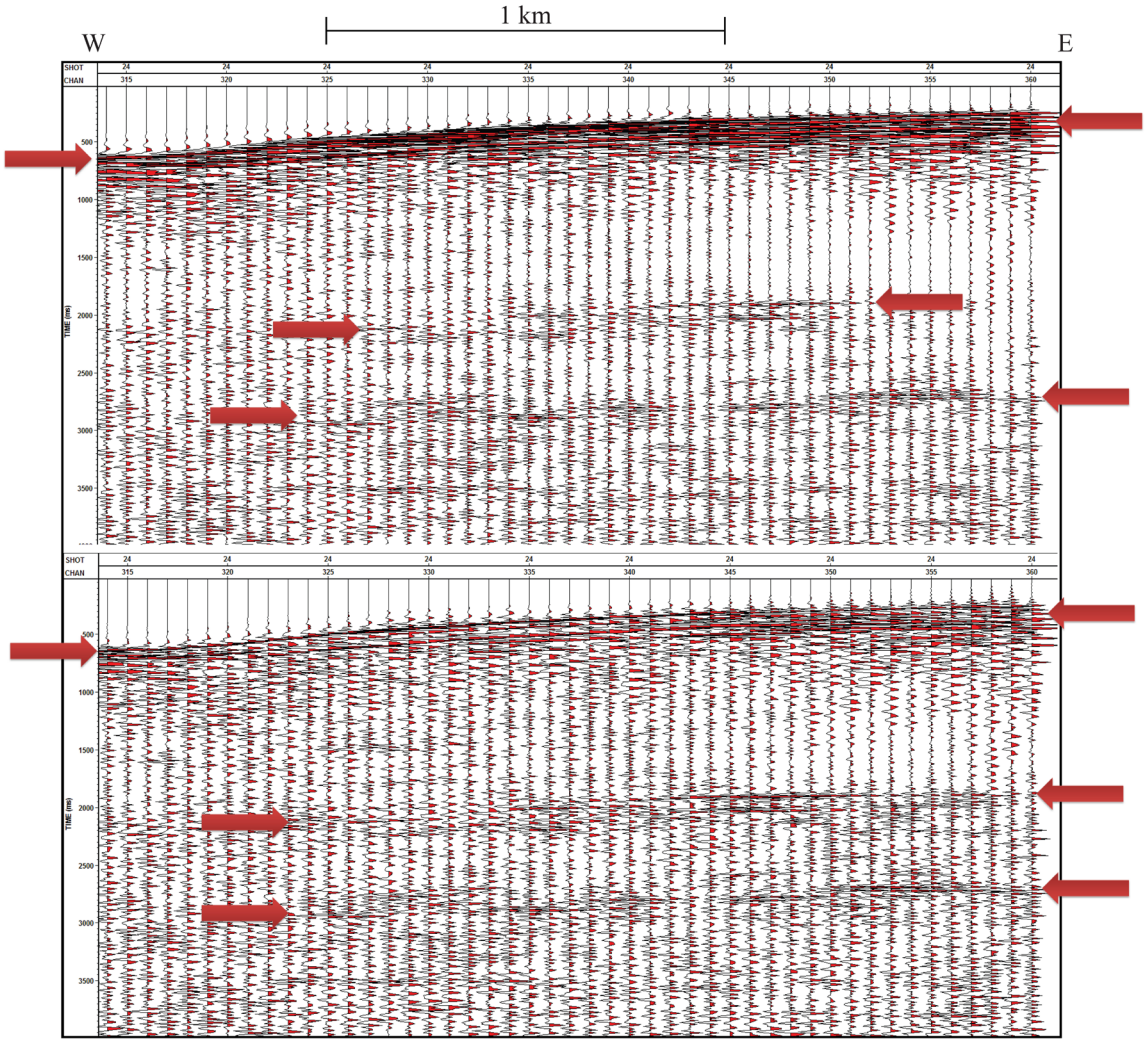

Figure 11. A comparison of filtered data (Top) to data that has also been corrected with AGC and spherical divergence (bottom). The amplitudes of first arrivals are reduced while deeper reflections are enhanced.

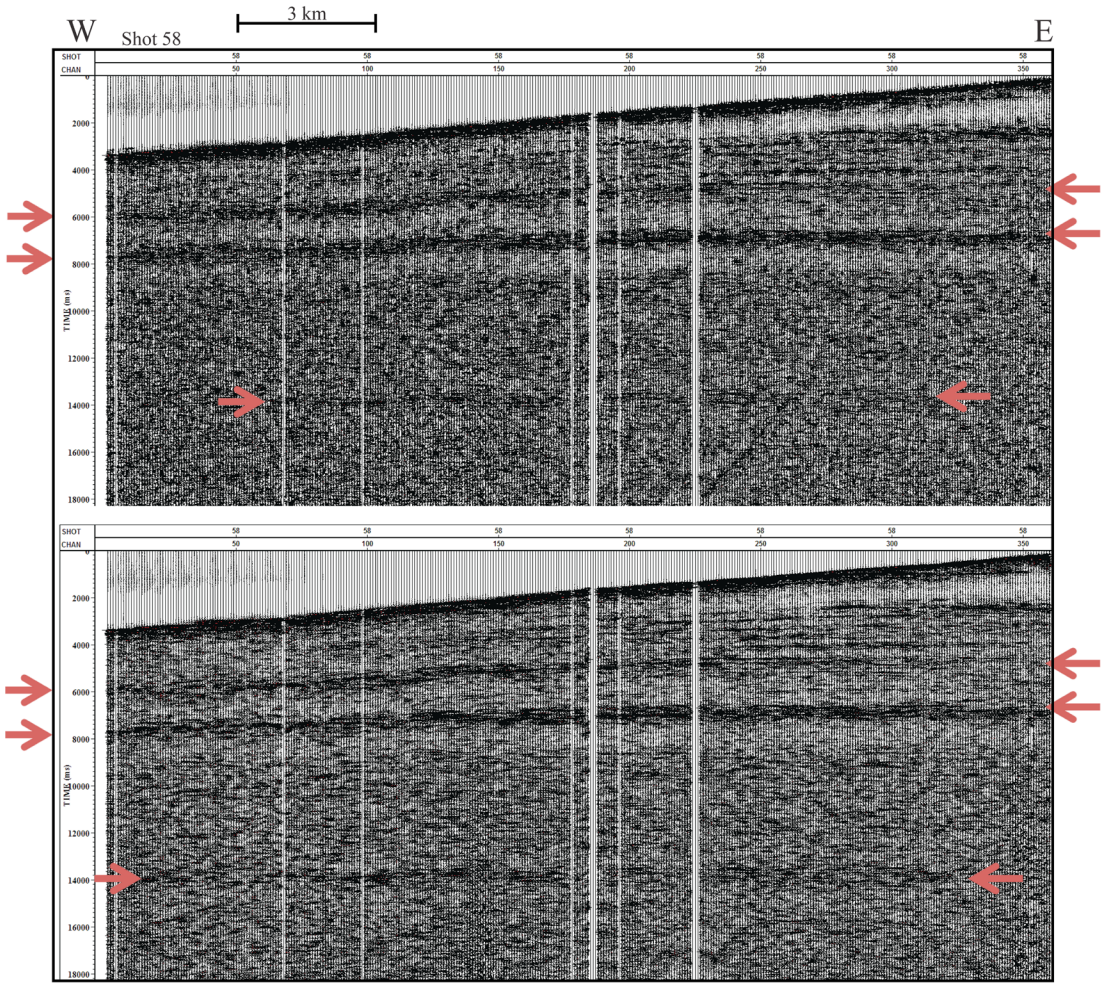

Figure 12. A comparison of filtered data to data that has been corrected with time variant spectrum balancing. Filtered data: top, spectrum balancing; bottom. Note the improvement in the deepest observed reflections.

Elevation Statics

Traces were adjusted in time by accounting for receiver, shot hole, and refraction static issues (Figure 13). The data must be adjusted along the time axis to account for elevation changes, near surface rock heterogeneity, and the effects of receiver offset on first arrivals and subsurface reflections (Yilmaz, 2001; Cox, 1999). The receivers and shots were placed on a fixed datum of 350 m a.s.l. A refraction replacement velocity of 6500 m/s was applied for the near surface weathering layer. First arrivals were manually chosen for each shot.

Crooked Line Binning

Crooked line binning was applied to account for the non-linear seismic acquisition that occurred in the fold and thrust belt. A first step in accounting for the crooked line was the construction of a slalom line in place of the original crooked line (Figure 14). A slalom line was created by first subdividing the original processing line into individual sections. Chords for the slalom line were drawn as best fit lines for each section of the processing line. The chords were connected and smoothed to act as a replacement processing line which is much straighter than the original acquisition line. A binning grid of 500 m length (Y) and 40 m width (X) was applied.

Deconvolution

Spiking Deconvolution compresses wavelets and removes multiples from the data which improves resolution and removes reverberatory energy (Yilmaz, 2001). Spiking

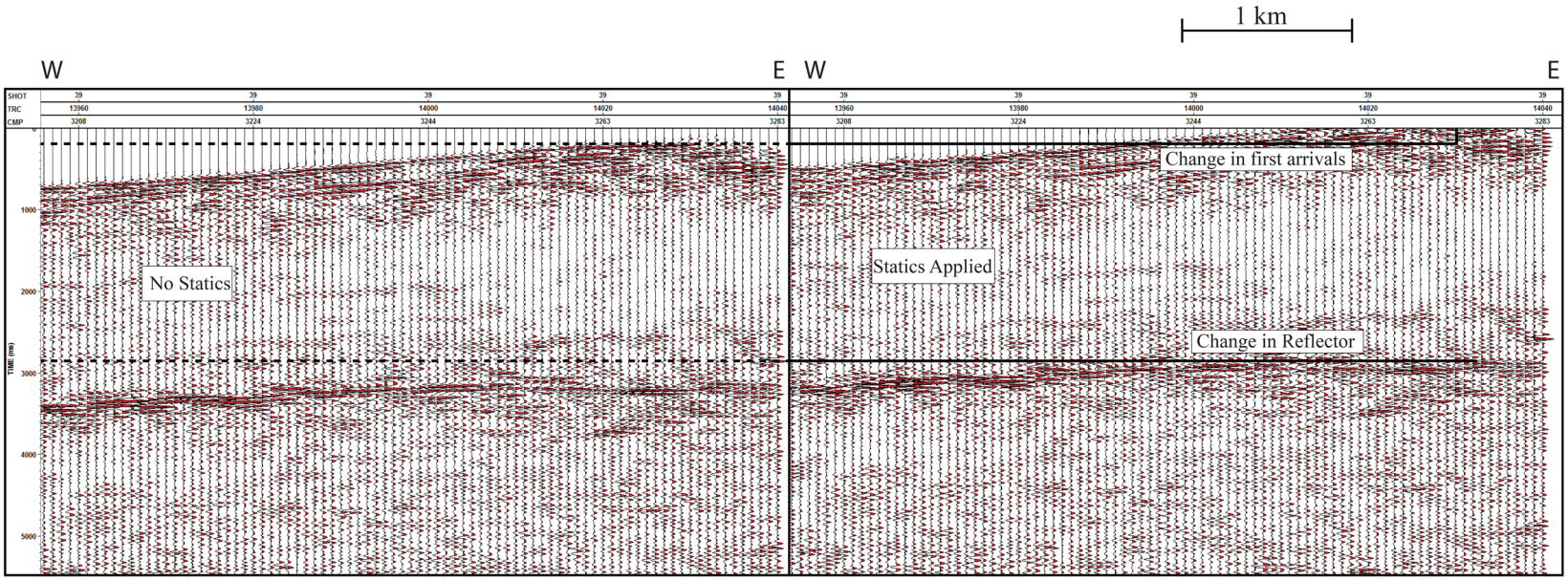

Figure 13. An example of seismic data with (left) and without (right) static corrections applied. Note the first arrivals and the reflector have been positioned closer to the surface with static shifts.

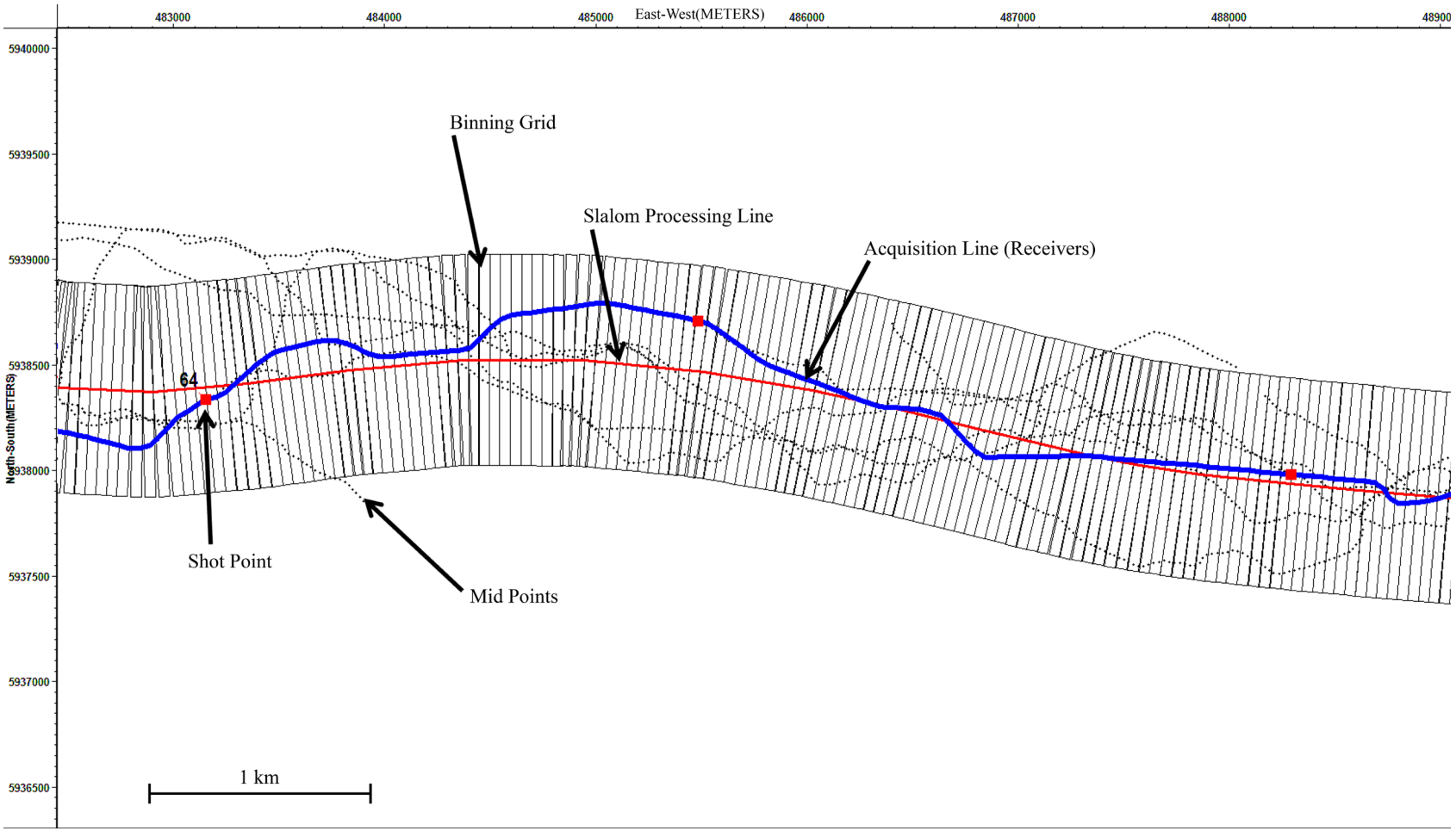

Figure 14. A section of the crooked line binning completed for the fold and thrust belt. The Binning grid, midpoints, acquisition line (blue), and slalom line (red) are shown.

deconvolution was applied with a Wiener-Levinson algorithm. A 40 milliseconds operator length and 150 ms time window were chosen with visual wavelet autocorrelation (Figure 15). Spiking deconvolution compressed wavelets and reduced reverberatory energy (Figure 16).

Velocity Analysis

Velocity analysis must be completed prior to stacking or migration (Yilmaz, 2001). A velocity function was generated by manually picking stacking velocities throughout all 68 shots (Figure 17). Velocities were picked in groups of 250 CMPs using semblance analysis. Stack power residual statics were applied twice in order to optimize the velocity function and to improve the quality of later completed stacked and migrated sections (Yilmaz, 2001). The velocity function was used for the normal move-out correction (Figure 18).

Stacking

Stacking is the process of combining several traces that image the same subsurface location (Yilmaz, 2001). Random noise is reduced by $1/\sqrt{n}$ where n is the number of traces being stacked and signal is increased. The data were nominally 6 fold but typically ranged between 2 and 5 fold.

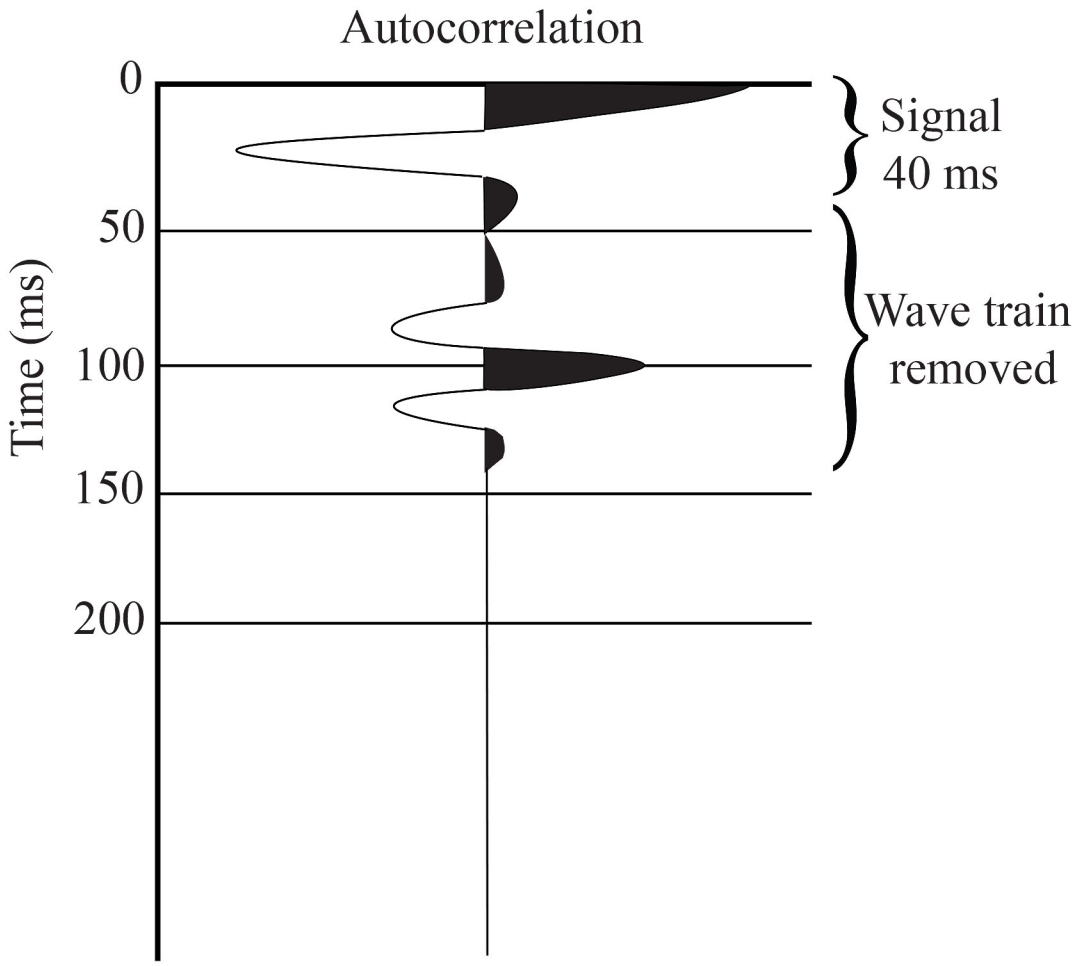

Figure 15. A traced image showing the use of wavelet autocorrelation in determining spiking deconvolution operator length and window length. The wavelet is normalized with its maximum at 0 ms time. The first 40 ms of the wavelet are determined to be the actual signal. The rest of the wavelet is determined to be ringing and the repeated signal.

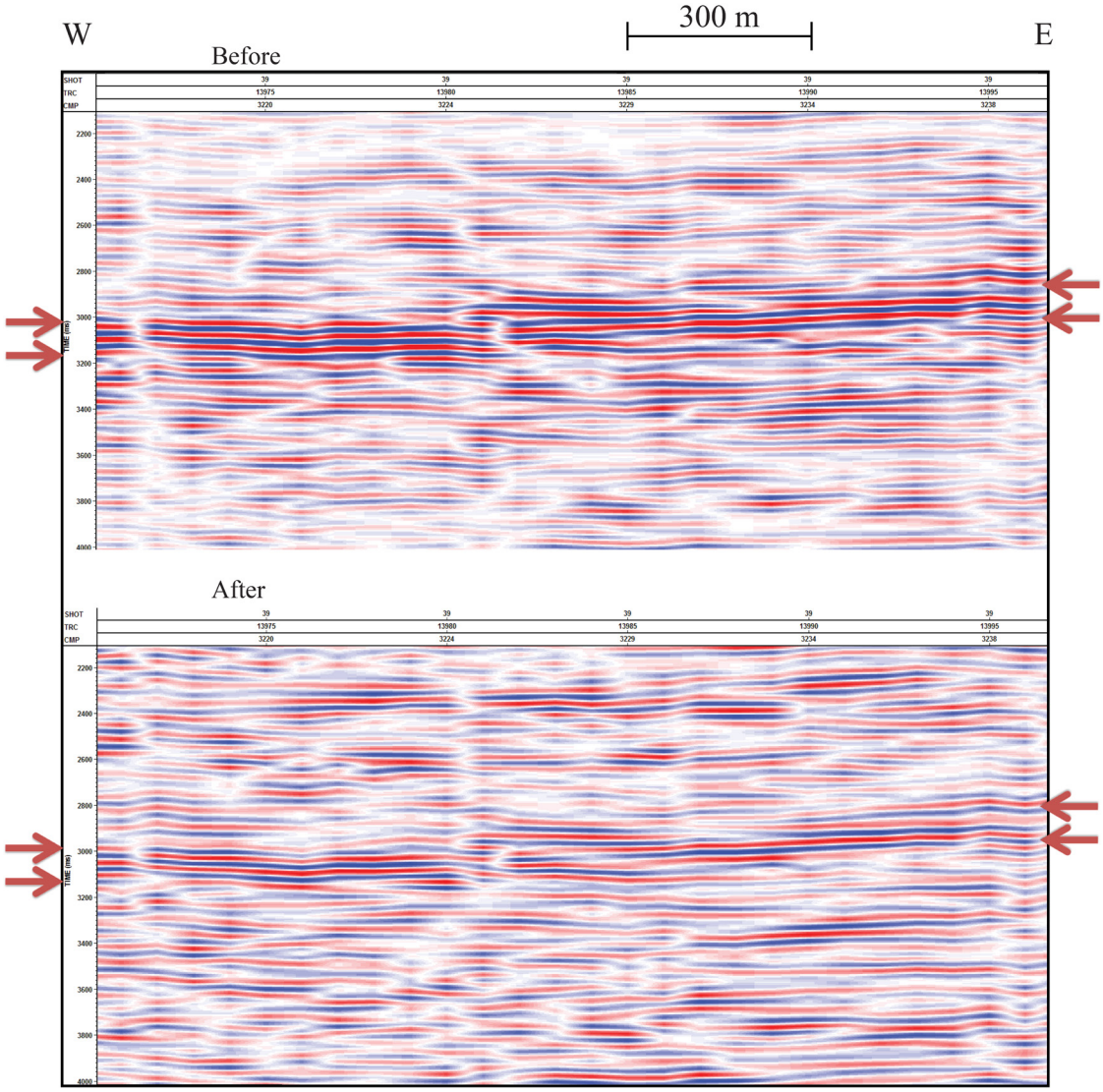

Figure 16. Data without deconvolution (top) and with spiking deconvolution applied (bottom). Wavelets are compressed and ringing is reduced.

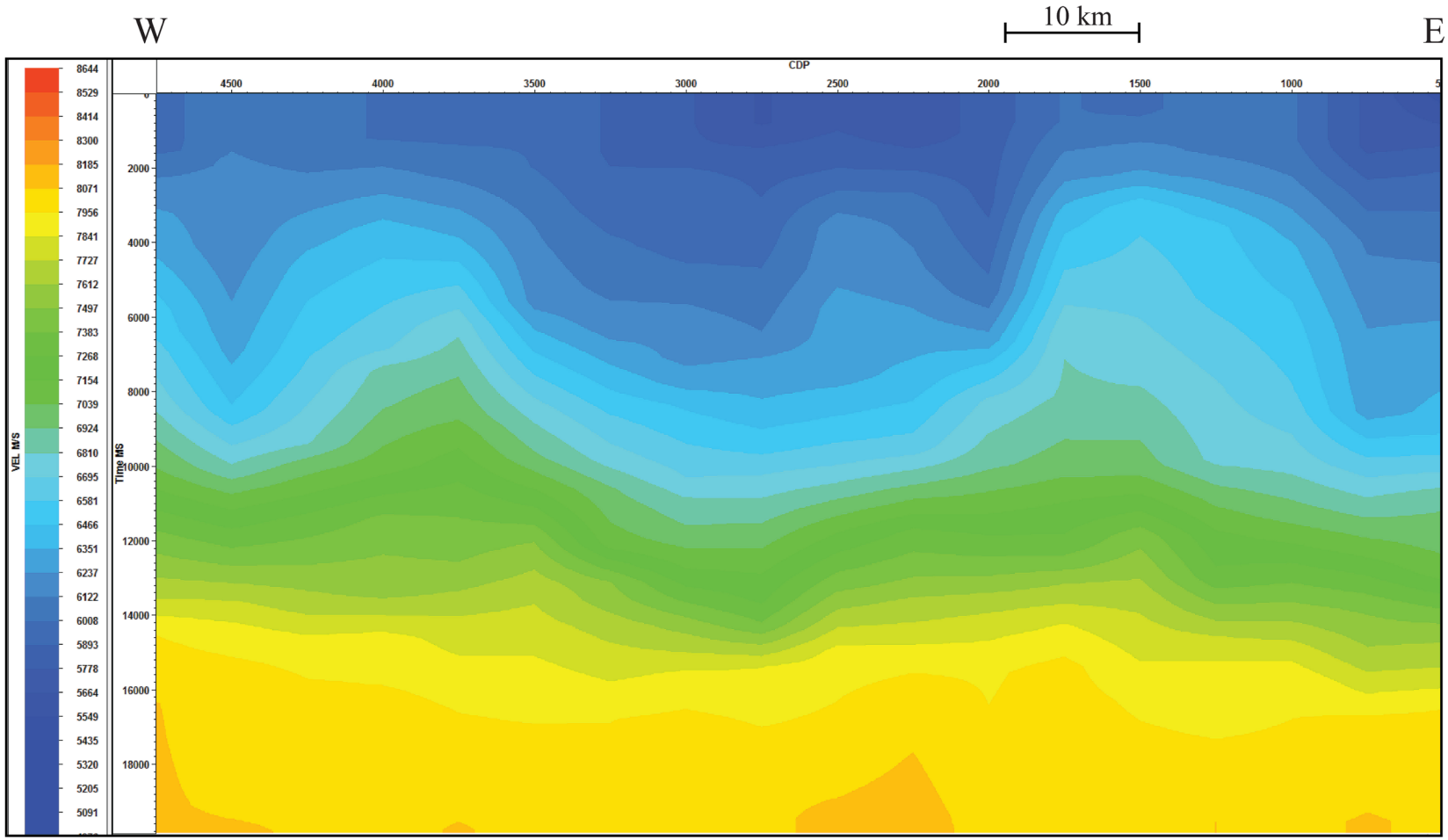

Figure 17. Velocity function generated during interactive velocity analysis.

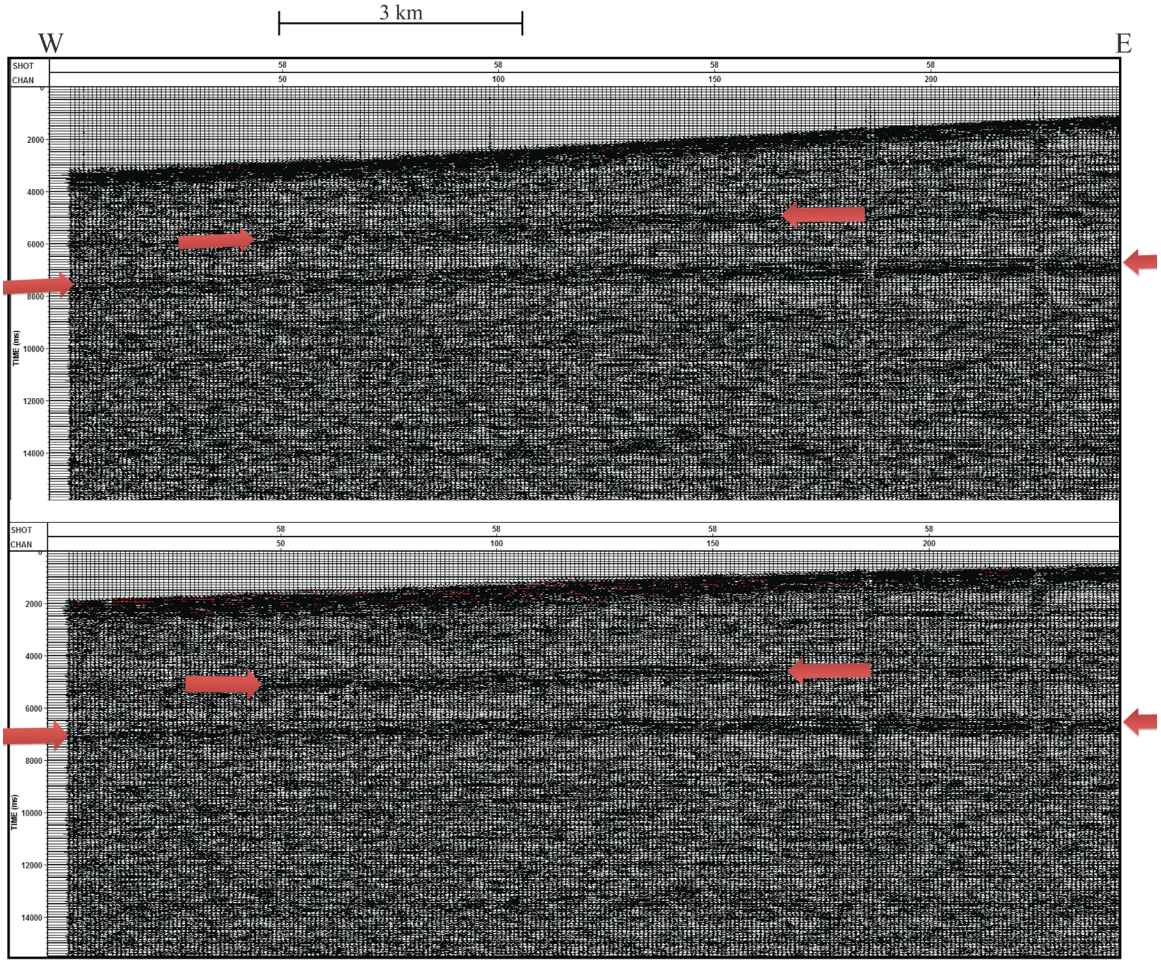

Figure 18. A comparison of data with and without normal move-out corrections applied. Uncorrected: top; NMO corrected: bottom

Migration

Migration is used to collapse diffractions and move dipping interfaces from their apparent location to their true subsurface location (Yilmaz, 2001). Since migration of wavelet data was ineffective, an approach using manual migration of deep reflectors was used. Endpoints of deep reflections were identified by visual inspection, recorded, and graphed (Figure 19). These reflection segments were plotted on a single graph (Figure 20) and migrated using the equation from Yilmaz 2001.

$$T = T_0 \times \sqrt[2]{1 - \frac{V^2 \times P_0^2}{4}} \quad (1)$$

T = migrated TWT

T_0 = original TWT

V = velocity

P_0 = dip constant

Ray Trace Modeling

Mac 2D Raytracer (MacRay) was used to verify the ray path of reflection data imaging the Moho boundary beneath the fold and thrust belt (Figure 21). A velocity net was created based on the southern Ural crustal velocities (Carbonell et al., 2000). The location of seismic charge shot points were plotted along the ~100 km transect. Pre-critical rays for all 68 shots were modeled in the receiver offset direction to ensure all possible reflections were identified.

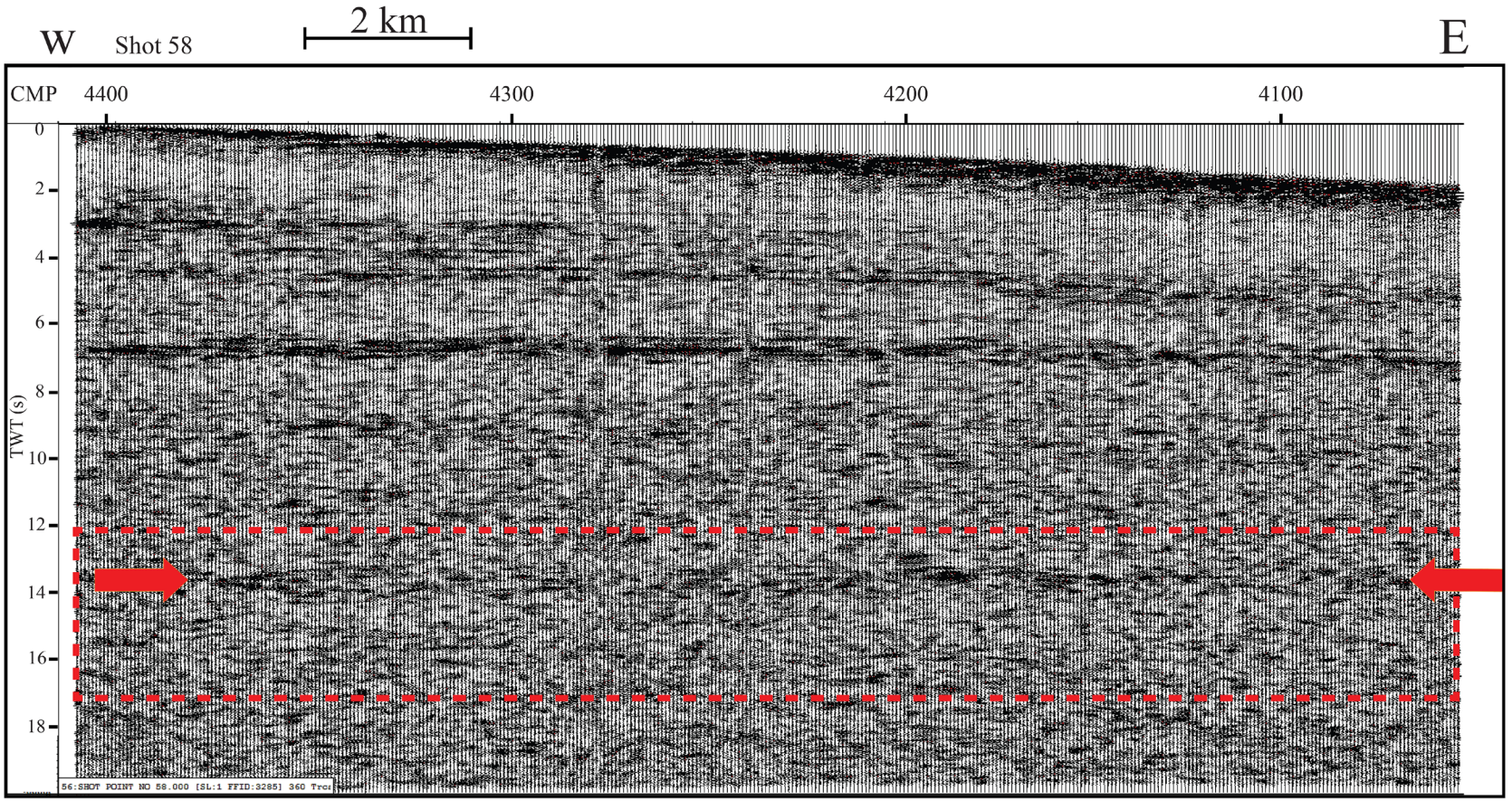

Figure 19. An example of the visual method used to select deep reflection endpoints for manual migration. The dashed red box represents the region where Moho reflections may occur. The red arrows show the endpoints of the selected reflector.

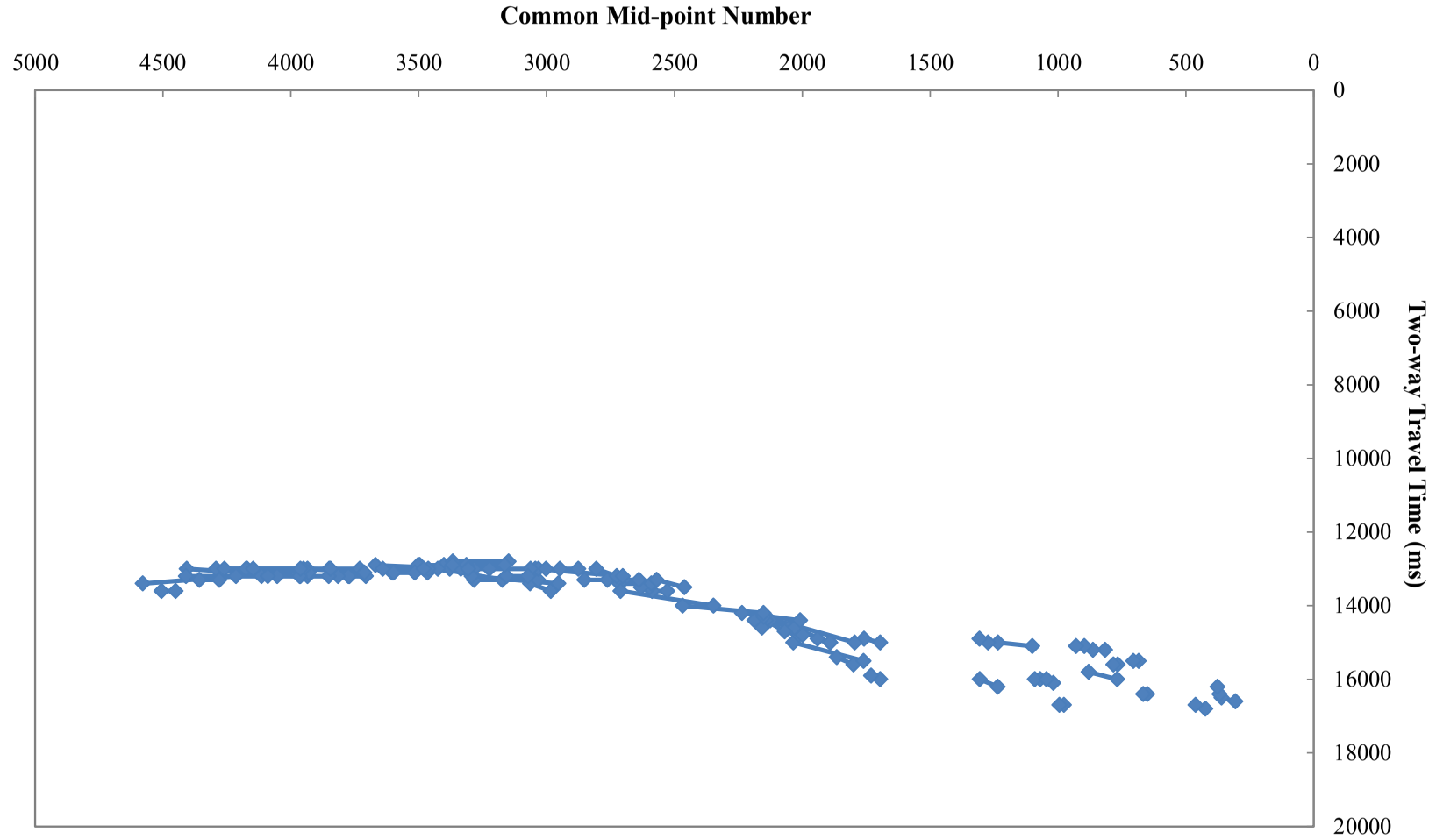

Figure 20. Plot of the deep reflection endpoints from the visual individual shot inspections.

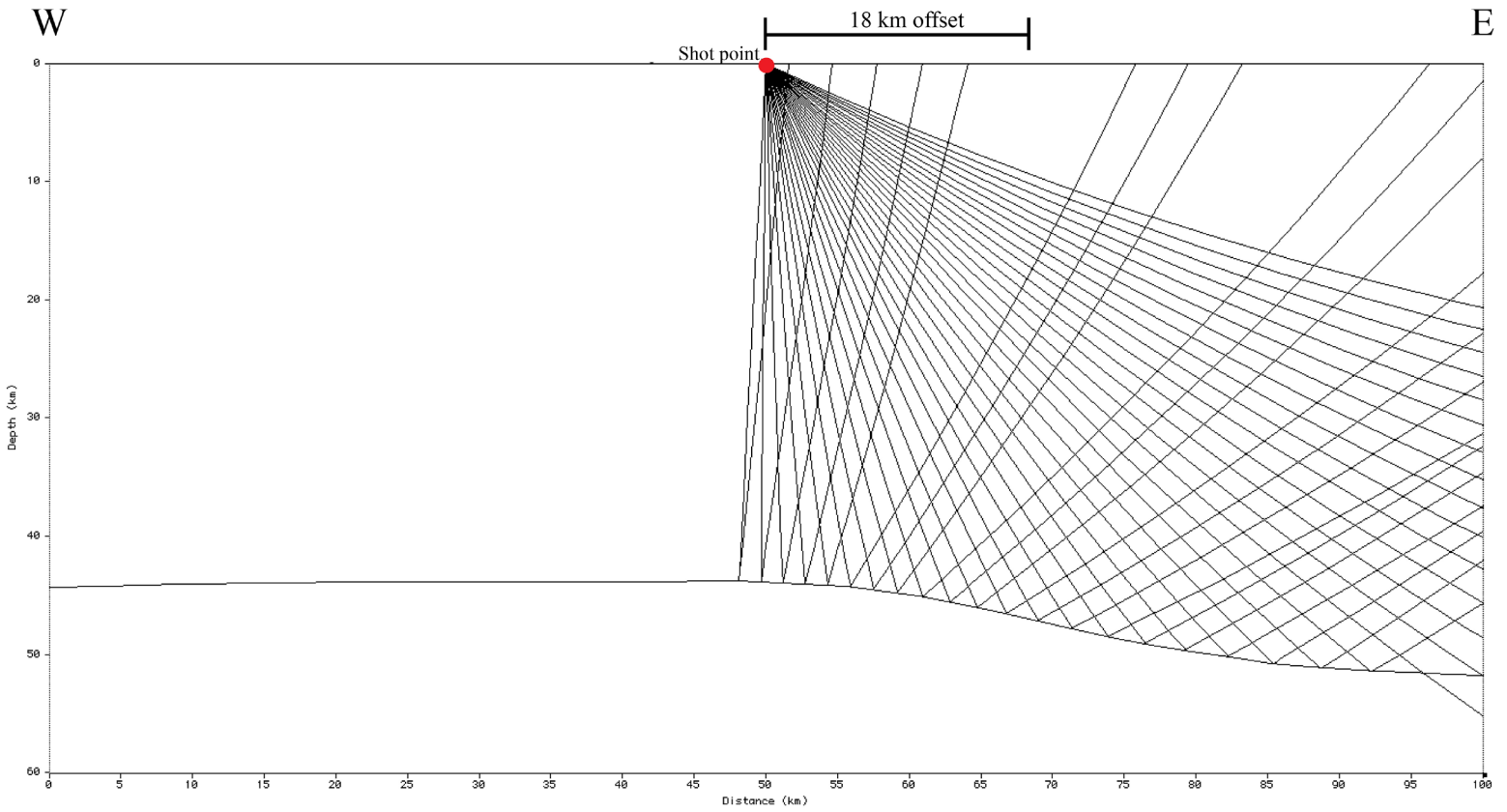

Figure 21. An example of reflection ray paths modeled in MacRay. Shot 24 is shown.

CHAPTER III

RESULTS

Seismic Reflection Processing

Overall, images of re-processed URSEIS explosion data are consistent with previous reports (Steer et al., 1998). In that study, Steer et al. (1998) noted several distinct reflectors of varying depth, thickness, and orientation. The upper and middle crust were said to contain several east dipping reflections which overlie a much deeper 3-9 km thick band of reflections (Steer at al., 1998). For this study, the stacked section was split into three separate panels which are further subdivided and described (Figure 22). Additionally, the location, start/end times, TWT, and dip for reflections picked in the stacked section are summarized in tabular form (Table 2).

Western Portion of the Fold and Thrust Belt

Panel 1 consists of the western most third of the stacked section for the fold and thrust belt (Figure 22, Panel 1). Several horizontal and subhorizontal reflectors can be identified between ~2-8 s TWT and a thick band of reflections is present at approximately 14 s TWT (Figure 22, Panel 1 and Figure 23).

Several reflectors imaged above 8 s TWT can be identified in this shallow, western portion of the fold and thrust belt (Figure 24). Horizontal reflections are observed from CMP 4420 to 4350 at approximately 2.2 s TWT (Figure 24, reflector 1). These reflections are moderate amplitude and discontinuous. Just beneath reflector 1, subhorizontal

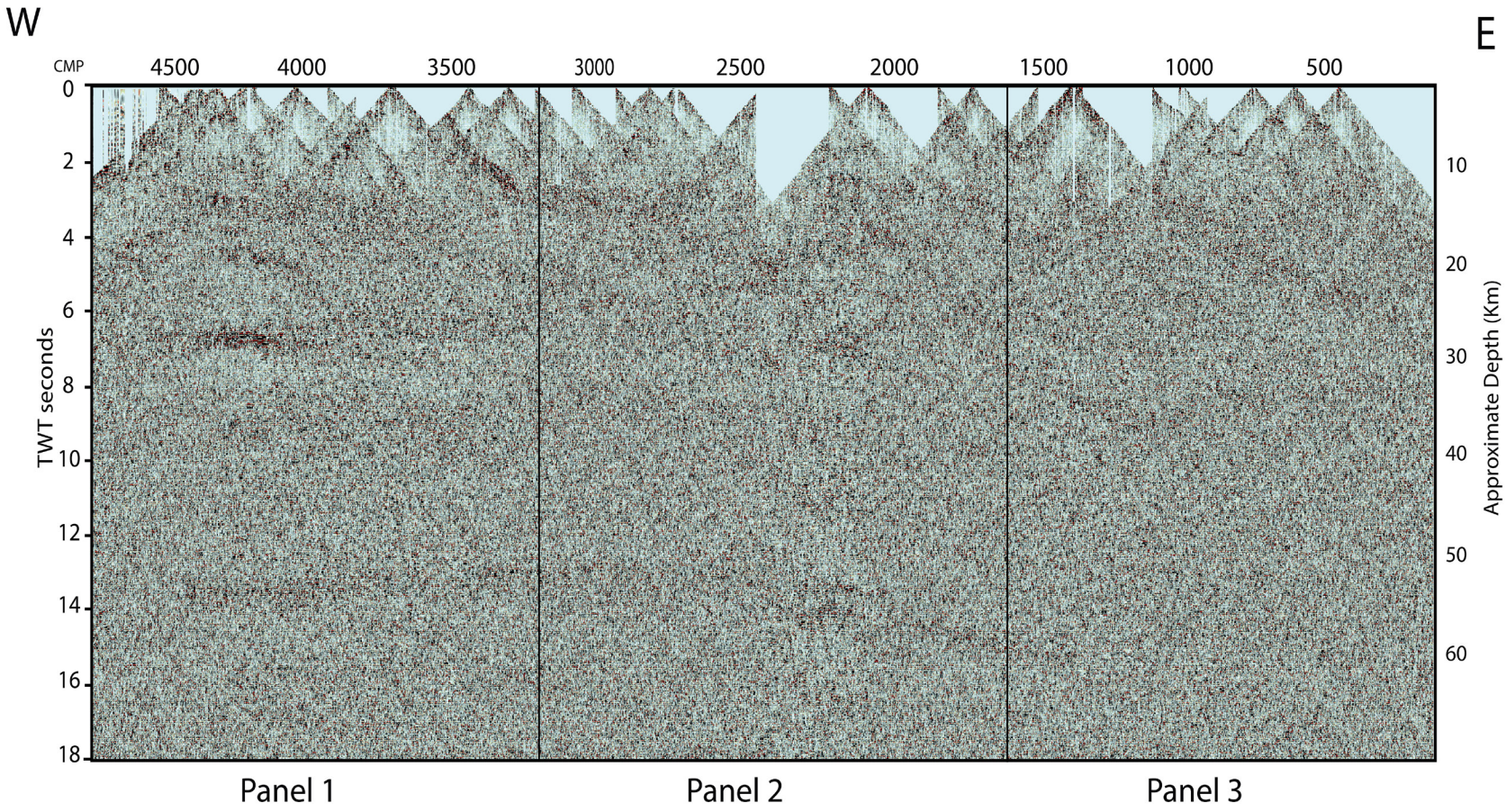

Figure 22. Processed and stacked section with three panels shown. Note the reflective upper crust and large deep reflector between approximately 14 and 16 seconds.

Table 2. A summary of reflectors observed in the processed and stacked data.

Panel	Box	Reflector	Start TWT (s)	End TWT (s)	Start CMP	End CMP	Apparent Dip (Degrees)	Dip Direction
Panel 1								
	Box 1	1	2	2	4420	4350	0	
		2	3	3.2	4400	4300	3	East
		3	3.8	4	4400	4300	2	East
		4	4.5	5	4360	4150	6	East
		5	3.5	3.3	4200	3960	3	West
		6	7	7	4200	3960	0	
	Box 2	1	3.5	3.5	3960	3800	0	
		2	2	3	3850	3750	6	
		3	1	2.5	3680	3450	20, 15	East
		4	4	4	3600	3400	3	East
		5	6	6	3960	3400	0	
	Box 3	1	14	13.5	4490	3950	2	West
	Box 4	1	13.5	13.3	3900	3400	2	West
Panel 2								
	Box 1	1	2	2.5	3300	3240	12	East
		2	3	3.4	3350	3200	10	East
		3	6	6	3390	2980	0	
	Box 2	1	5	5	2880	2750	0	
		2	4.5	4.5	2700	2600	0	
	Box 3	1	2.5	2.5	2450	2300	5	East
		2	4	4.2	2350	2200	5	East
		3	4	4	2500	2350	0	
		4	6.5	7	2500	2300	5	East
	Box 4	1	14	14	3350	2750	0	
	Box 5	1	14	15	2690	1950	6	East
Panel 3								
	Box 1	1	0.5	5	1400	600	15-20	East
	Box 2	1	15	15.3	1990	1710	5	East

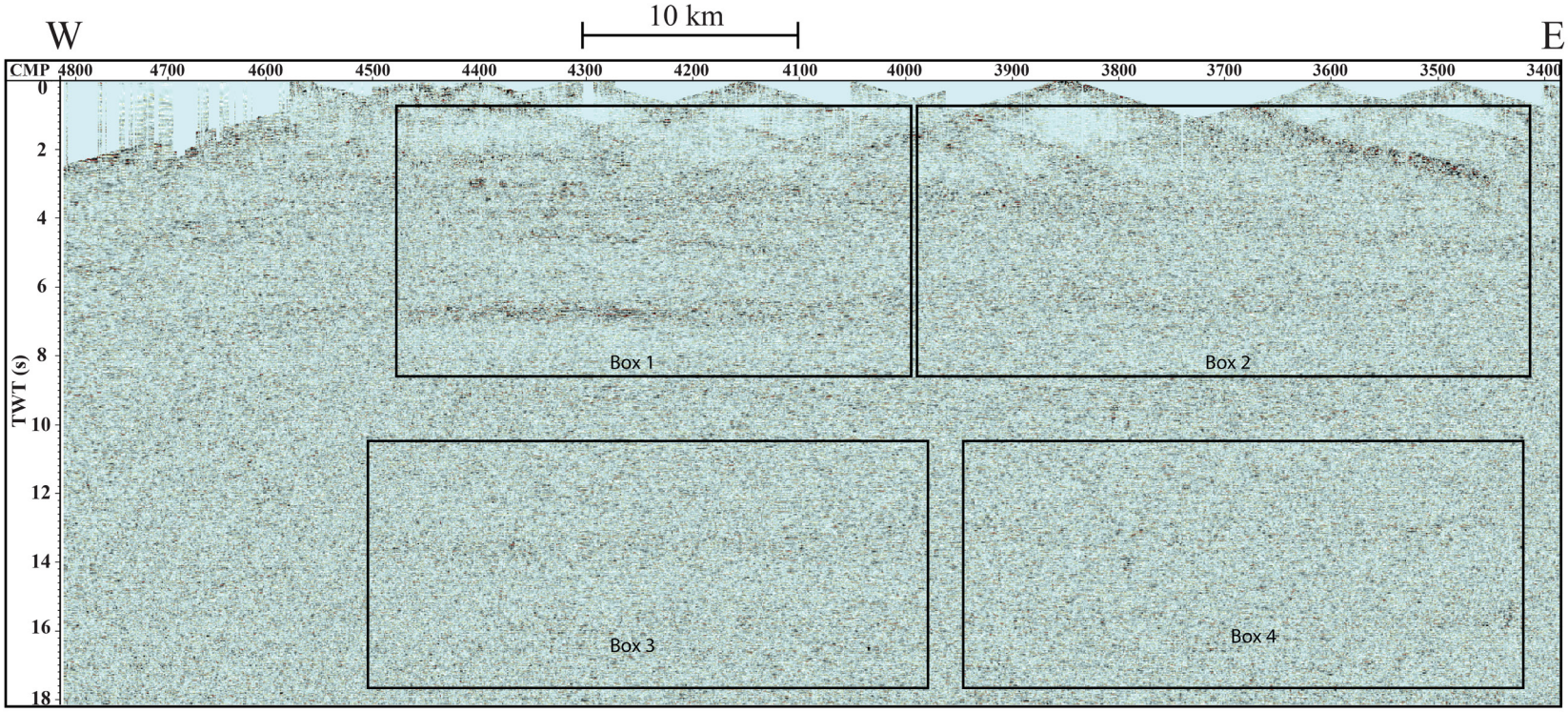

Figure 23. Zoomed image of Panel 1 from the stacked section showing the western portion of the fold and thrust belt. Four boxes are shown that will be discussed in further detail. Stretched horizontally 6:1.

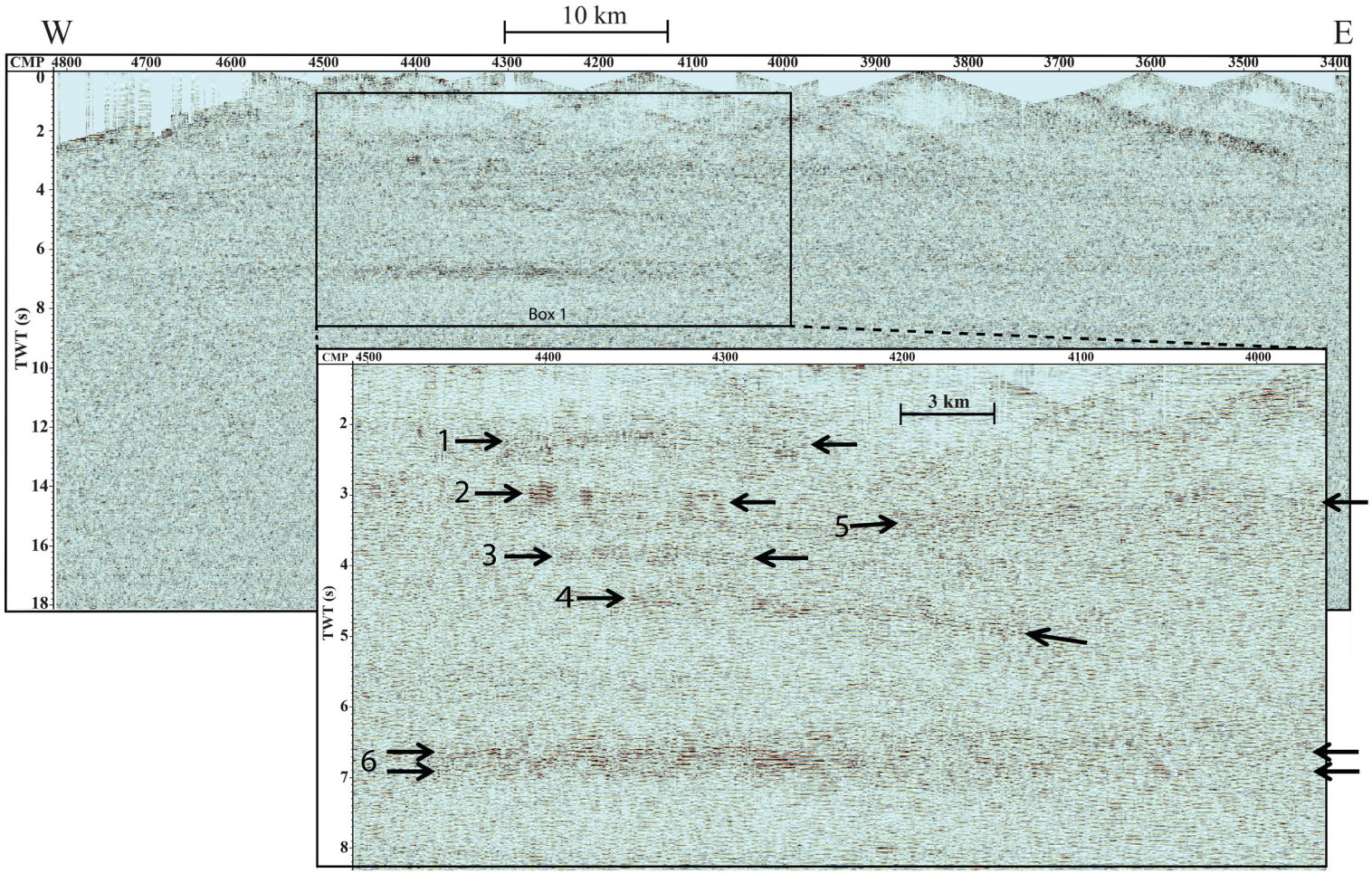

Figure 24. Zoomed image of Box 1 located within Panel 1 showing the shallow, western portion of the fold and thrust belt. Six reflectors are observed in this region. Stretched horizontally 6:1

reflections are observed from CMP 4400 to 4300 at 3 s TWT (Figure 24, reflector 2). These reflections are high amplitude, discontinuous, and dip 3 degrees eastward. Beneath reflector 2, more subhorizontal reflections are imaged from CMP 4400 to 4300 at less than 4 s TWT (Figure 24, reflector 3). These reflections are discontinuous, moderate amplitude, and dip approximately two degrees eastward. Additional subhorizontal reflections are observed between CMP 4360 and 4150 at approximately 4.5 s TWT (Figure 24, reflector 4). West dipping, subhorizontal reflections are observed between CMP 4200 and 3960 at approximately 3.5 s TWT (Figure 24, reflector 5). These reflections are moderate amplitude, discontinuous, and dip west at approximately 3 degrees. The deepest reflections are observed across the entire section at approximately 7 s TWT (Figure 24, reflector 6). These reflections are high amplitude in the west and have diminishing amplitude farther to the east. Reflector 6 is mostly discontinuous with an exception of reflections between approximately CMP 4300 and 4350.

Several additional reflectors can identified in this shallow, western portion of the fold and thrust belt at less than 8 s TWT (Figure 25). Horizontal reflections are identified from CMP 3960 to 3800 at approximately 3.5 s TWT (Figure 25, reflector 1). These reflections are discontinuous and low to moderate amplitude. Subhorizontal reflections are observed from CMP 3850 to 3750 at approximately 2 s TWT (Figure 25, reflector 2). These reflections are moderate amplitude, discontinuous, and dip eastward at approximately 6 degrees. Strong subhorizontal reflections are observed from CMP 3680 to 3450 at approximately 1 to 2.5 s TWT (Figure 25, reflector 3). These reflections are moderate to high amplitude and become more continuous to the east. Reflector 3 dips approximately 20 to 15 degrees to the east. Additional subhorizontal reflections are observed from CMP 3600 to 3400 at 4 s TWT (Figure 25, reflector 4). These reflections are moderate to low amplitude, discontinuous, and dip east at approximately 3 degrees. The deepest

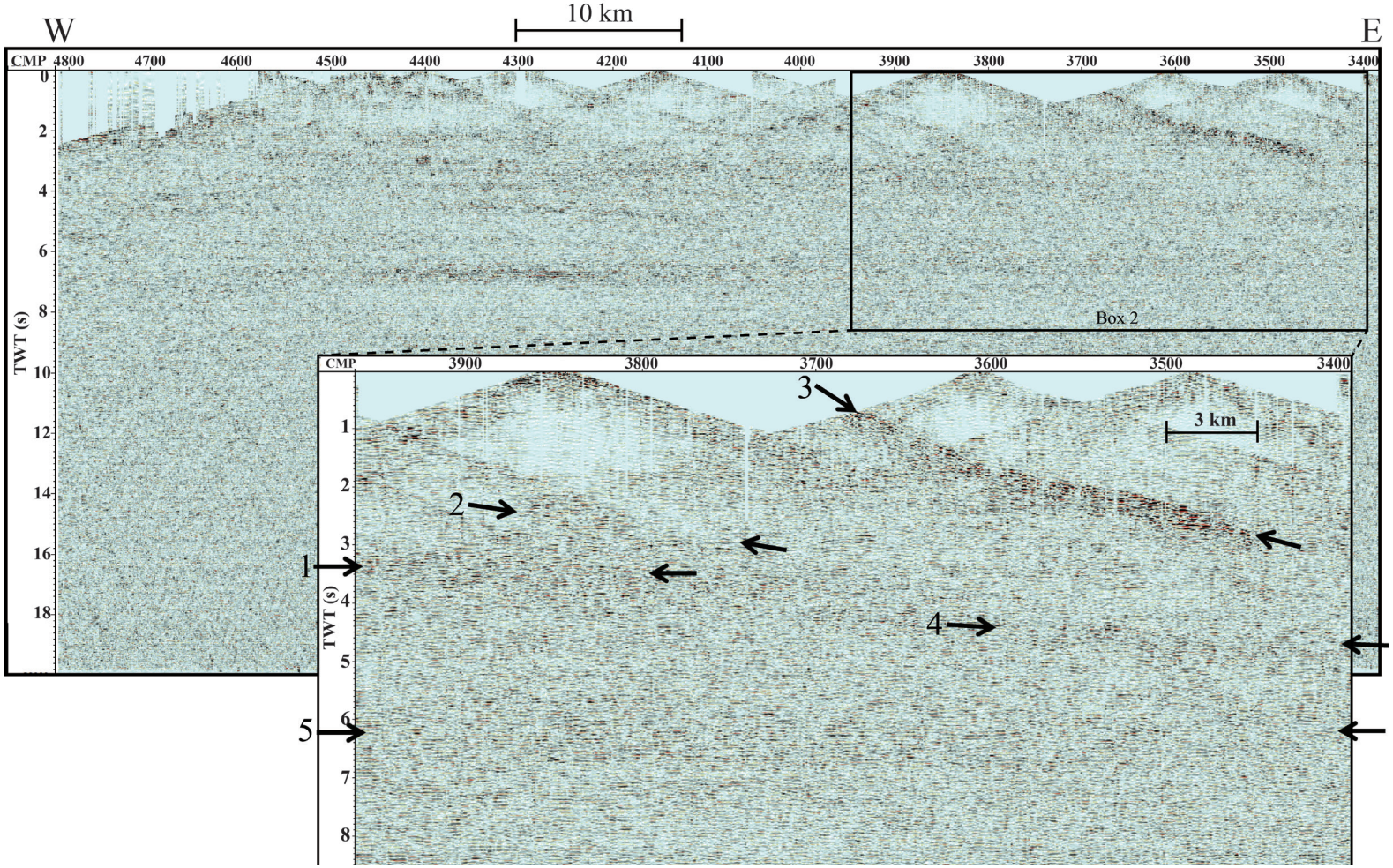

Figure 25. Zoomed image of box 2 from Panel 1 showing more of the shallow, western portion of the fold and thrust belt. Five reflectors are observed in this region. Stretched horizontally 6:1.

reflections are observed across the entire section at approximately 6 s TWT (Figure 25, reflector 5). These reflections are low to moderate amplitude and are discontinuous.

Deeper data contain a single reflection package that is identified in the western, deep portion of the fold and thrust belt (Figure 23; box 3 and Figure 26). The reflections are imaged at approximately 13.5 to 14 s TWT. These reflections are moderate amplitude, discontinuous across the entire section, and dip approximately 2 degrees westward.

Farther east a single reflection package is observed in the deep portion of the fold and thrust belt (Figure 27). The reflections are imaged at approximately 13.5 s TWT across the entire section. These reflections are moderate amplitude, discontinuous across the entire section, and dip westward by approximately 2 degrees.

Middle Portion of the Fold and Thrust Belt

Several horizontal and subhorizontal reflections occur at less than 8 s TWT and a deep reflection package is observed at 14 s (Figure 22, panel 2).

Three reflectors are identified in the shallow, west central portion of the fold and thrust belt (Figure 28; box 1 and Figure 29). Subhorizontal reflections are observed from CMP 3300 to 3240 at approximately 2 to 2.5 s TWT (Figure 29, reflector 1). These reflections are moderate amplitude, discontinuous, and dip 12 degrees to the east. Beneath reflector 1, more subhorizontal reflections are observed from CMP 3350 to 3200 at approximately 3 s TWT (Figure 29, reflector 2). These reflectors are moderate to high amplitude, discontinuous, and dip 10 degrees to the east. The deepest reflections are observed across entire section at less than 6 s TWT (Figure 29, reflector 3). These reflections are moderate to low amplitude and discontinuous across the entire section.

The central portion of this area (Figure 28; box 2) contains two reflections (Figure 30). Horizontal reflections are observed from CMP 2880 to 2750 at greater than 5 s TWT (Figure 30, reflector 1). These reflections are moderate to low amplitude and are

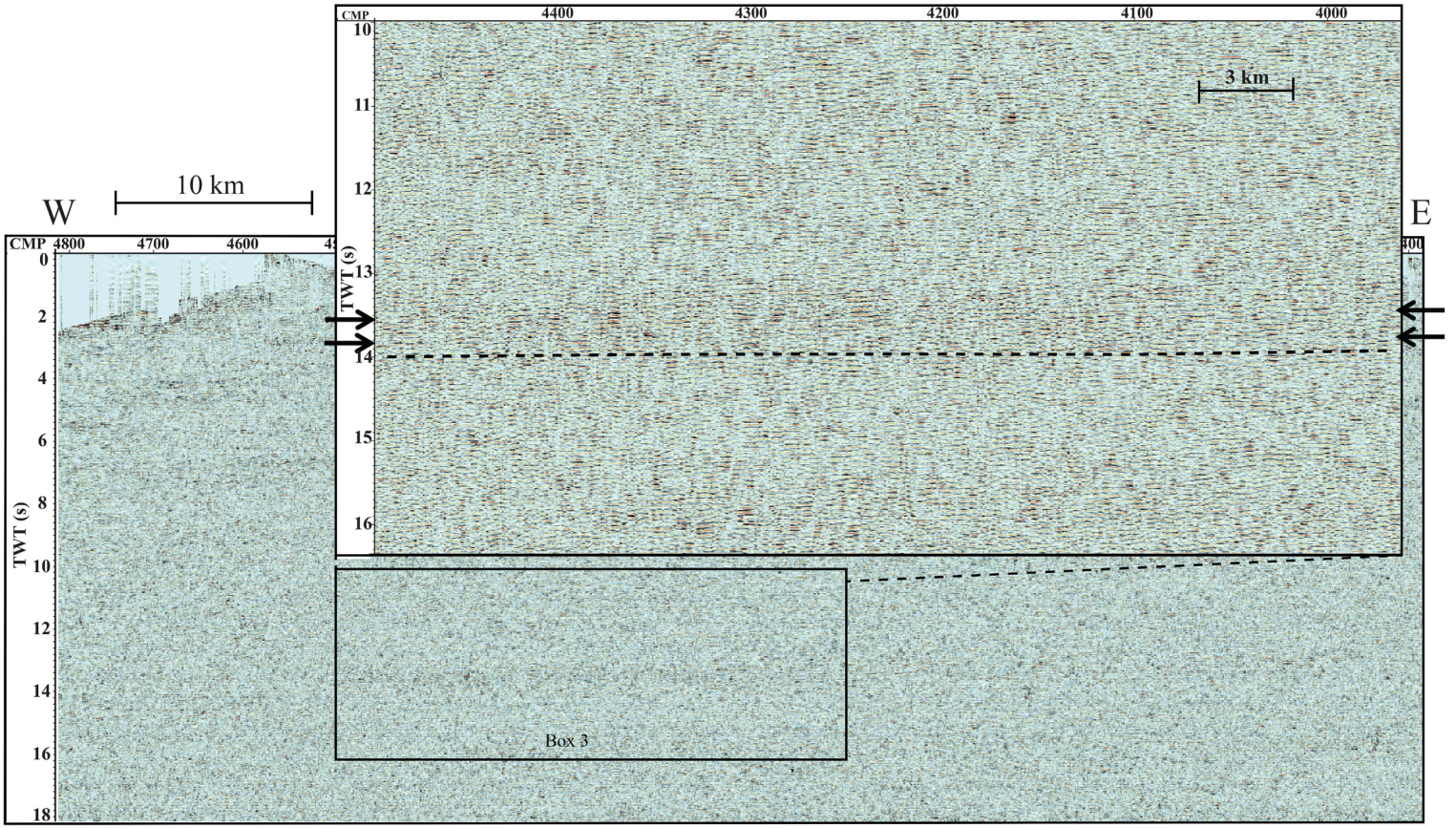

Figure 26. Zoomed image of box 3 from Panel 1 showing the deep, western portion of the fold and thrust belt. One large reflection package is observed in this region. Stretched horizontally 6:1

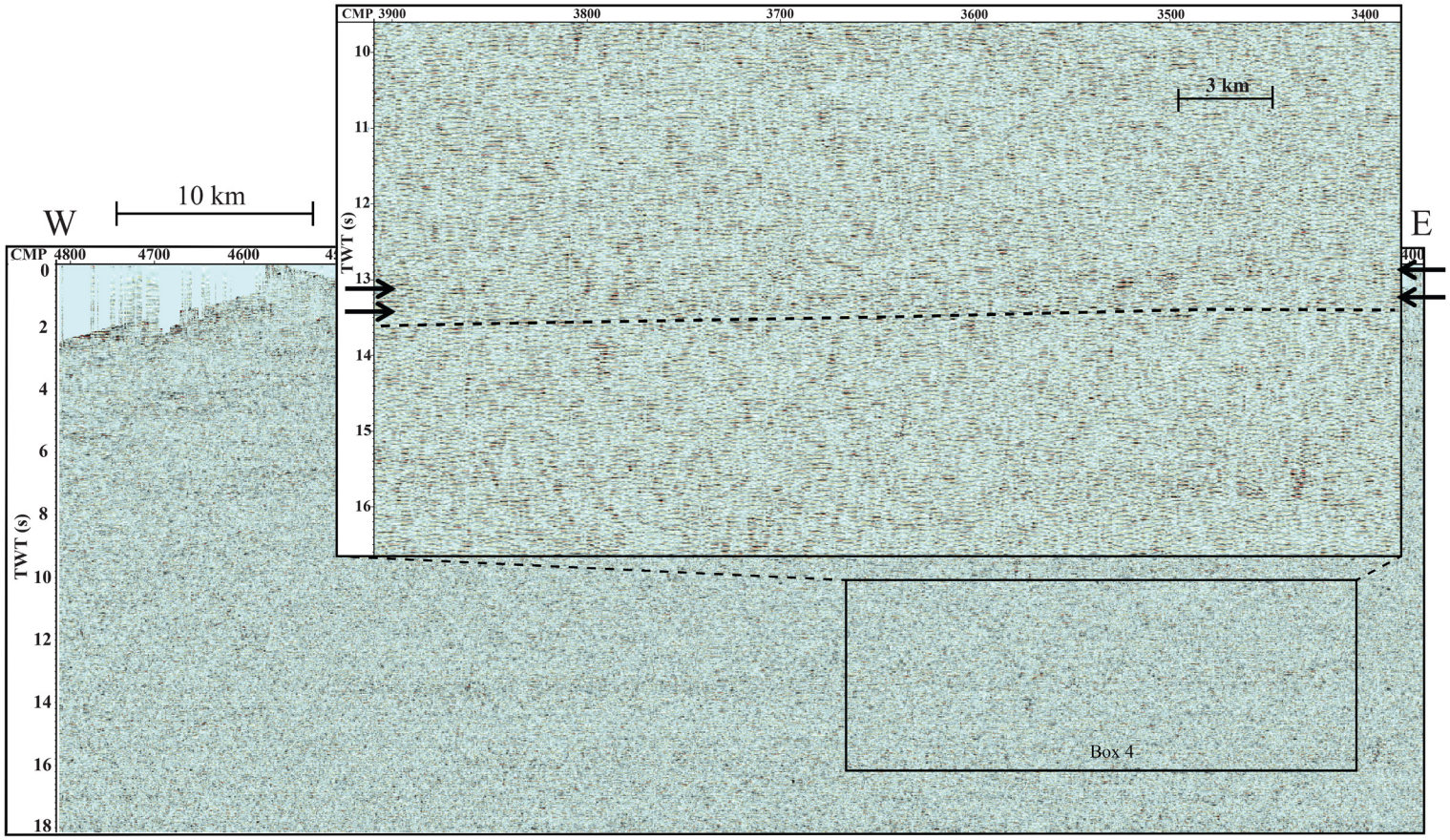

Figure 27. Zoomed image of box 4 from Panel 1 showing more of the deep, western portion of the fold and thrust belt. One reflection package is observed in this region. Stretched horizontally 6:1.

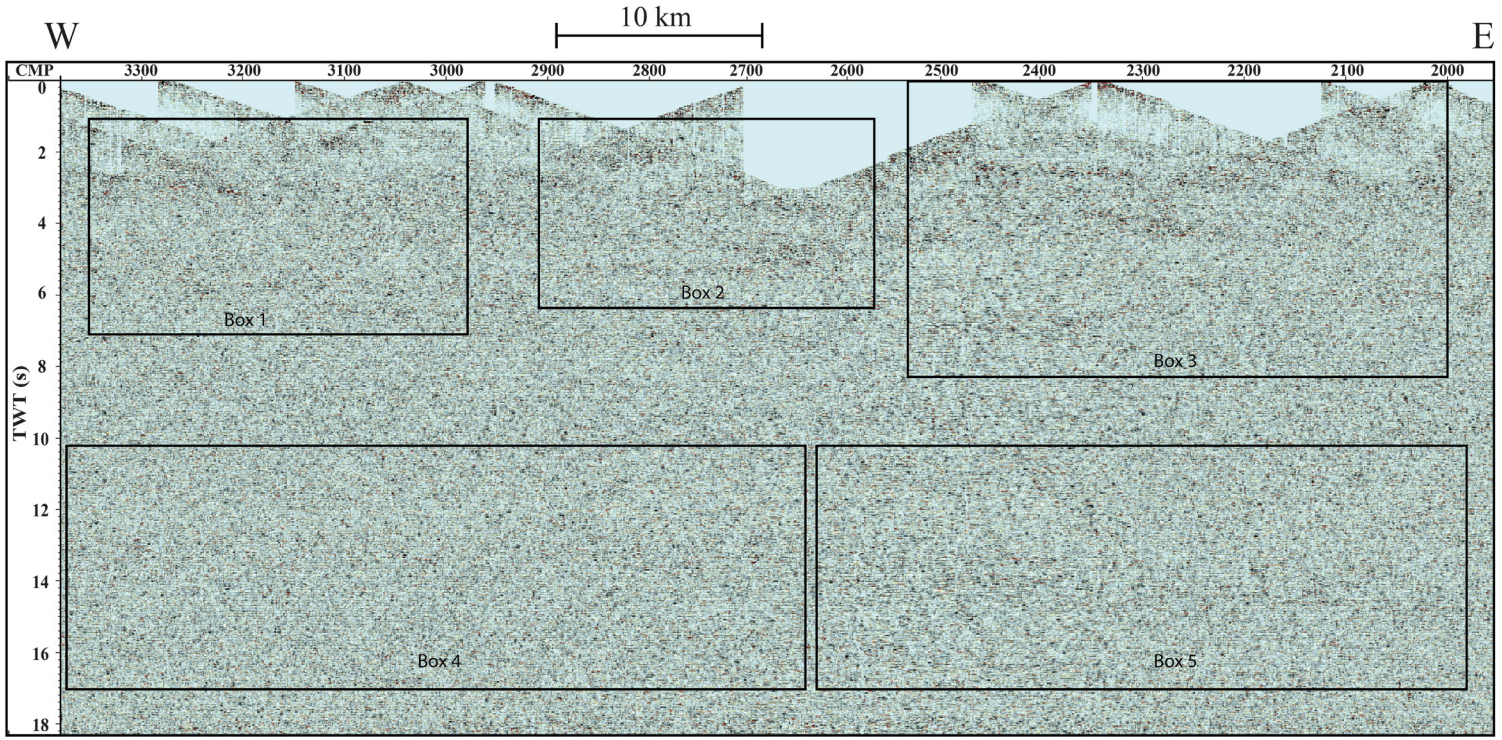

Figure 28. Zoomed image of Panel 2 from the stacked section showing the central portion of the fold and thrust belt. Five boxes are shown which will be discussed in further detail. Stretched horizontally 6:1.

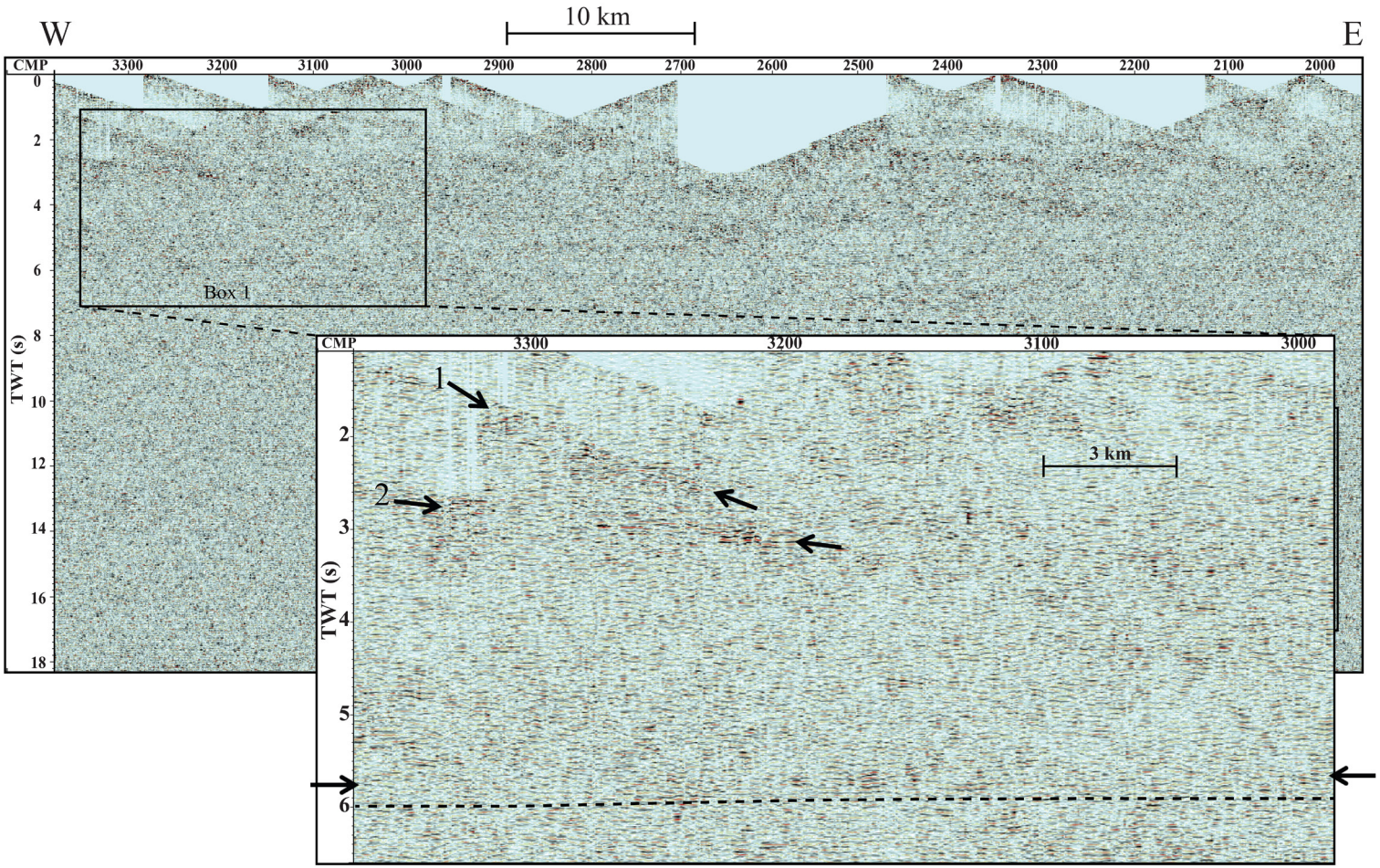

Figure 29. Zoomed image of box 1 from Panel 2 showing the shallow, west central portion of the fold and thrust belt. Three reflectors are observed in this box. Stretched horizontally 6:1.

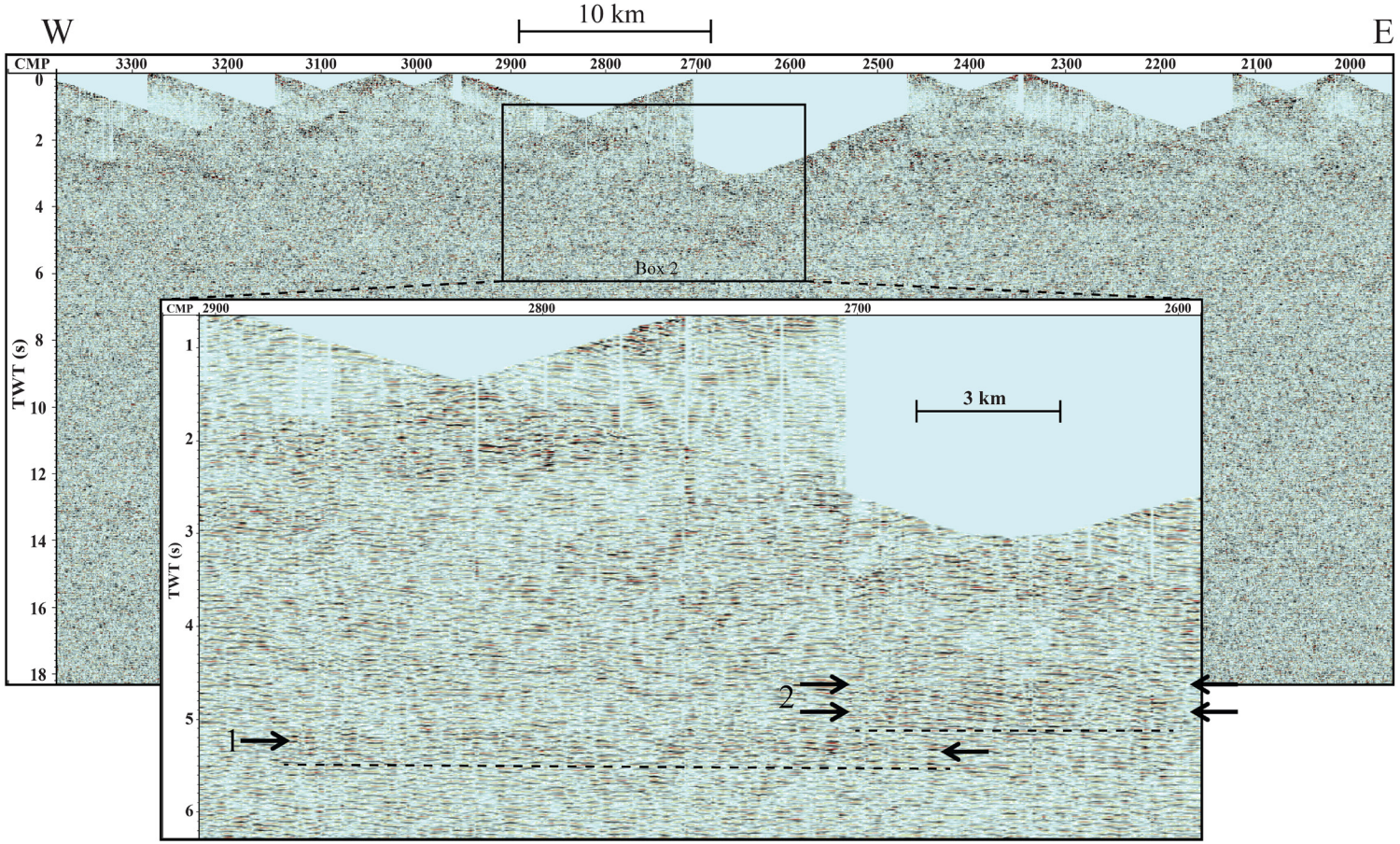

Figure 30. Zoomed image of box 2 from Panel 2 showing the shallow, central portion of the fold and thrust belt. Two reflectors are observed in this box. Stretched horizontally 6:1.

discontinuous. A thick band of horizontal reflections are observed from CMP 2700 to 2600 at approximately 4.5 s TWT (Figure 30, reflector 2). These reflections appear to be of moderate amplitude and are discontinuous.

Four major reflectors are imaged in the shallow, east central portion of the fold and thrust belt (Figure 28; box 3 and Figure 31). Subhorizontal reflections are observed from CMP 2450 to 2300 at approximately 2.5 s TWT (Figure 31, reflector 1). These reflections are moderate amplitude, discontinuous, and dip 5 degrees to the east. Additional subhorizontal reflections are observed from CMP 2350 to 2200 at approximately 4 s TWT (Figure 31, reflector 2). These reflections are moderate amplitude, discontinuous, and dip 5 degrees to the east. Horizontal reflections are observed from CMP 2500 to 2300 at greater than 4 s TWT (Figure 31, reflector 3). These reflections are moderate to low amplitude and are discontinuous. The deepest reflections are observed from CMP 2500 to 2300 at approximately 6.5 s TWT (Figure 31, reflector 4). These reflections are low to moderate amplitude and are discontinuous.

Deep reflections are identified across this region at travel times between 13-15 s (Figure 28; box 4-5). These reflections are moderate to low amplitude and discontinuous. To the east, reflections are noted at 13.5 s TWT (Figure 32). Farther east, the reflections begin to dip beneath CMP 2400 trending 15 degrees eastward (Figure 33).

East Portion of the Fold and Thrust Belt

Fewer crustal reflectors were observed to the east. A single reflector is observed in the shallow crust and another reflector is observed deeper at 15 s TWT (Figure 22; panel 3 and Figure 34). A dipping reflection package is observed in the shallow, east portion of the fold and thrust belt (Figure 35). Reflections are also observed from CMP 1500 to 500 between approximately 1 and 6 s TWT. These reflections are high to moderate amplitude and discontinuous. The reflector dips at approximately 15 to 20 degrees to the east.

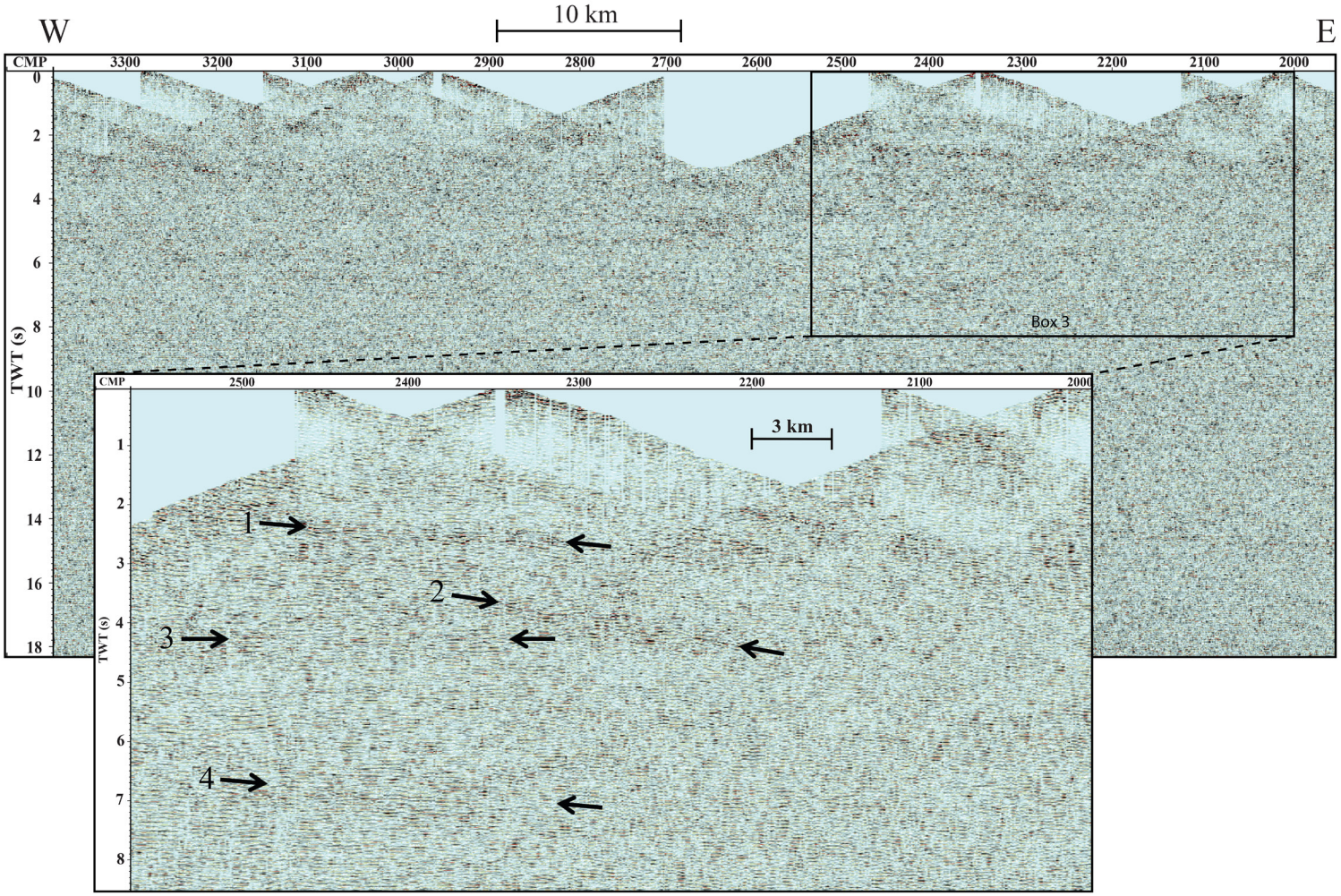

Figure 31. Zoomed image of box 3 from Panel 2 showing the shallow, east central portion of the fold and thrust belt. Four reflectors are observed in this box. Stretched horizontally 6:1.

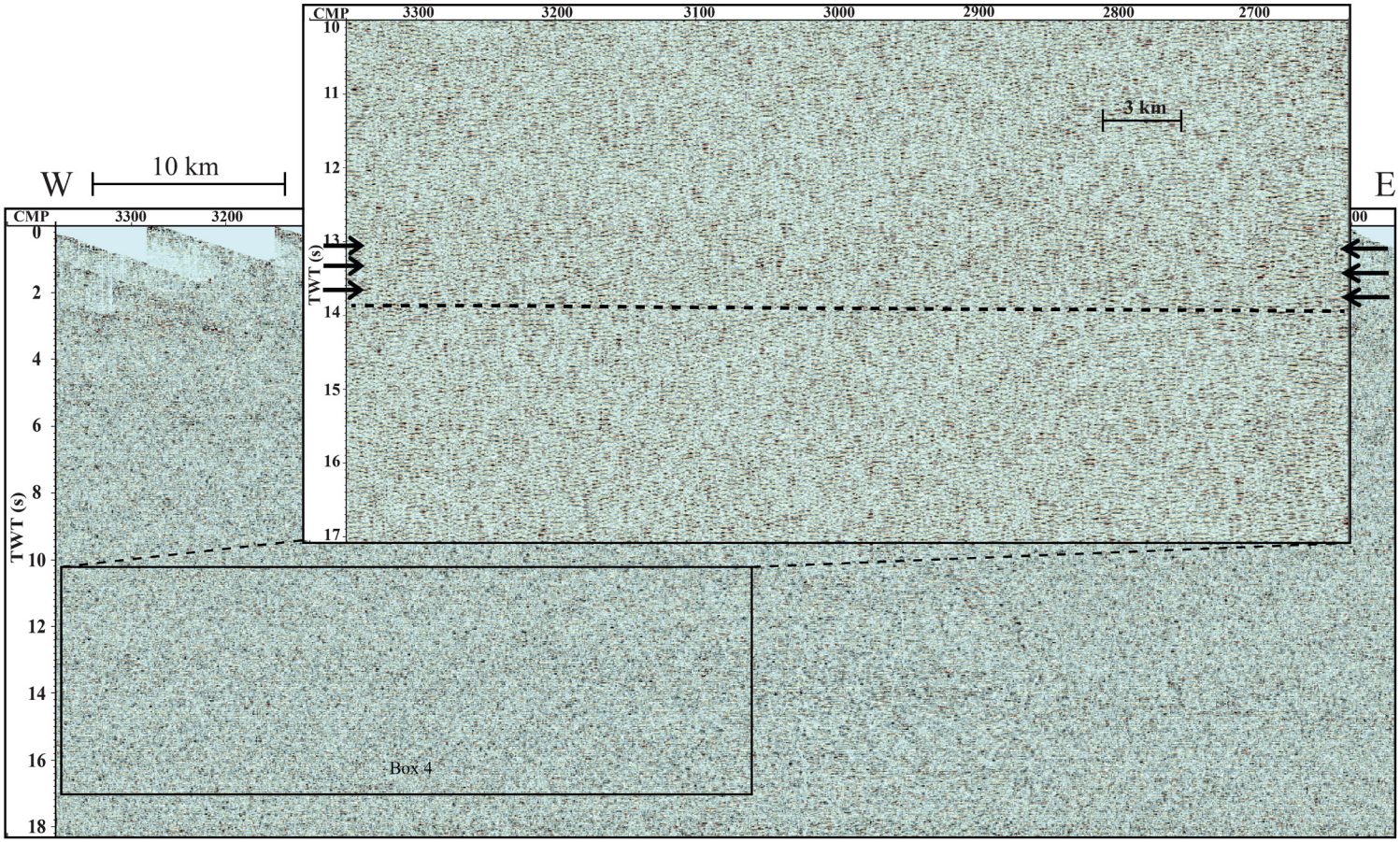

Figure 32. Zoomed image of box 4 from Panel 2 showing the deep, west central portion of the fold and thrust belt. A single reflection package is observed in this box. Stretched horizontally 6:1.

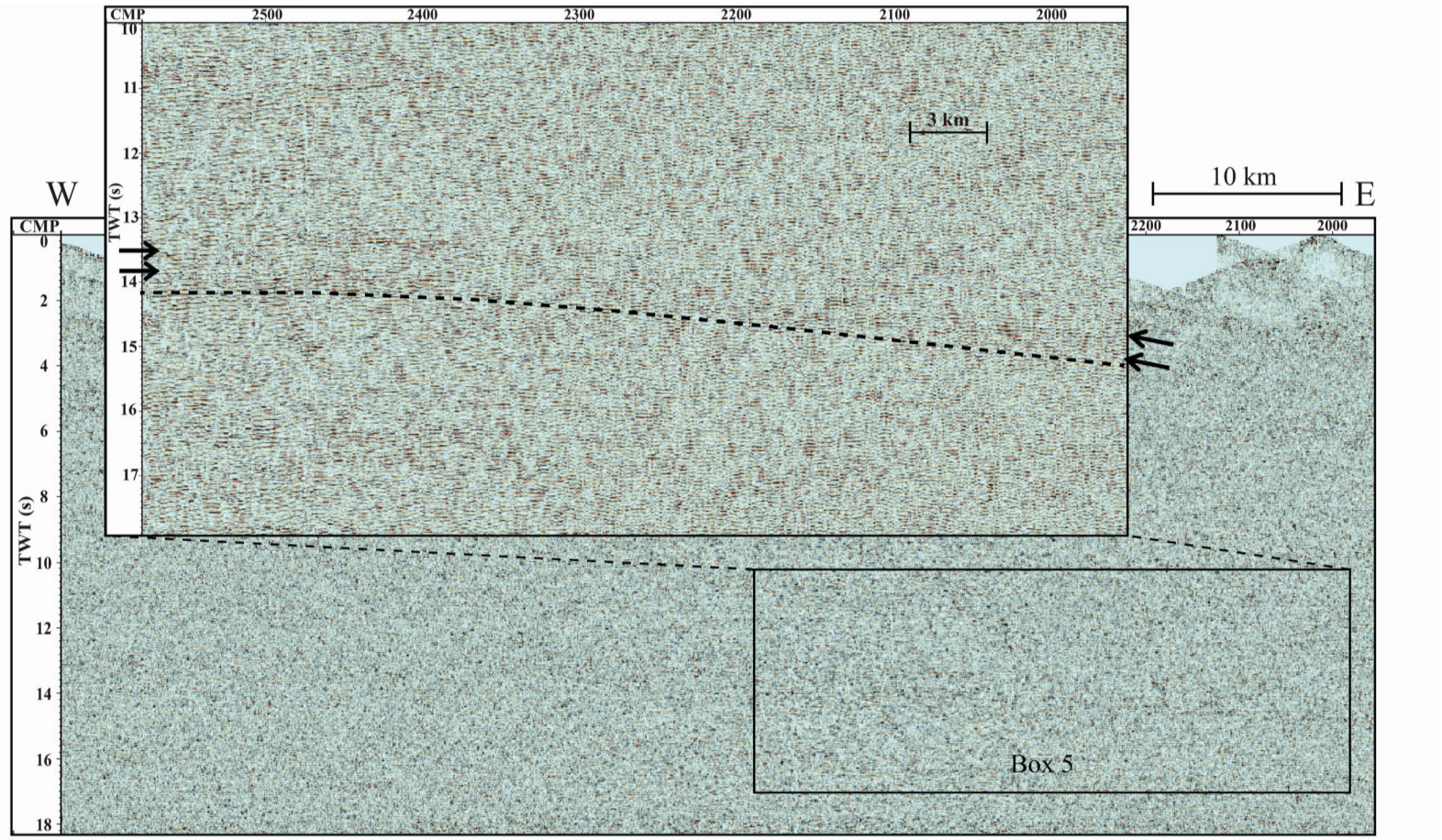

Figure 33. Zoomed image of box 5 from Panel 2 showing the deep, east central portion of the fold and thrust belt. One reflection package is observed in this box. Stretched horizontally 6:1.

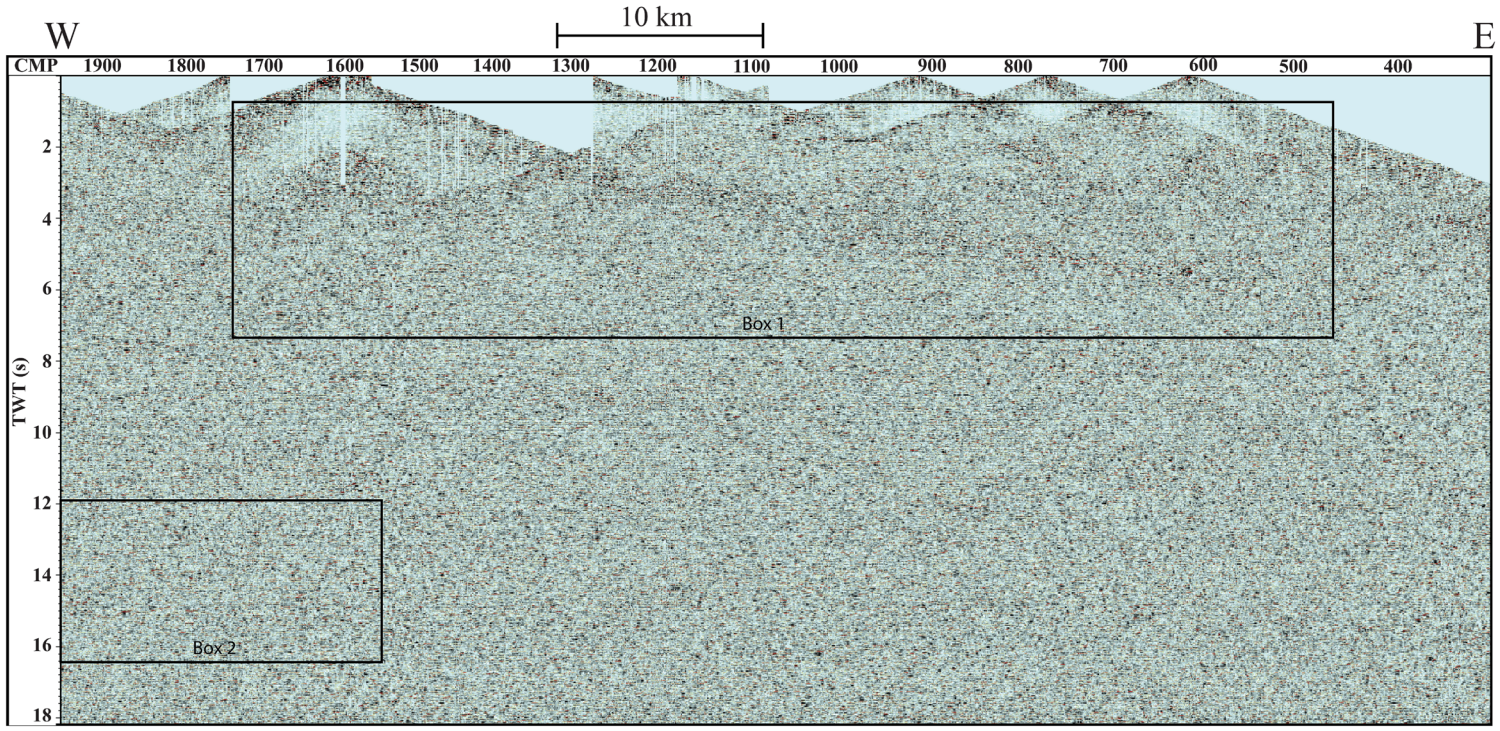

Figure 34. Zoomed image of Panel 3 from the stacked section showing the east portion of the fold and thrust belt. Two boxes are shown which will be discussed in further detail. Stretched horizontally 6:1

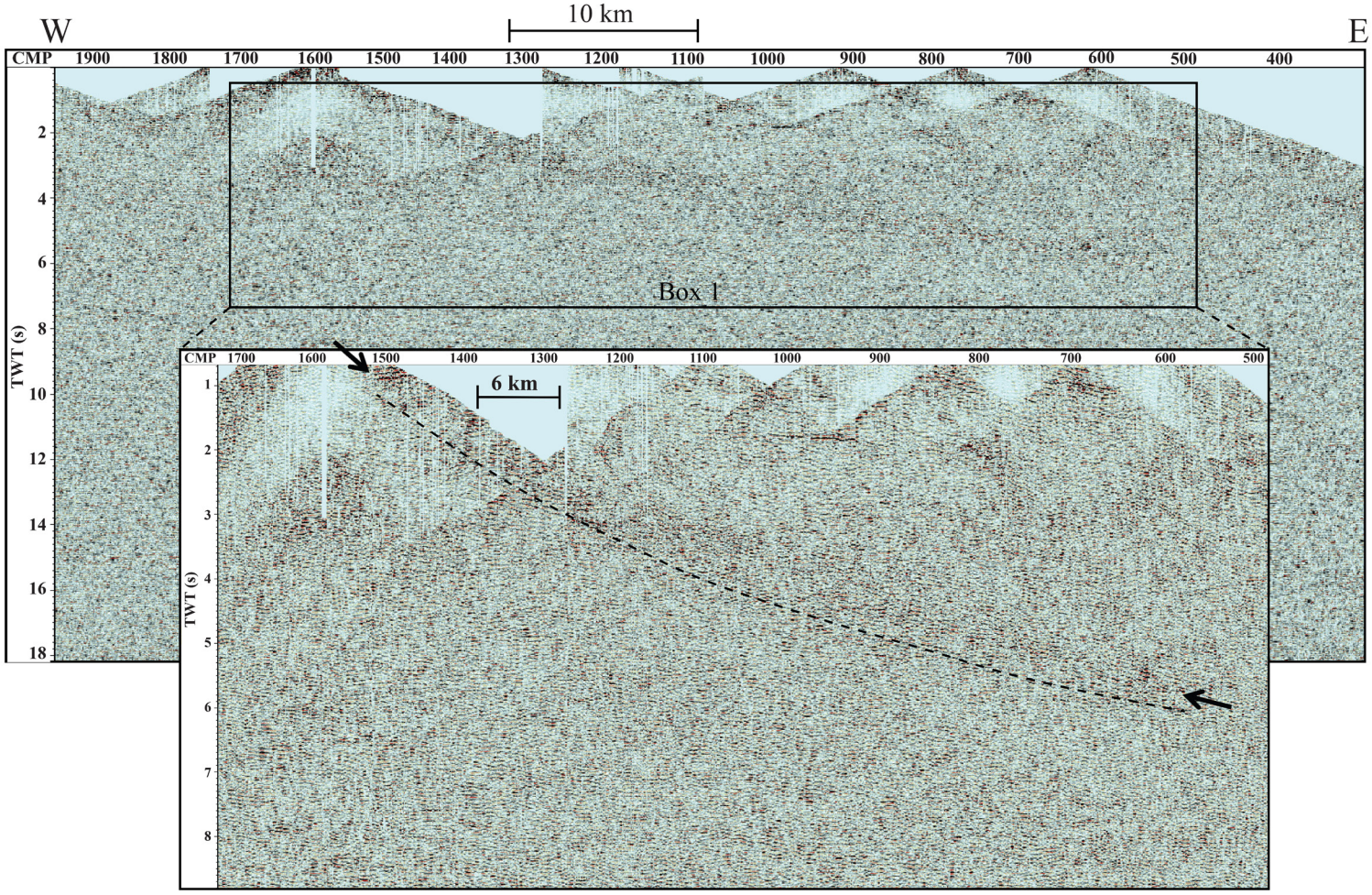

Figure 35. Zoomed image of box 1 from Panel 3 showing the shallow east portion of the fold and thrust belt. One large crustal reflector is observed in this box. Stretched horizontally 6:1.

Deeper in the section (Figure 36) a dipping reflection package is observed in the eastern portion of the fold and thrust. The reflections are observed across the entire portion of the profile at approximately 15 s TWT. These reflections are moderate to high amplitude, discontinuous, and dip approximately 5 degrees to the east.

Processing Corrections

Crooked line binning and static corrections improved the image of the re-processed data but did not appear to significantly affect the dip of the deep reflections. Crooked line binning accounted for offset (X, Y, Z) relationships between shots and receivers along the acquisition line. Applying crooked line binning eliminates incorrect vertical placement of reflectors (Gray et al., 1999; Nedimovi´and West, 2003). As a result, wavelets forming a reflection are moved to their correct horizontal position (Figure 37). Static corrections (refraction, receiver, and residual) adjust reflections by accounting for near surface topography and lithology that affect velocities and shot/ receiver placement (Cox, 1999). The effects of applying static shift corrections are observed in the processed, stacked data (Figure 38). Crooked line binning and static corrections did not flatten the dip of the deep reflections beneath the east portion of the fold and thrust belt.

Analysis of the Deep Reflections

Shot Inspection

Inspecting individual shots for deep reflections was an effective method for determining the geometry and dip of the deep reflections beneath the fold and thrust belt. The reflections observed in individual shots show a thick reflection package from CMP

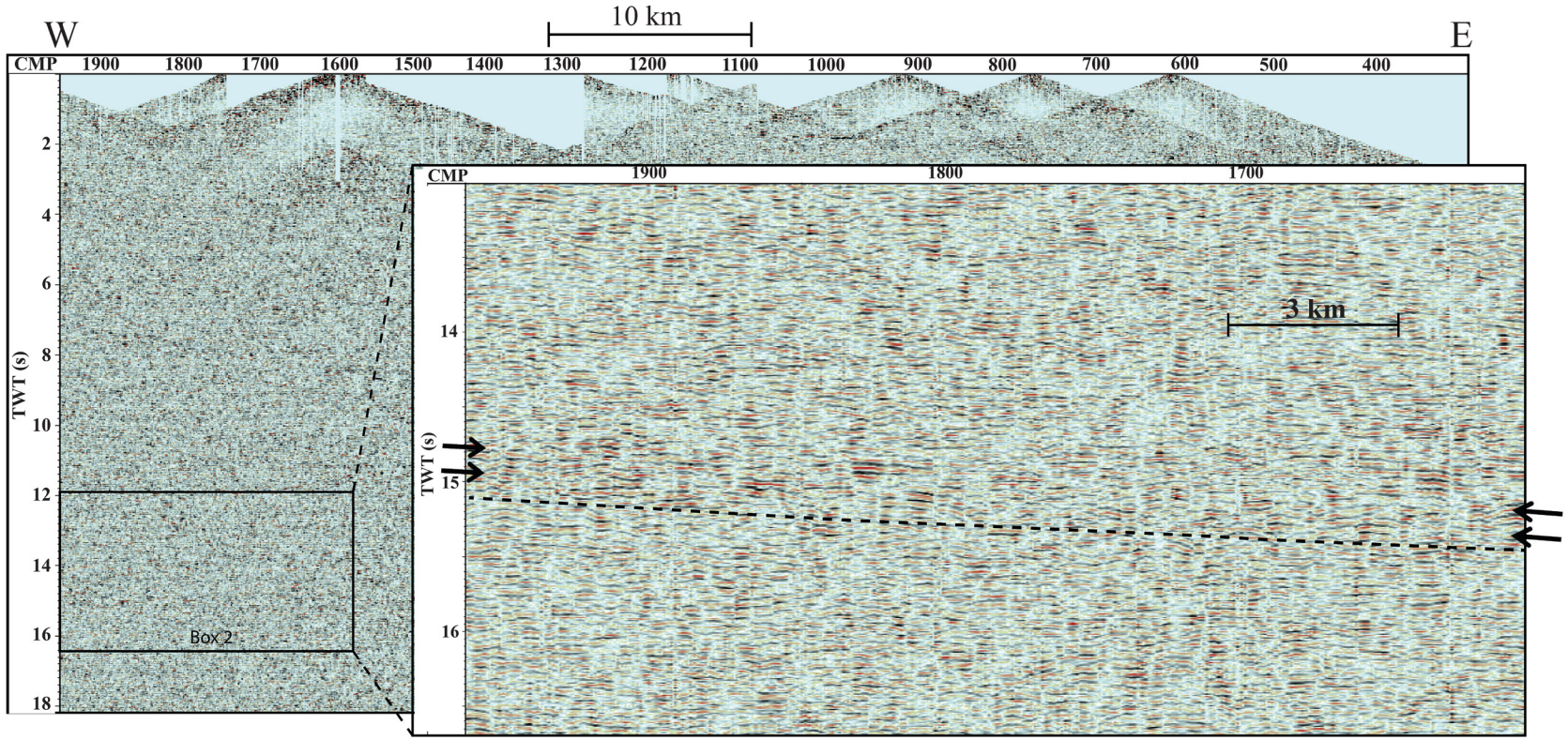

Figure 36. Zoomed image of box 2 from Panel 3 showing a deep section of the eastern fold and thrust belt. One reflection package is observed in this box. Stretched horizontally 6:1.

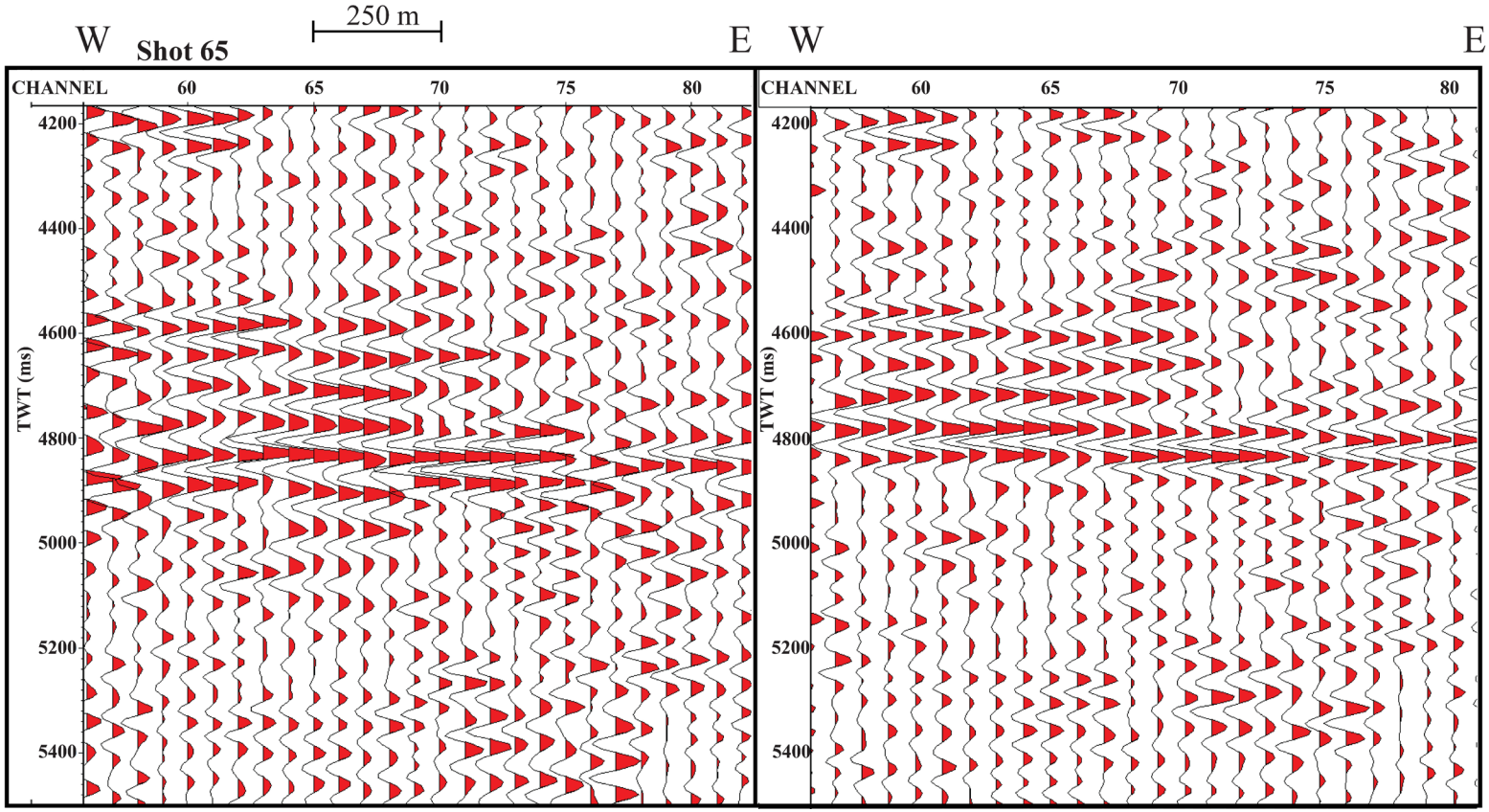

Figure 37. A comparison showing the effects of applying crooked line corrections to reflection data. Filtered data without crooked line binning is shown (Left) and the same data is shown with crooked line binning applied (right).

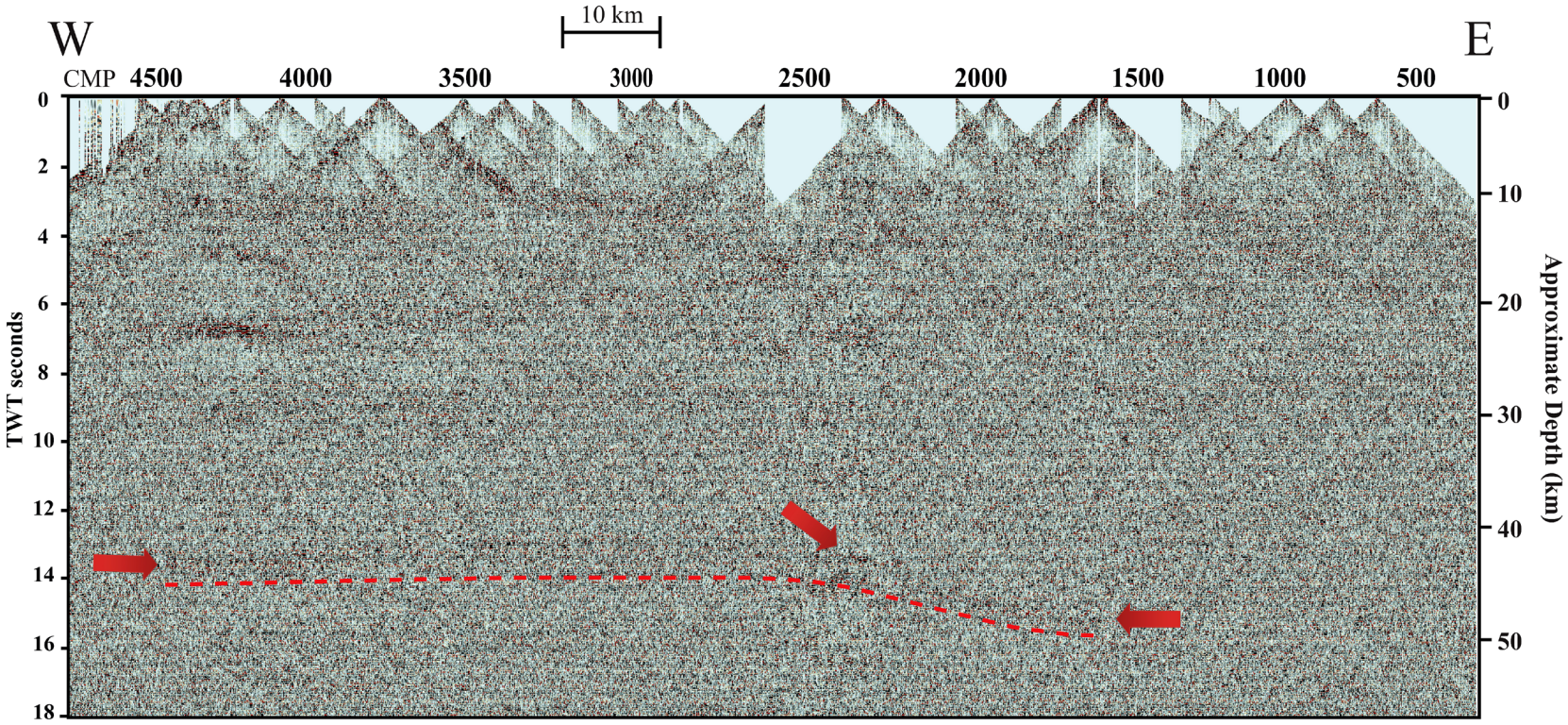

Figure 38. Stacked data from the fold and thrust belt with all static corrections and crooked line binning applied prior to stacking. The Moho's lateral extent is shown by the red line the red arrows. Note the dip starting beneath CMP 2500.

4500 to CMP 500 at 13000 to 17000 ms TWT (Figure 39). Similar continuous reflections are observed from CMP 4500 to 1700 at approximately 14000 ms TWT. These reflections begin to dip eastward at approximately 20 degrees beneath CMP 2500 and terminate beneath CMP 1500 at approximately 16000 ms TWT. Additionally, several scattered reflections are observed from CMP 1500 to 300 at approximately 16000 ms TWT (Figure 39).

Line Migration

The migration equation (Equation (1)) was applied to the eastern portion of the reflections starting under CMP 2500 at 14000 ms TWT (Figure 40). The first reflectors from CMP 2500 to 2000 at 13000 ms required a velocity input of 9000 to 10000 m/s to migrate them nearly horizontal (Figure 40, Green endpoints). The scattered reflections from CMP 1000 to 500 at less than 14000 ms required a migration velocity of 11,000 m/s to be nearly horizontal (Figure 40, orange endpoints).

Interpretations

The deep reflections observed between approximately 13 and 16 s TWT in the stacked section are interpreted to be reflections from the Moho (Figure 41). These reflections mark the point at which the deepest lateral crustal reflections are found at travel times consistent with estimates of crustal thickness (Cook et al., 2010; Klemperer et al., 1986). These reflections occur in an approximately 3 km thick band (1 s TWT) along the entire boundary (Figures A1 – A5). The re-processed data suggests that the Moho has a downward, concave dip trending 15 to 20 degrees east (Figure A4). The dipping Moho then appears to become more horizontal at ~50 km depth in the east (Figure A5). Furthermore, the plot of deep reflection endpoints available from individual

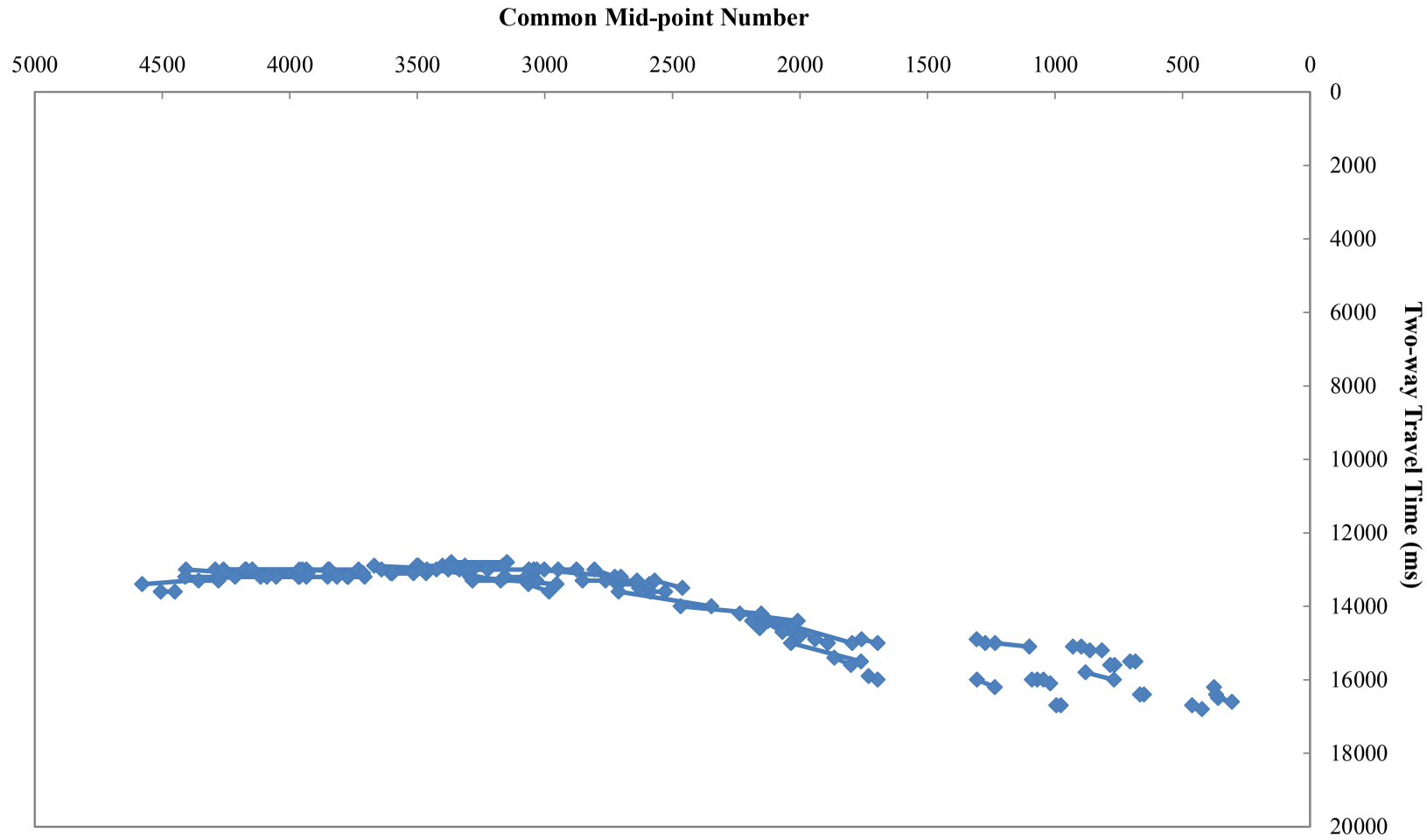

Figure 39. Deep reflection endpoints that were recorded and plotted. Endpoints were gathered from individual shot analysis.

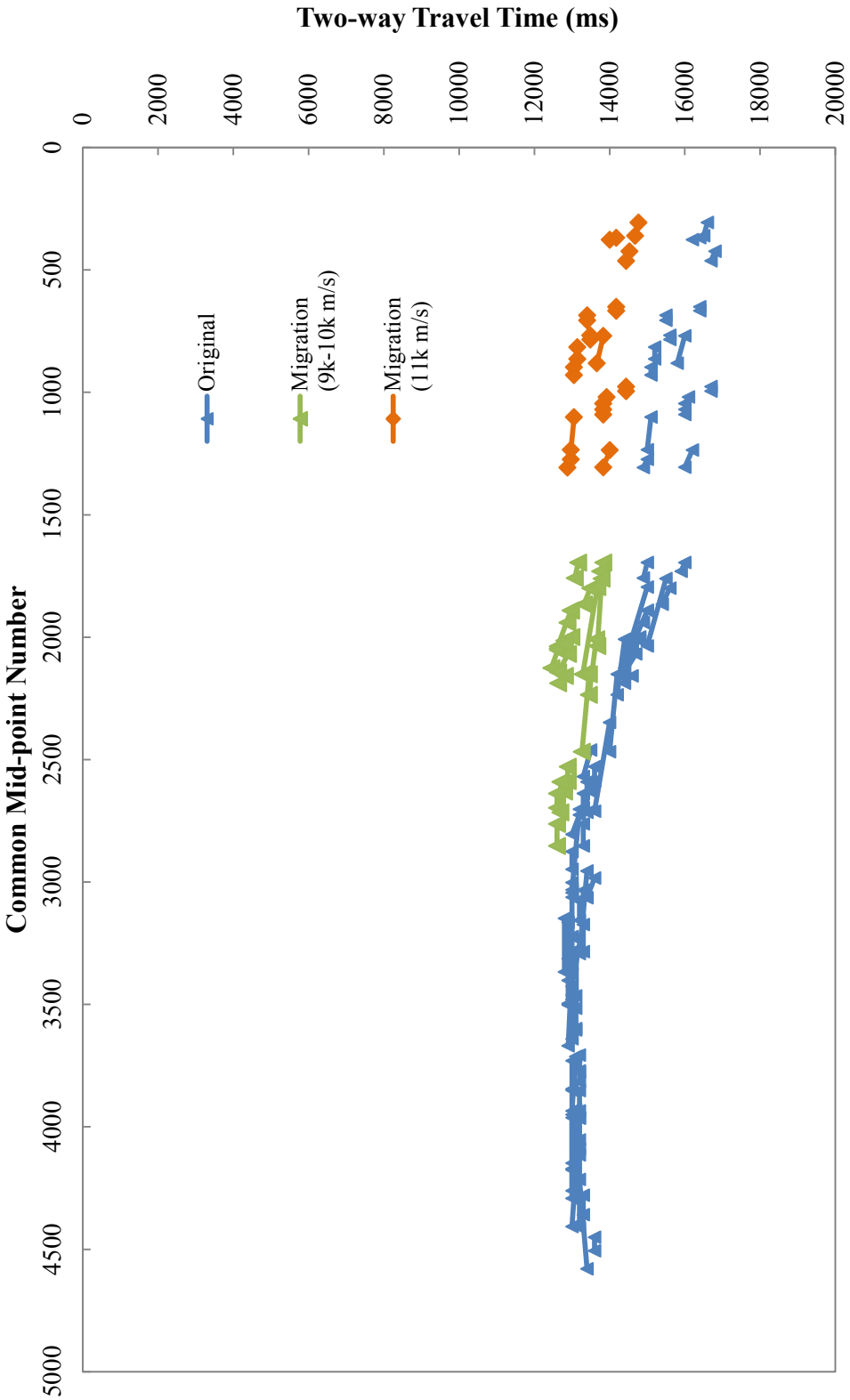

Figure 40. Manual migration of the deep reflections gathered from individual shot inspection.

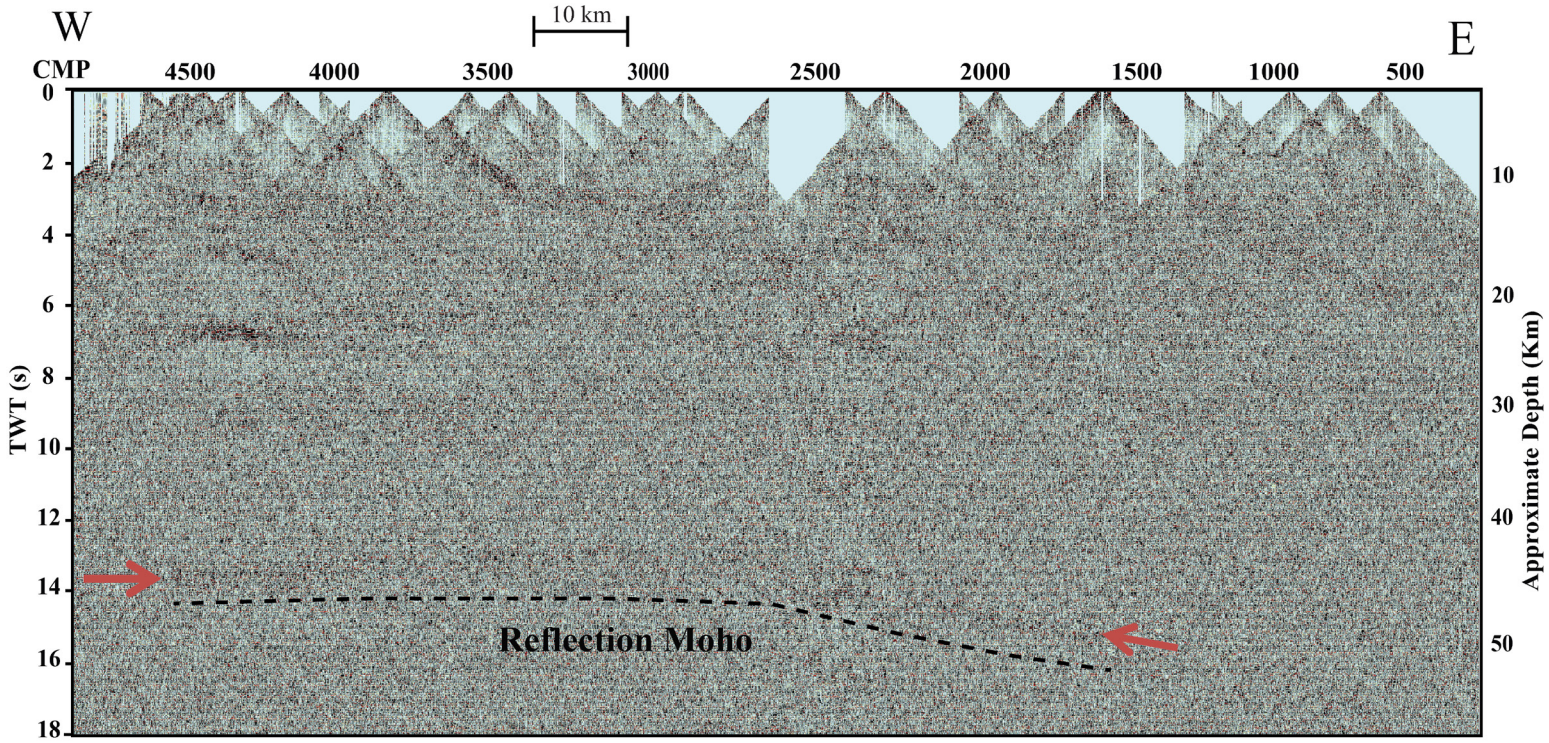

Figure 41. The reflection Moho visible in the re-processed stacked data from the fold and thrust belt.

shot inspection also shows the lateral extent of the reflection Moho (Figure 42). The continuous portion of the Moho observed in the plot is consistent with the lateral extent of the reflection Moho present in the stacked data (Figure 42, A). The scattered reflections observed from CMP 1500 to 500 in the individual shot data were not visible in the stacked data and the Moho is not observed in this region (Figure 42, B). This region represents a transition zone from reflective to diffuse, non-reflective Moho. The Moho can still be interpreted to continue east since it is a continuous worldwide boundary between the crust and mantle (Cook et al., 2010). The diffuse, non-reflective nature of the Moho has been interpreted to be the result of either massive magmatic underplating or eclogite in the deeper crust (Nelson, 1991; Baird et al., 1995).

The dipping Moho can be interpreted to represent a remnant collisional subduction zone (Balling, 2000; BABEL Working Group, 1990). Similar subhorizontal Moho structures, imaged beneath northwestern Europe and the Canadian Shield, have been interpreted to be the remains of ancient subduction zones (Balling 2000; Cook et al., 2010). Furthermore, the eastward dip of the Moho beneath the fold and thrust belt is also consistent with the East European plate being subducted east beneath the Magnitogorsk arc during the Paleozoic (Puchkov, 2009).

The 3 km thick lamination and lateral discontinuity of the reflection Moho observed in the basement of the fold and thrust belt is often observed in orogenic regions. This reflectivity can be interpreted to be the result of mafic sills intruded into the lower crust (Prussen, 1991; Jarchow et al., 1993; Eaton, 2006; Thybo and Nielson, 2012; Thybo and Artemieva, 2013). Therefore the Moho observed here may be the result of mafic sills that were intruded into the basement rock of the fold and thrust belt (Figure 43).

The shallow crust of the fold and thrust belt contains several reflection sequences that are consistent with west verging thrusts and eastward subduction of the crust (Figures A6 – A10). Potential thrust fault structures were identified in the shallow, western portion of

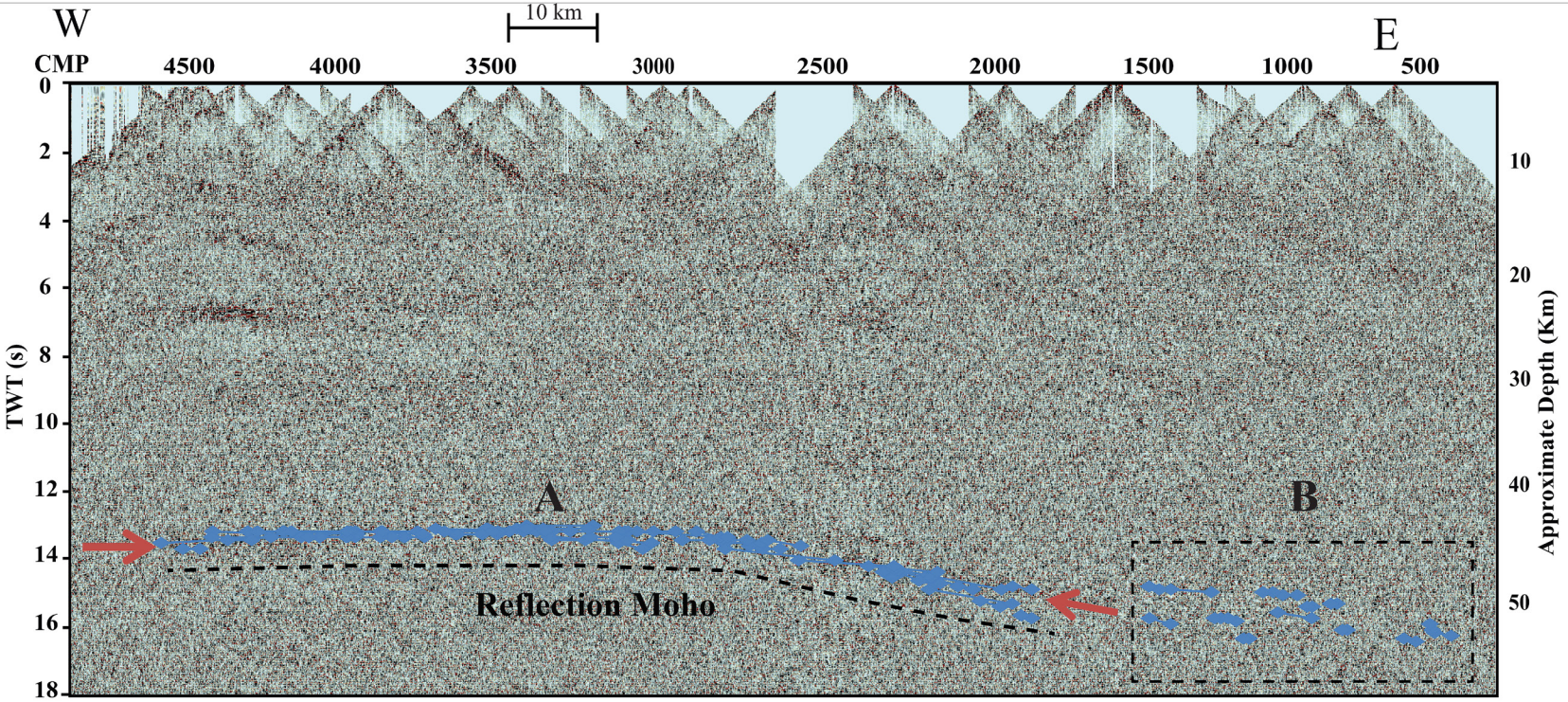

Figure 42. Moho reflection endpoints from individual shot inpsection transposed onto the stacked data. (A) The laterally continuous portion of the reflection Moho. (B) Scattered reflections that may be associated with the Moho boundary.

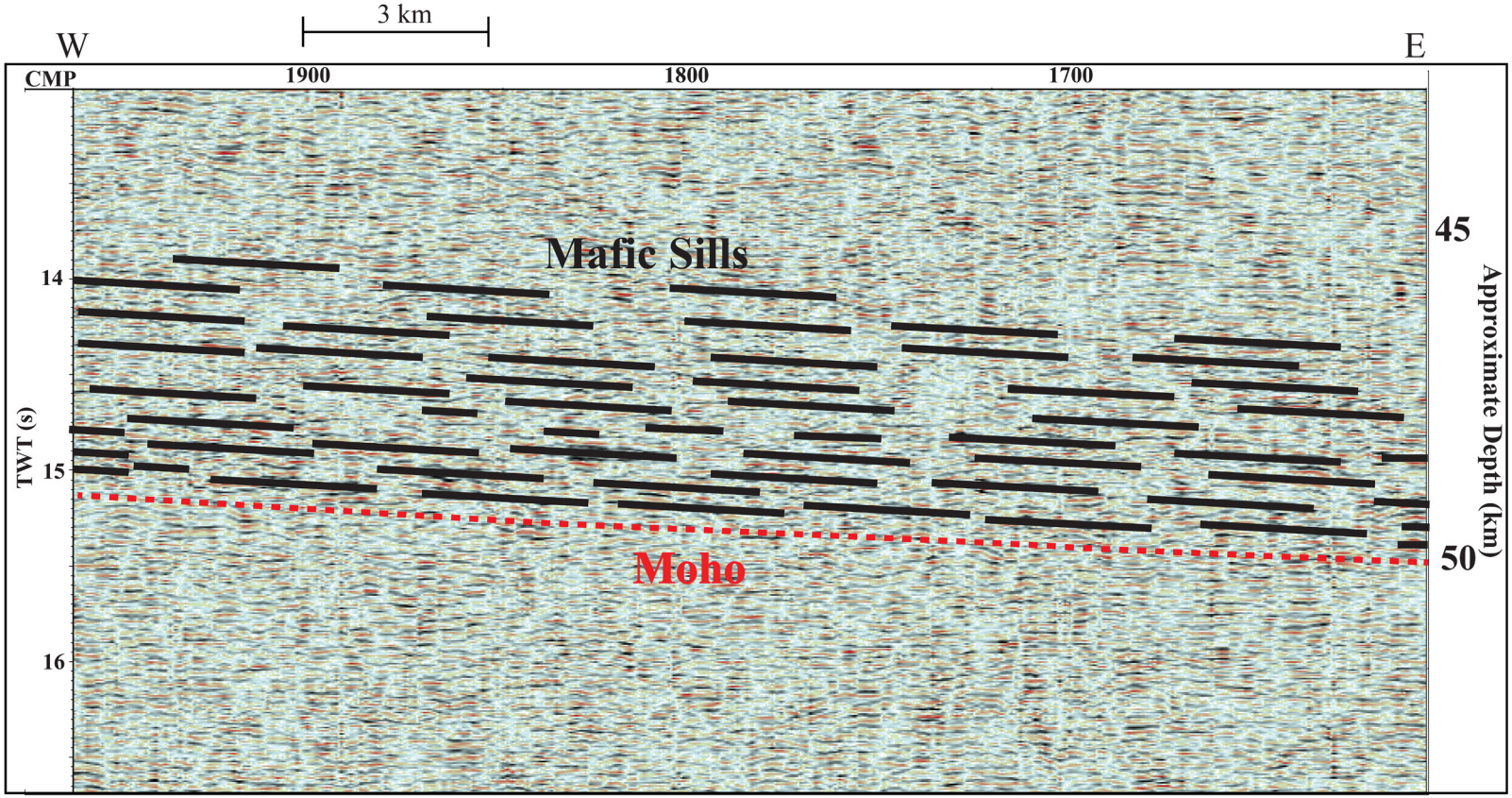

Figure 43. Mafic sills that likely comprise the reflection Moho. Note that the Moho is the boundary between the crust and mantle which is interpreted to occur where these reflections terminate.

the stacked data based on observed reflections (Figures A6 and A7). Additional faults and an exhumed Archean basement slab were identified in the shallow, central portion of the stacked data (Figure A8 – A10). Additionally, a thrust fault was identified in the shallow, eastern portion of the fold and thrust belt (Figure A11). All thrust faults in this region are interpreted to dip eastward at angles of near or less than 45 degrees. These fault structures agree with and eastward subduction of the East European Craton's crust (Puchkov, 2009).

An interpreted model for the geologic and tectonic structure of the southern Urals fold and thrust belt has been created based on reflections observed in the stacked data (Figure 44, A). The new model is consistent with previous geologic and seismic data interpretations (Berzin et al., 1997; Brown et al., 1997; Brown et al., 2008). In addition, combined geologic interpretations of the crust and Moho are shown for the fold and thrust belt (Figure 44, B). The implications of the seismic data results and interpretations will be discussed in the next section.

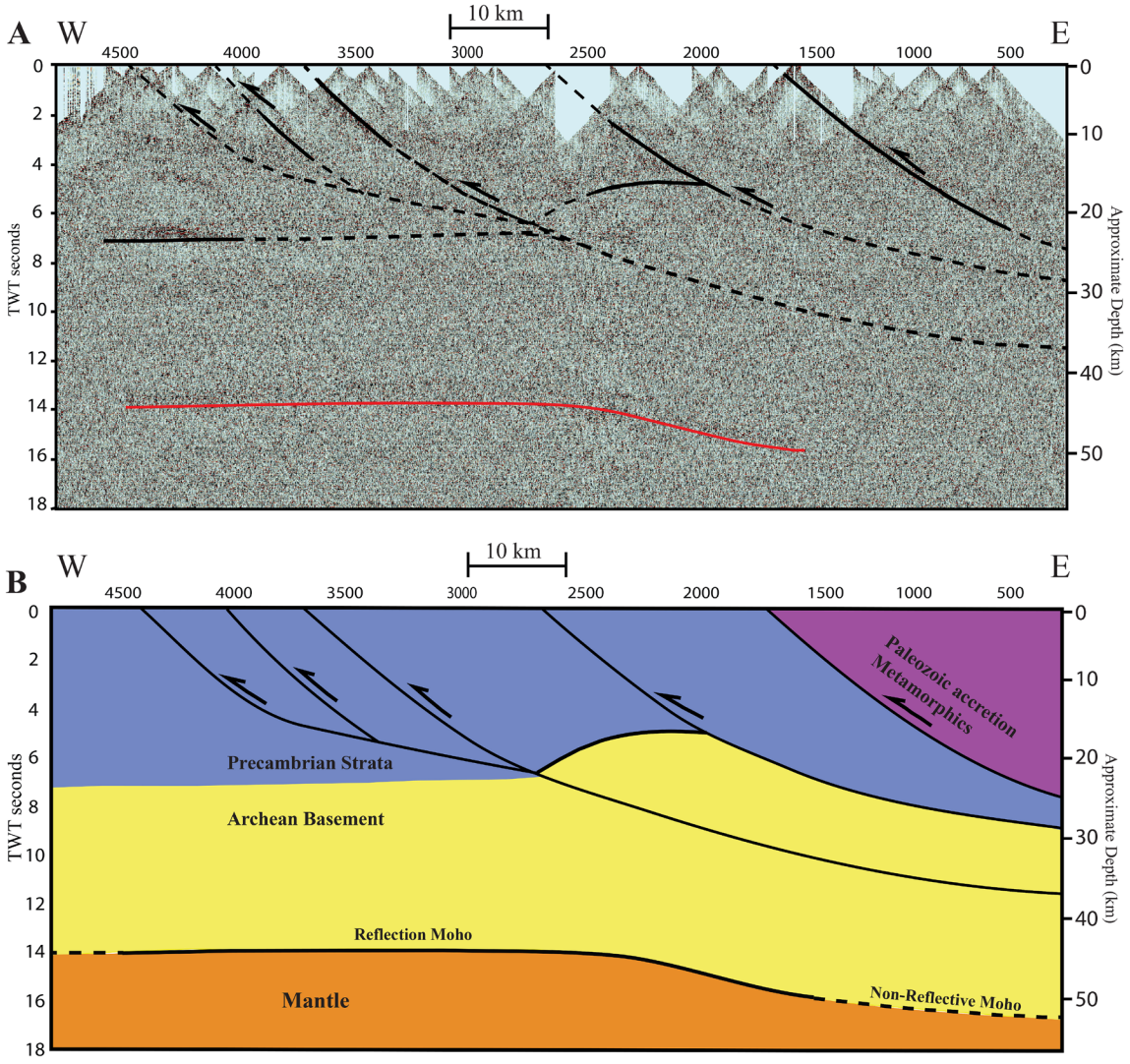

Figure 44. Interpretations of the Moho and crustal structures based on re-processed stacked seismic reflection data from the fold and thrust belt. (A) Interpretations of the reprocessed stacked reflection data. Faults are shown (black) as well as the Moho (red). (B) A cartoon of the crust and Moho. The crust has been generalized into Precambrian, Paleozoic, and Archean lithology (After Berzin et al., 1996; Brown et al., 1997; Matte, 2006).

CHAPTER IV
DISCUSSION

Previous interpretations of seismic reflection data from the Uralian fold and thrust belt depict a reflective upper crust underlain by a subhorizontal Moho that becomes non-reflective toward the crustal root (Berzin et al., 1996; Steer et al., 1998). These interpretations are consistent with the new interpretations of re-processed reflection data which identified west verging thrust faults in the upper crust and a ~3 km thick band of laterally varying reflections in the deep crust that constrain the Moho. The subhorizontal geometry of the Moho is interpreted to be the result of eastward subduction and bending of the east European crust (Puchkov, 2009, 2013). The laminated reflections overlying the Moho are interpreted to be the result of mafic sills emplaced in the lower crust (Nelson, 1991; Warner, 1990b). Furthermore, the non-reflective character of the Moho beneath the east most portion of the fold and thrust belt is interpreted to be the result of either eclogite or magmatic underplating (Nelson, 1991; Baird et al., 1995).

Subhorizontal Moho

The subhorizontal Moho imaged beneath the eastern portion of the fold and thrust belt is supported by velocity pushdown analysis and manual depth migration. Velocity pushdown was a suspected cause of the sub horizontal Moho reflections beneath the eastern portion of the fold and thrust belt but is not likely the case. Velocity push-down occurs when acoustic velocities are slower in an adjacent portion of the study area

resulting in what appears to be a structural low in the imaged reflector (Yilmaz, 2001). Average velocities were tested through trial and error to "pushup" the sub horizontal Moho reflections to a depth (~45 km) similar to the Moho in the west and central portion of the fold and thrust belt (Figure 45). The observed Moho reflection endpoints were converted to depth using the southern Urals' average crustal velocity (6.6 km/s, Carbonell et al., 2000) (Figure 45, blue line). The deepest reflections from CMP 500 to 300 required 5.5 km/s to reach ~45 km depth (Figure 45, red endpoints). Deep reflections from CMP 1000 to 500 required 5.7km/s and 5.8 km/s respectively (Figure 45, purple and green endpoints). The shallower, subhorizontal reflections from CMP 2500 to 1700 required an average velocity of 6.2 km/s to reach ~ 45 km depth (Figure 45, orange endpoints). The velocities necessary to pushup the reflections are lower than both the average Southern Ural and average global crustal velocities (global: 6.45 km/s, Christensen and Mooney, 1995; Urals: 6.6 km/s, Carbonell et al., 2000). Averaging the lowest possible velocities in the southern Ural crust still yields a velocity of ~6.4km/s (Figure 46). Based on the difference between observed and tested velocities, it does not seem viable that velocity pushdown was responsible for the eastward dip of the Moho.

Manual Migration accounted for the effects of dip and velocity on the Moho reflections and verified the geometry of the Moho observed in reflection processing. The migration equation relies on the seismic velocity that would correspond to the reflections' depths. The velocities (9-11 km/s) required to move reflections to a horizontal position are not possible based on known crustal, Moho, and upper mantle velocities for the southern Urals and the world (Christensen and Mooney, 1995; Carbonell et al., 2000; Cook et al., 2010). Manual dip migration did not flatten the Moho's geometry in this region, rather it is consistent with an eastward dipping Moho (Figure 47).

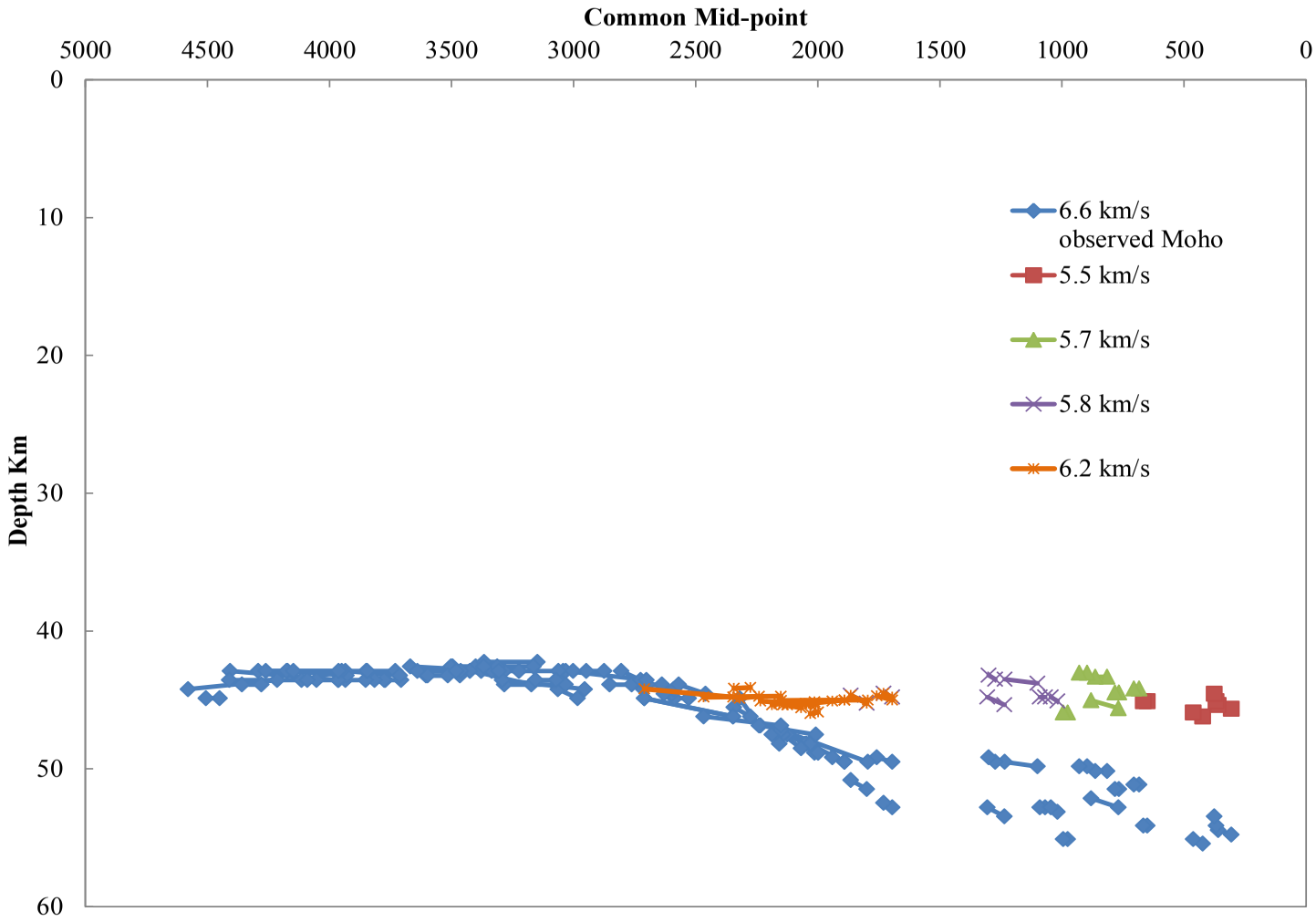

Figure 45. Velocity push-down analysis of the Moho reflectors taken from individual shot analysis.

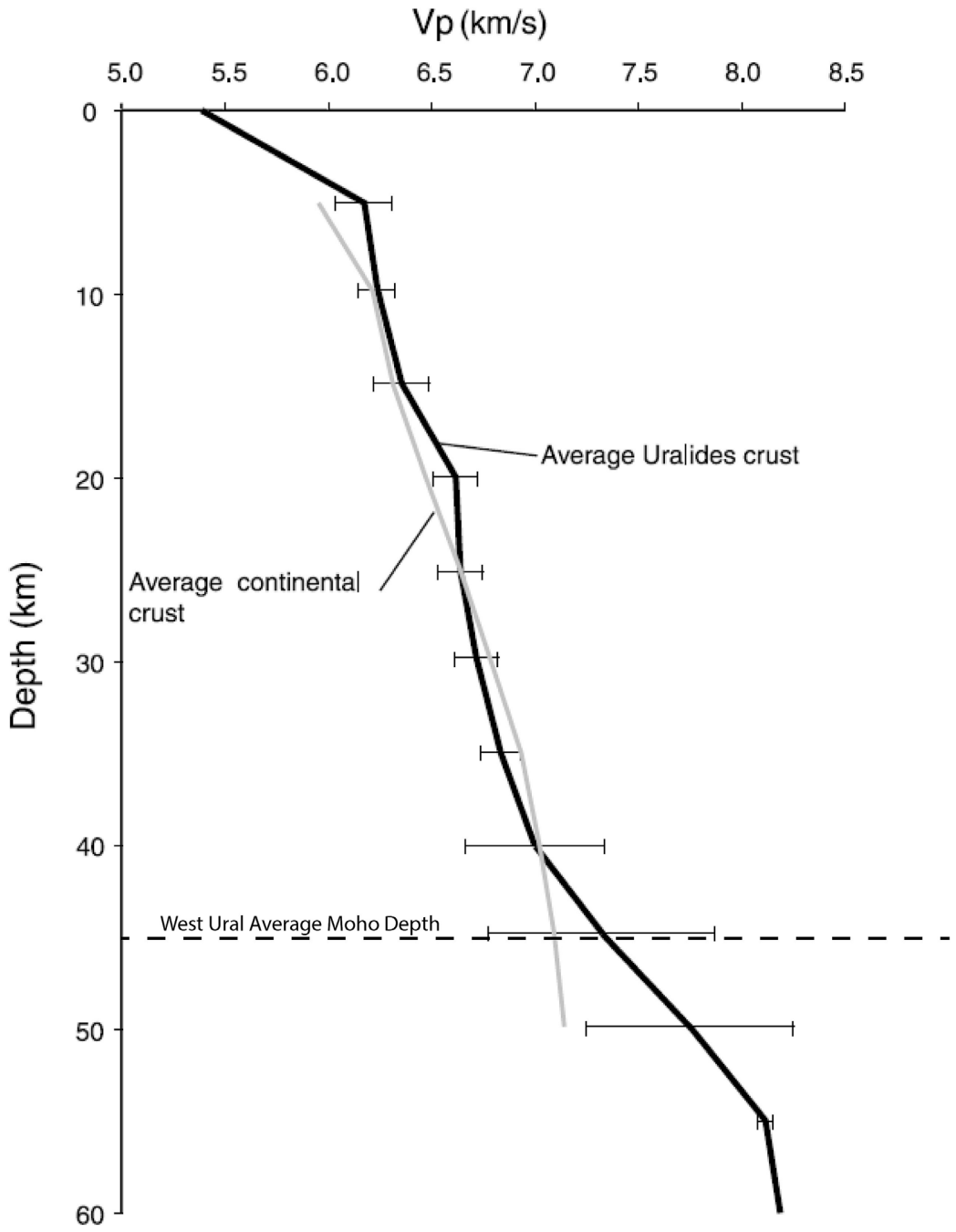

Figure 46. Comparison of average global crustal P-wave velocities to average Ural crust P-wave velocities (from Brown et al., 2003). Horizontal lines represent a standard deviation in the average Ural crust velocities at 5 km intervals. The average depth of the Moho (crustal thickness) beneath the fold and thrust belt is shown at ~45 km (after Carbonell et al., 2000). Averaging all of the lowest possible velocities from the standard deviations yields ~6.4 km/s.

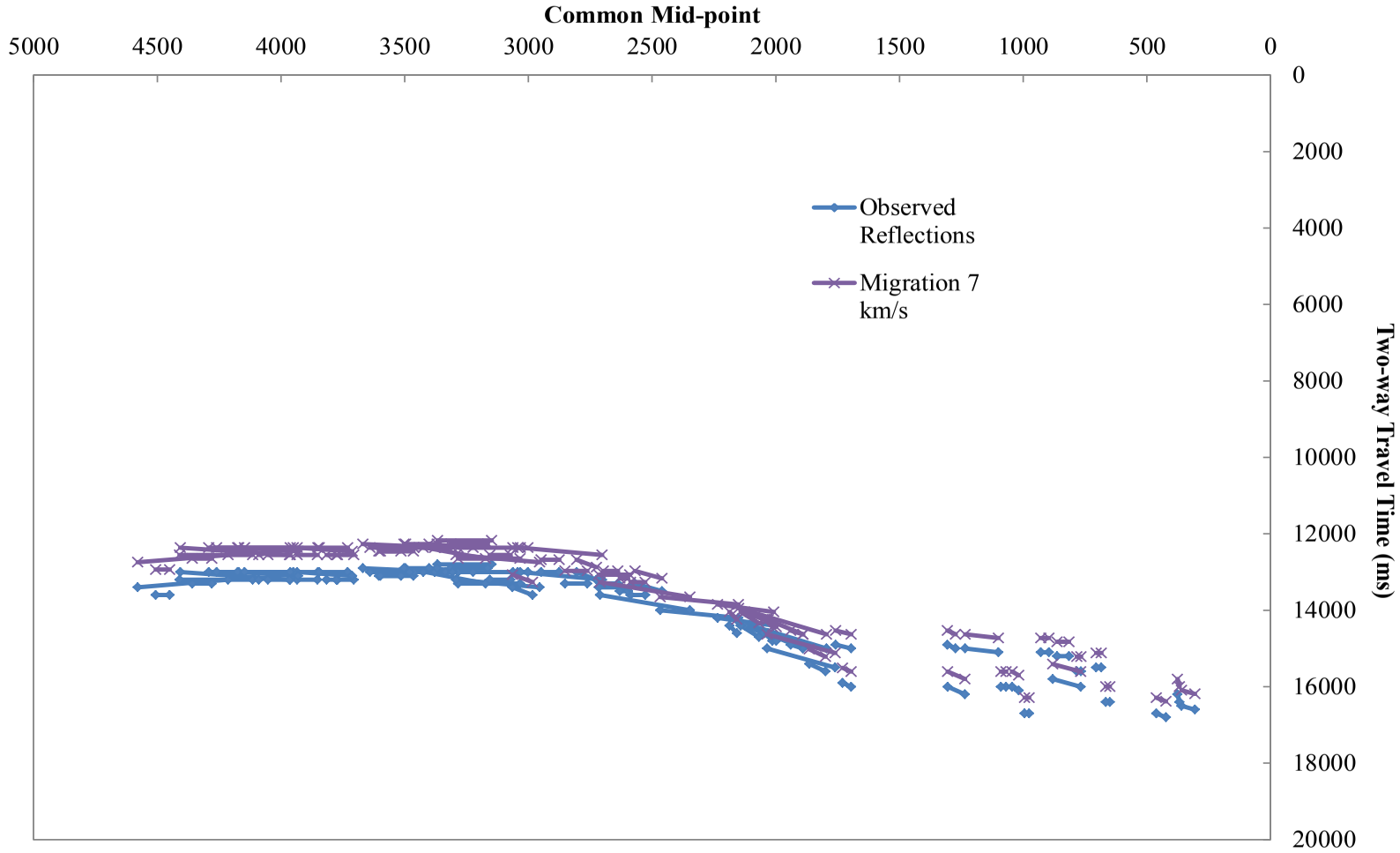

Figure 47. Migration of Moho reflection endpoints. These have been migrated using a known velocity of ~7 km/s for the deepest portion of the crust (Carbonell et al., 1998, 2000). The dipping reflections remain in a sub horizontal orientation.

Laminated Moho Reflections

Magmatic underplating is proposed to have occurred across much of the continental lithosphere during the Proterozoic (Fyfe, 1978; Furlong and Fountain, 1986; Fyfe, 1992; Thybo and Artemieva, 2013). The emplacement of sills by magmatic underplating has been used by other authors as a means to explain the horizontal reflectivity in the deep crust (Thybo et al., 2000; Clowes et al., 2002; McBride et al., 2004). For instance, Lithoprobe seismic refraction experiments in North America have identified a laminated lower crust thought to be the result of mafic sills emplaced in the Archean basements (Clowes et al., 2002). The reflectivity of mafic sills is proposed to be the result of high impedance contrasts when compared to the surrounding rock that comprises the lower crust (Warner, 1990a; 1990b). The data and images here support the contention that the Moho in this region contains mafic sills.

Non-Reflective Moho

Ray tracing was used to determine if the lack of Moho reflections beneath the eastern portion of the fold and thrust belt is the result of far offset ray paths. According to Steer et al. (1998), shot energy penetration in the region of the fold and thrust belt should have been sufficient to image the entire crust (25-30 s TWT). It is more likely that the subhorizontal position of Moho reflectors (in this case the mafic sills) caused reflections to arrive at offsets greater than 18 km receiver spread. However, ray trace models do not entirely agree with this case. The first 25 shots in the fold and thrust belt were recorded within the region of the subhorizontal Moho. The receiver line for Shot 1 recorded rays over the non-reflective region but did not image reflections directly from the interpreted Moho boundary (Figure 48). The first 9 shots were similar to shot 1 and only some of

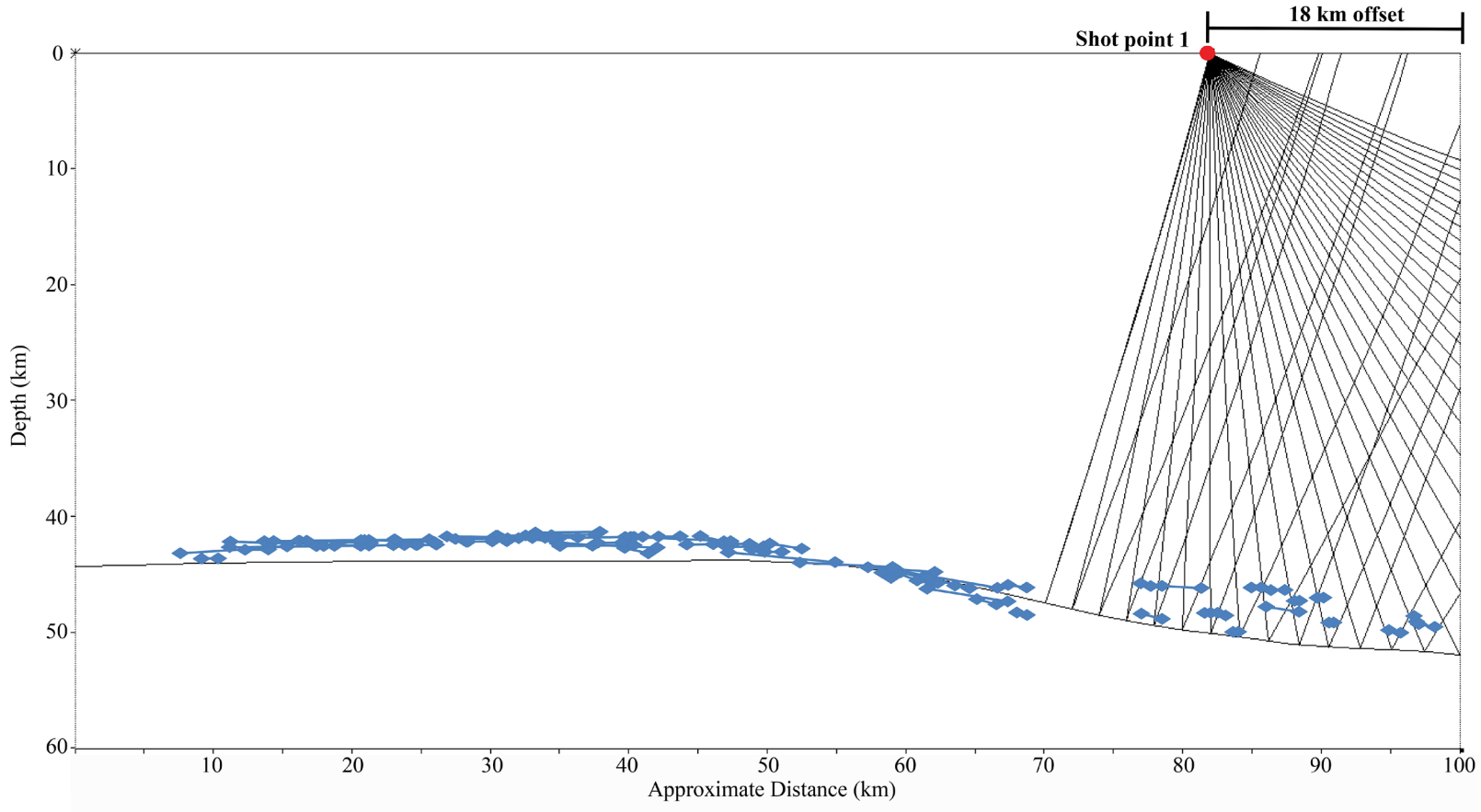

Figure 48. A comparison between the MacRay model for shot 1 and the reflection endpoint data. Rays are received but very few reflections are imaged. Shots 1-9 had similar results.

the rays for these shots would have been reflected far from the receiver offset. In contrast Shots farther west (10-25) should have recorded Moho reflections (Figures 49 and 50). It is evident from the ray trace models that more Moho reflections should have been observed in the east portion of the data if the Moho were reflective.

Although it is outside the scope of this paper, Steer et al. (1998) noted that the Moho maintained a non-reflective character in near vertical reflection data throughout the entire root of the southern Urals. In contrast, Carbonell et al. (1998) did image the Moho in wide angle data and it appeared relatively horizontal at ~53 km depth in the central root. It is apparent from this information that the reflective nature of the Moho beneath the southern Urals is not governed solely by its geometry. In other words, the non-reflectivity of both horizontal and subhorizontal Moho may be the result of the deep crustal geology.

Geologic Evidence

The non-reflective character of the Moho interpreted in the east portion of the data is consistent with other geophysical data and is usually attributed to either massive magmatic underplating or a gradual phase transition from crustal mafic rock into eclogite (Nelson, 1991; Baird et al., 1995). A mafic body resulting from magmatic underplating would be mostly transparent in near vertical reflection data (Nelson, 1991). However, wide angle reflections would have laterally imaged the top and bottom of a massive igneous body and recorded internal velocities much higher than 7 km/s (White, 1988; Nelson, 1991). Carbonell et al. (1998, 2000) noted no such structure or velocities (Except the Moho jump from ~7 to 8 km/s) in the wide angle seismic data beneath the western region of the southern Urals. Furthermore, seismic velocity, gravity, heat flow, and magnetic data collected in other studies identified characteristics of a lower crust consisting primarily of metamorphic rocks and not mafic intrusions (Brown et al., 2003;

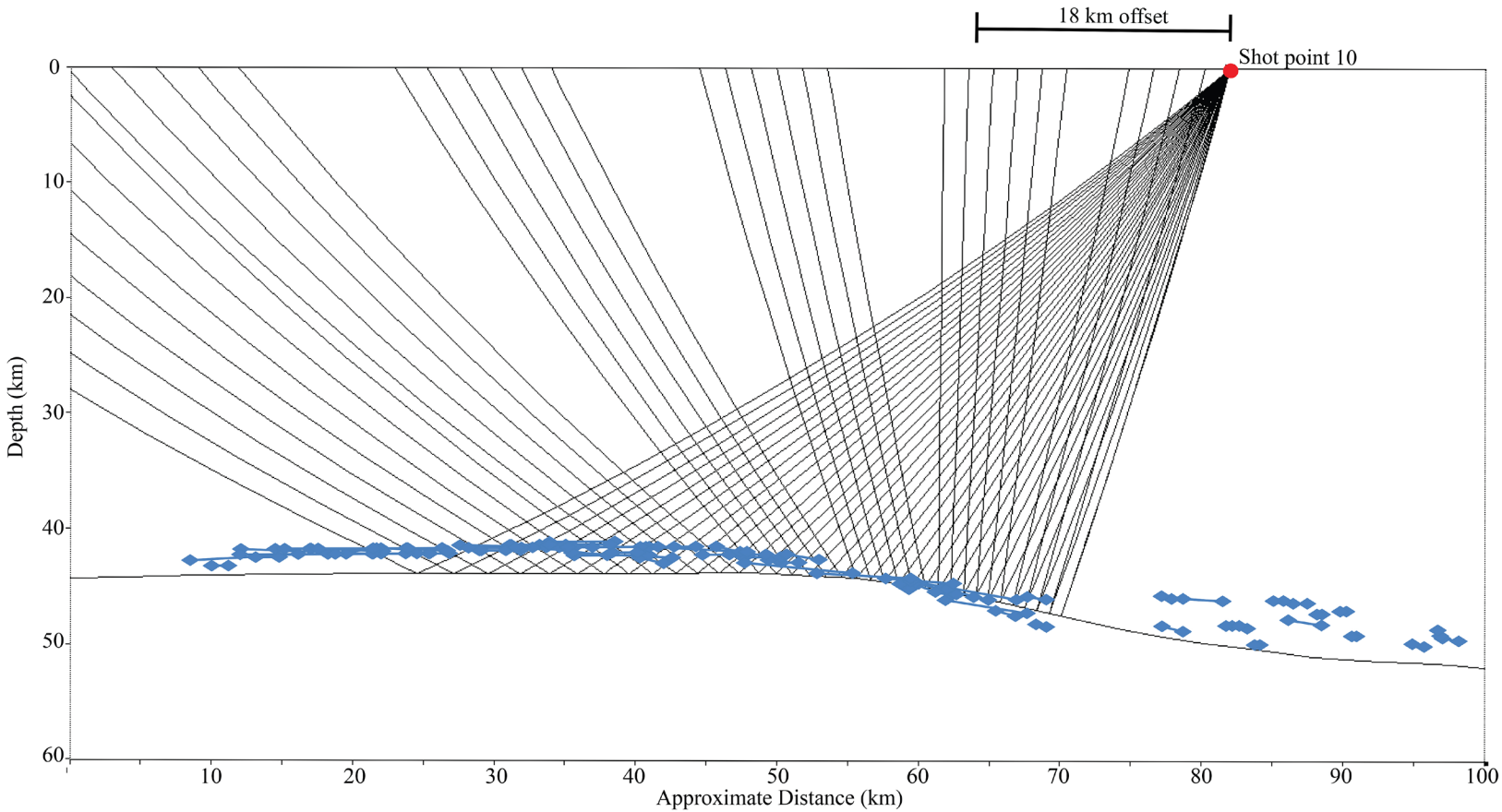

Figure 49. Shot 10 from the ray trace models compared to reflection endpoint data. Here it is clear that rays were received within the 18 km offser and reflections were observed.

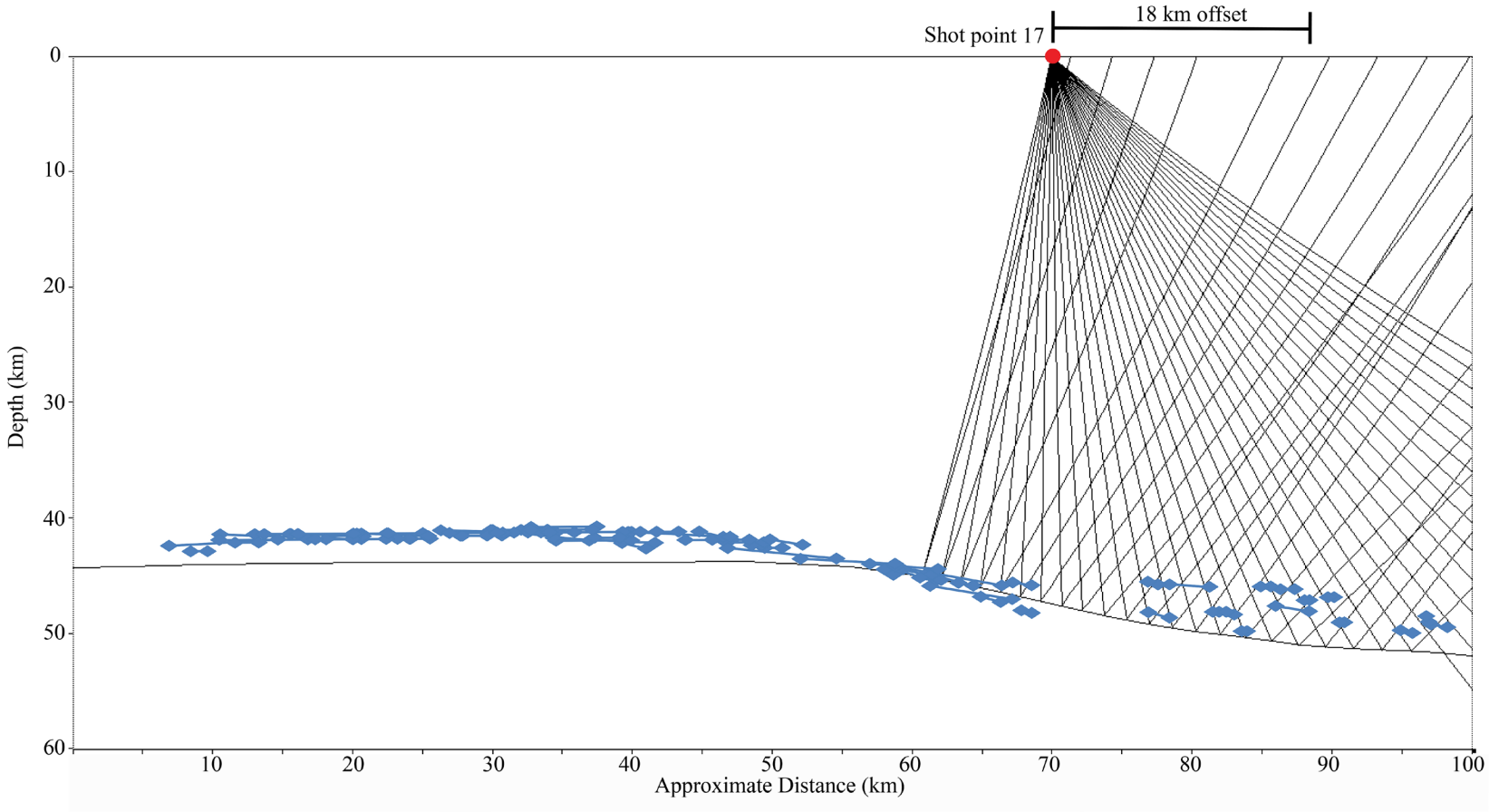

Figure 50. Shot 17 from the ray trace models compared to reflection endpoint data. Again it is clear that rays were received within the 18 km offset and reflections were observed.

Brown et al., 2008). The crustal model from Brown et al. (2008) was combined with the interpretations from this study to constrain the composition of the crust beneath the fold and thrust belt (Figure 51). Particularly, the lower crust beneath the fold and thrust belt has been interpreted to consist primarily of mafic granulite or amphibolite (Brown et al., 2003). An additional study completed by Russian scientists is consistent with a lower crust comprised of mafic granulite with potential inclusions of eclogite in the deepest crust (Kukkonen et al., 1997). The low heat flow in the Urals observed by Kukkonen et al. (1997) is not consistent with a massive mafic intrusion.

Ruling out the presence of a massive mafic intrusion, an eclogite metamorphic front is a more plausible case for the non-reflective Moho. The observations of the Moho in the southern Urals are similar to those made in the Trans-Hudson orogeny where the lack of Moho reflections was interpreted to be the result of eclogite (Baird et al., 1995). A similar non-reflective, eclogitized Moho was also interpreted in the Central Alps (Laubscher, 1990; Austrheim, 1991; Bousquet et al., 1997). Eclogite is a high pressure metamorphic rock favored by pressures greater than 1.3 Gpa (10 kbar) and temperatures greater than 500-600^{0}C (Austrheim, 1991; Spear, 1993). The temperature and pressure conditions where the Moho is not imaged beneath the fold and thrust belt (Figure 52) are similar to conditions observed in many places around the world where subducted or thickened crustal zones have exceeded 50 km depth and eclogite is thought to have formed (Austrheim, 1991; Spear, 1993; Fountain et al., 1994; Hynes and Snyder, 1995; Poli and Schmidt, 1997; Schreyer and Stockhert, 1997; Knapp and Diaconescu, 2002). The non-reflective nature of eclogite in near vertical reflection data may be due to the effects of the eclogite neighboring mantle peridotites. The close proximity of eclogite to peridotite would not produce high enough reflection coefficients to image the boundary (Furlong and Fountain, 1986).

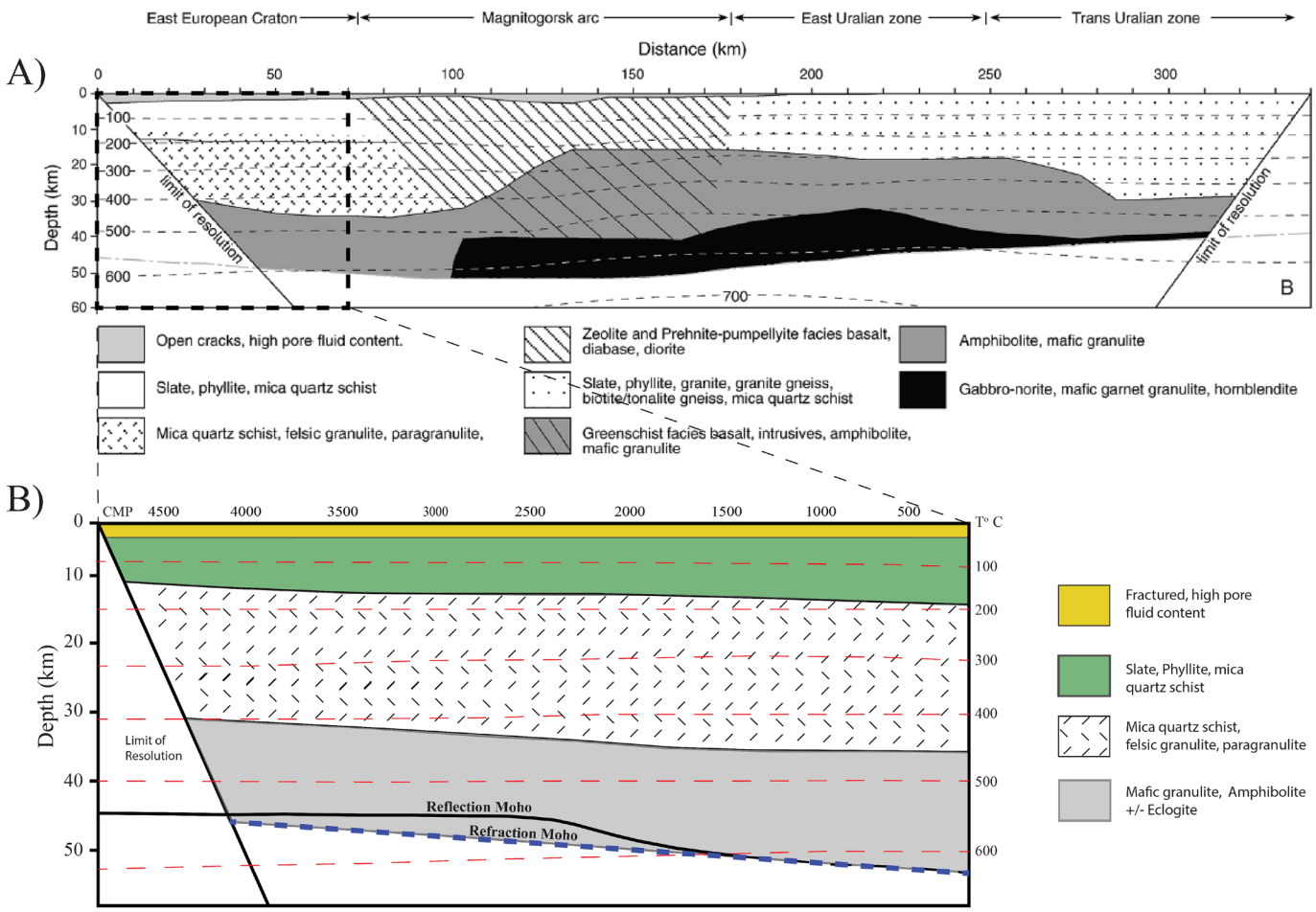

Figure 51. Southern Ural fold and thrust belt crustal composition data placed along with the interpreted reflection Moho from this study (Brown et al., 2008; Kukkonen et al., 1997). A) Original crustal data based on refraction, gravity, heat flow, and magnetic data (Brown et al., 2003, 2008). B) The crustal composition data placed into the fold and thrust belt study area. Note that the rock boundaries are estimates and do not represent definite boundaries or include offsets. Also note the difference between the interpreted reflection Moho and the refraction Moho used in the composition interpretation (Carbonell et al., 1998, 2000).

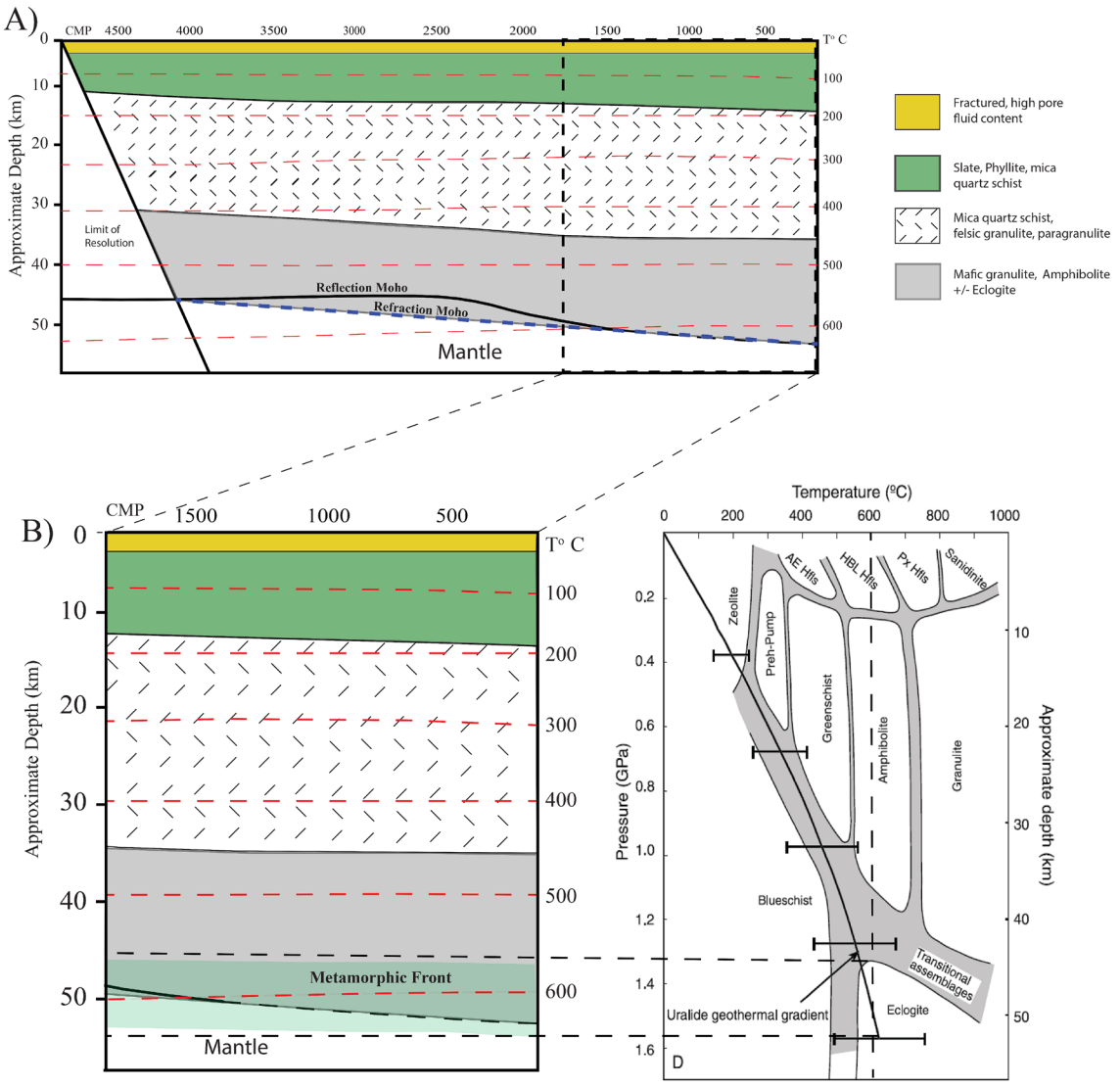

Figure 52. A comparison of the fold and thrust belt crustal composition data to Ural metamorphic conditions. A) Crustal composition data for the fold and thrust belt (after Brown et al., 2003, 2008). B) Comparison of the eastern portion of the fold and thrust belt to the Ural P-T chart (from Brown et al., 2003). Note that the metamorphic front has been based on the location of eclogite on the P-T chart. The interpreted non-reflective Moho within the front appears below 50 km depth and 600^{0}C where eclogite is favored.

Magnitotelluric Data

Magnitotelluric data from the Southern Urals (Diakonova, 2007) provide additional insight into this regions Moho and agree with the existence of eclogite in the deep crust. The Moho is defined as a step change in electrical conductivity, known as the electric Moho, that occurs at depth similar to the refraction Moho (Jones and Ferguson, 2001; Cook et al., 2010). Unfortunately, the conductivity of the lower crust likely masks any effective resistivity changes due to the Moho (Jones, 1992). However, there does appear to be a change in the resistivity where the Moho becomes non-reflective (Figure 53, orange box). The change in resistivity may be indicative of the presence of fluids from the lower crust and possibly upper mantle (Fyfe, 1986; Diakonova, 2007). These fluids may contribute to the formation of eclogite (anhydrous garnet-clinopyroxene assemblages) which may depend upon the presence of fluids in the deep crust (Austrheim, 1991; Poli and Schmidt, 1997).

Refraction Ray Tracing

The refraction Moho is the subsurface boundary where there is rapid jump in P wave velocity to an average of 8 km/s (Steinhart, 1967; Cook et al., 2010). This is observed in the southern Urals from wide angle seismic data (Thouvenot et al., 1995; Carbonell et al., 1998; Stadtlander et al., 1999). However, the refraction Moho interpretations are not consistent with the reflection Moho interpretations.

The Moho imaged in the wide angle refraction data of the southern Urals (Carbonell et al., 1996, 1998, 2000) did not match the image in the reflection data (Berzin et al., 1996; Steer et al., 1998). The refraction ray traces plotted against the crustal and Moho data from this paper show low resolution along the Moho boundary (Figure 54). No

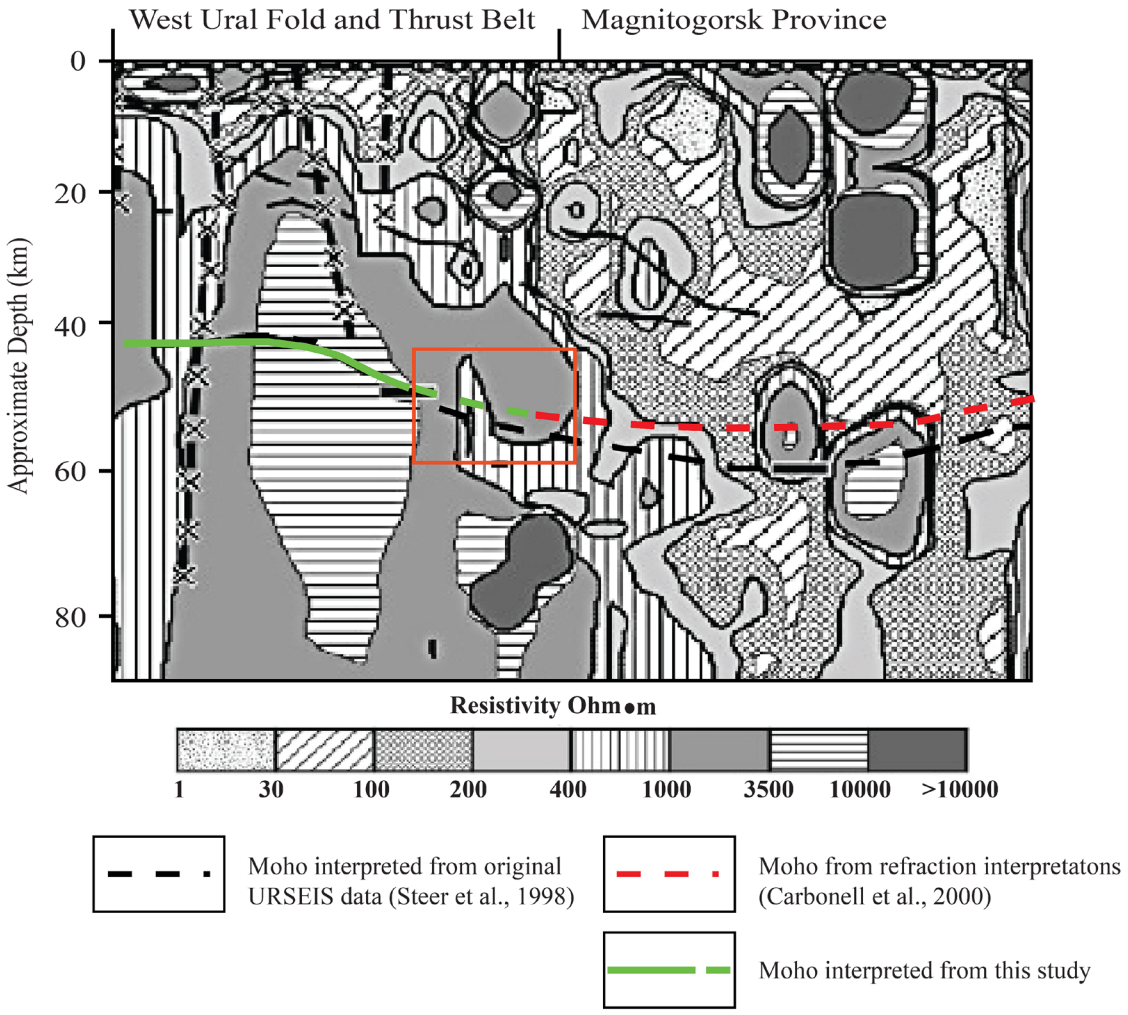

Figure 53. Magnitotelluric data of the fold and thrust belt and Magnitogorsk Province along the URSEIS transect (modified from Diakonova et al., 2007). Notice the mixture of low and high resistance where the Moho becomes non reflective (orange box).

rays are refracted from the first 40 km along the Moho boundary (Figure 54, West Uralian Zone). The rays reflected from the Moho boundary occur from 50 to 150 km at ~50 km depth (Figure 54, Central zone and Magnitogorsk Arc). These rays are widely spaced, become farther apart to the east, and terminate beneath the Magnitogorsk arc at ~53 km depth. The Southern Ural wide angle experiment relied on a wide receiver spacing (2.5 km) and only 4 shot positions (Carbonell et al., 2000) which would likely smear the image of the Moho. In contrast, 6 fold acquisition, 360 channels per shot, and 50 m receiver spacing were used for the reflection experiment (Steer et al., 1998). Interpretations of the Moho beneath the fold and thrust belt would be most accurate when based on the reflection Moho (Figure 55).

Ural Wilson Cycle

The dipping nature of the Moho observed beneath the southern Urals fold and thrust belt may play a role in determining the tectonic state of the mountain belt. The Moho beneath the fold and thrust belt is similar to the Moho observed beneath other intact orogens and cratons around the world that have depressed; dipping natures associated with thickened crust and deep crustal roots (BABEL Working Group, 1990; Kissling, 1993; Németh et al., 1996; Henstock et al., 1998). The presence of the transition from reflective to non-reflective, eclogitized Moho interpreted beneath the fold and thrust belt may also be indicative of an uncollapsed, unextended orogeny. Work by Ryan and Dewey (1997) provides evidence that non-reflective eclogite occurs in non-collapsed, eroded orogens due to the eclogite's unstretched near-vertical layering. In contrast, collapsing orogens stretch the eclogite into sub-vertical layering that would become reflective in seismic experiments (Ryan and Dewey, 1997). Based on this information, the nature of the crust and Moho beneath the fold and thrust belt supports the intact, unextended nature

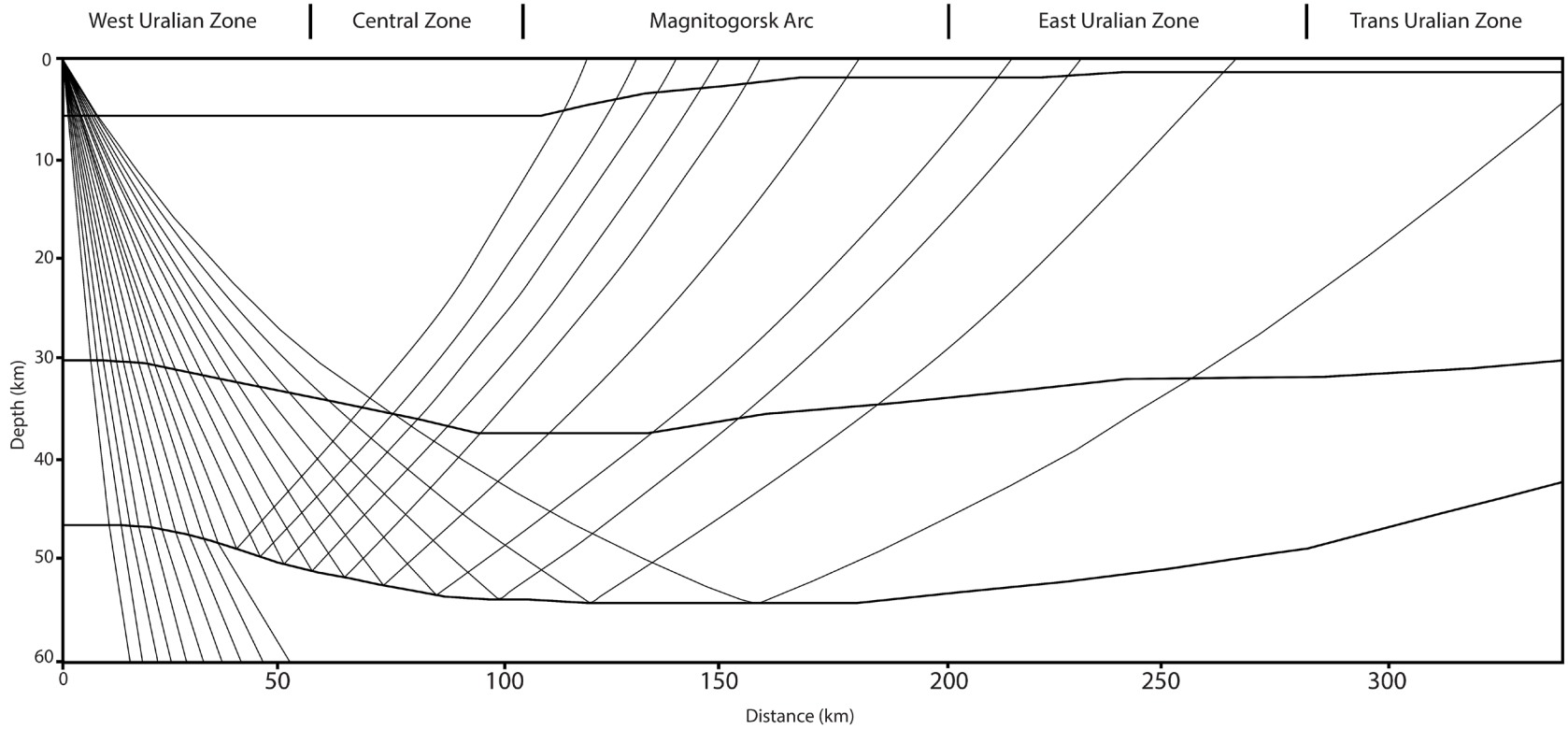

Figure 54. Refraction ray trace results from MacRay. This represents shot 1 from the wide angle experiment (Carbonell et al., 1998). This was the only wide angle shot to image the Moho beneath the fold and thrust belt (west and central Uralian zones). Note the lack of reflections beneath most of the west Ural Zone.

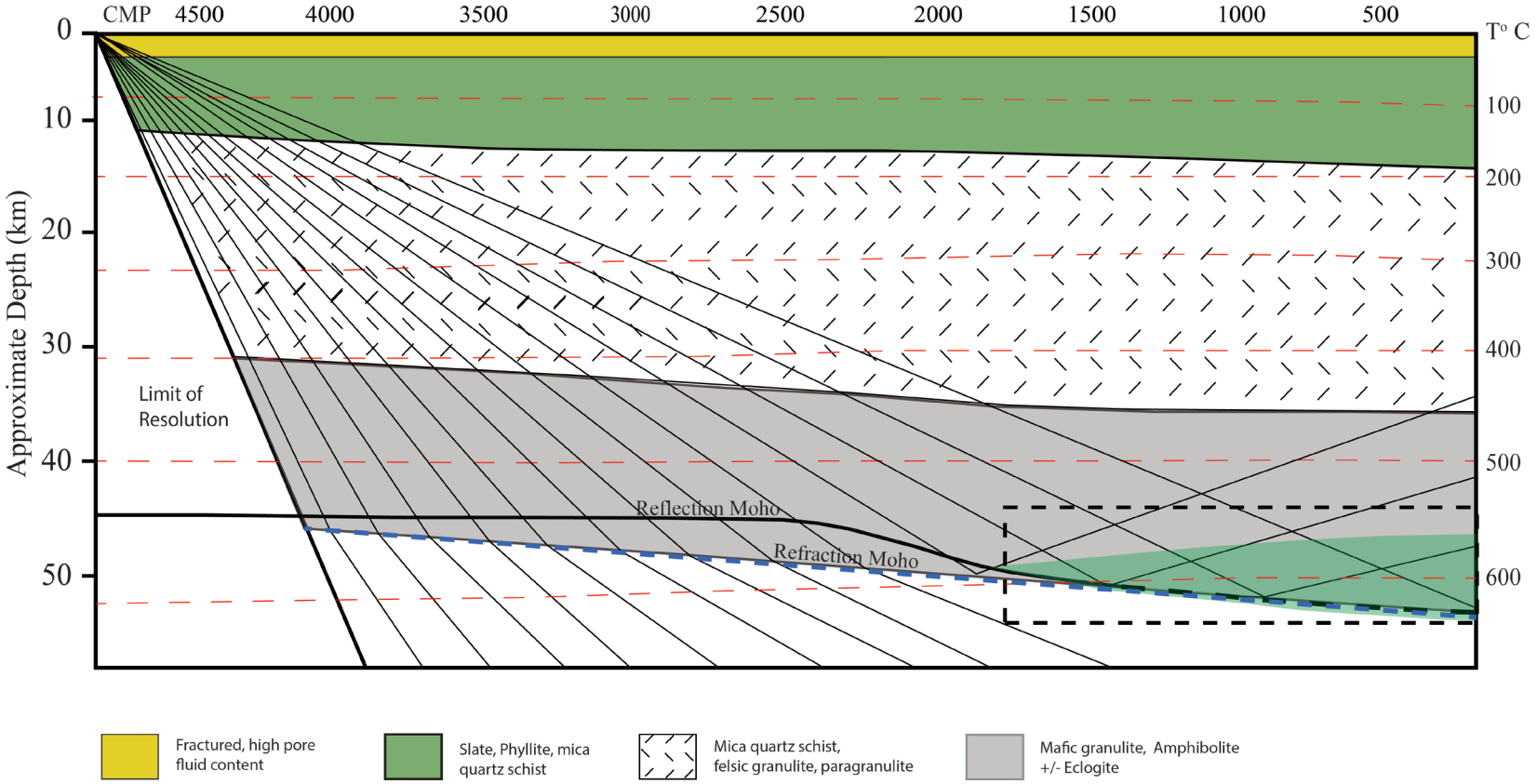

Figure 55. The refraction ray traces placed against the physical data. The reflection and refraction Moho do not match. The mismatch is attributed to a lack of refraction resolution along the Moho boundary. The depth and extent of the crustal composition data were based on the refraction Moho (Brown et al., 2003, 2008).

of the southern Urals (Figure 56). The mountain belt appears to remain in a state that resulted from the previous collisional stage of the Ural's Wilson cycle and a new stage of extension has not begun.

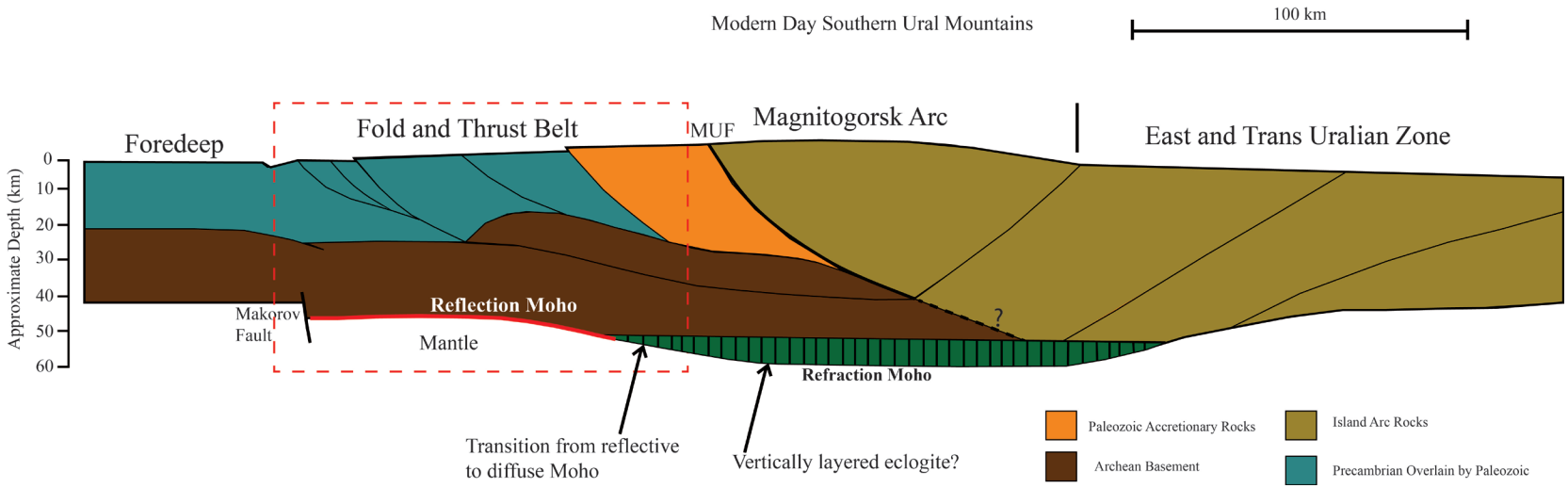

Figure 56. Interpreted tectonic structure of the southern Ural mountains (after Berzin et al., 1997). The reflection Moho from this study and the refraction Moho are shown (Carbonell et al., 2000). The bivergent structure of the crust, depressed, dipping Moho, and vertically layered eclogite indicate a lack of extension in the Urals. This structure is consistent with a stable, post collisional, pre-extensional stage of the Wilson cycle (Fichter, 2000).

CHAPTER V

CONCLUSIONS

Reprocessing of URSEIS explosive source seismic data from the Southern Urals fold and thrust belt is consistent with original processing and has provided new insight into the nature of the crust and Moho beneath this region. The upper portion of the crust (<30 km) appears dominated by several west verging fault structures. The fault structures in the crust overlie a predominantly mafic granulite basement that terminates at the base of a 3 km thick band of reflections that constrain the Moho in this region.

The complex geologic history of the Southern Urals, especially in the fold and thrust belt, has resulted in what appears to be a Moho that dips eastward towards the crustal root and becomes non-reflective. The seismic reflections interpreted as the Moho are likely the result of mafic sills that were emplaced in the lower crust by magmatic underplating during Precambrian time. Furthermore, the lower crust and mafic sills were later deformed from Ural mountain building processes during Paleozoic time. The sills and lower crust were flexed and pushed below ~50 km depth where conditions favor the formation of eclogite. The eclogitization of the lower crust and mafic sills is interpreted to be responsible for the non-reflective Moho (Figure 57). A distinct transition from the reflective to diffuse, non-reflective Moho has been observed.

Overall, this study supports the hypothesis that the southern Ural Mountains have remained laregly unextended since their formation. The depressed, dipping geometry of the Moho beneath the fold and thrust belt has been confirmed by reprocessing and

analysis of seismic reflection data. Additionally, the presence of vertically layered, non-reflective eclogite is consistent with an unextended orogeny.

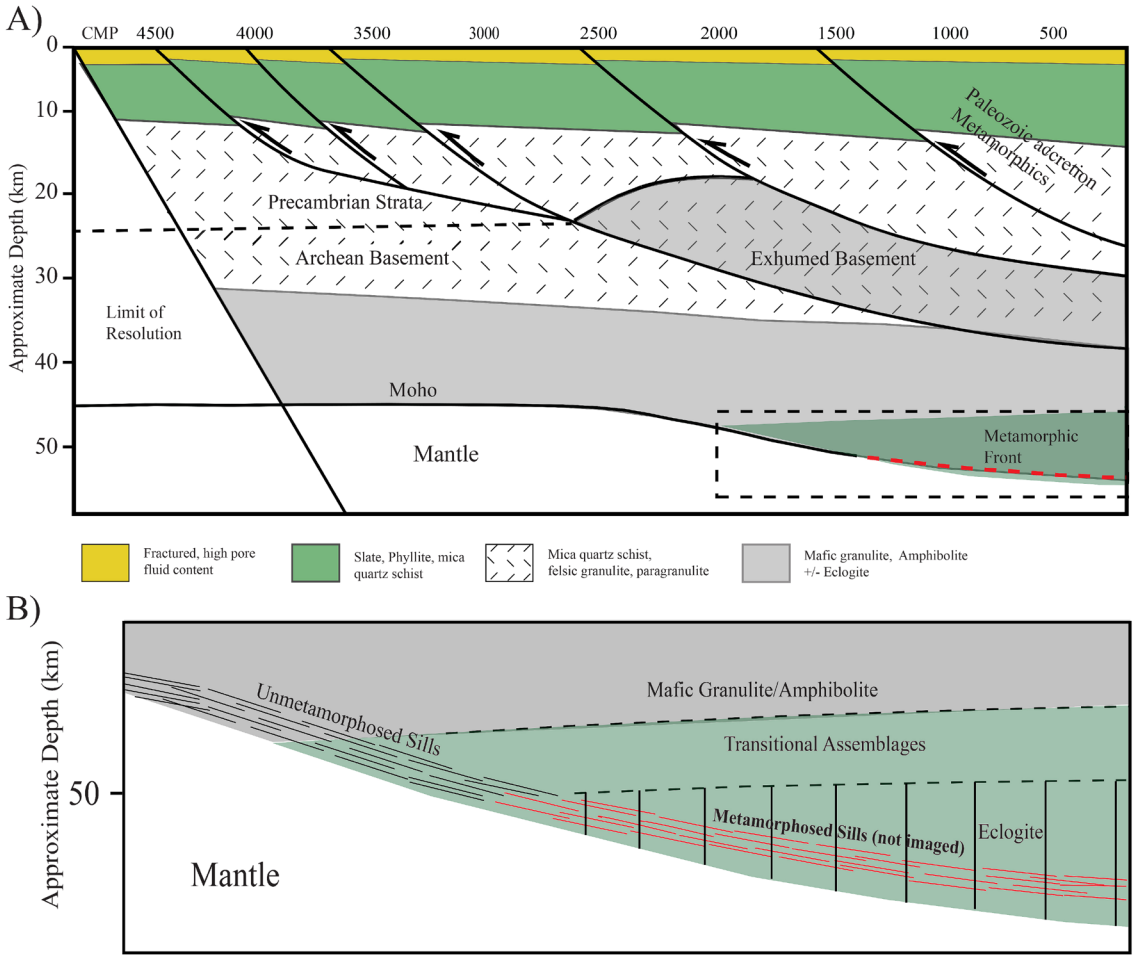

Figure 57. Final interpretations of the crust and Moho beneath the West Ural fold and thrust belt. A) New interpretations of the geologic cross–section for the fold and thrust belt (modified after Brown et al., 2003, 2008). The crustal mafic granulite/amphibolite is shown to terminate at the reflection Moho. B) The metamorphic front has been enlarged to show details of the mafic sills and rock composition of this region (Based on Ryan and Dewey, 1997; Brown et al., 2003, 2008).

REFERENCES

Alvarez-Marron, J., 2002, Tectonic processes during collisional orogenesis from comparison of the Southern Urals with the Central Variscides. In: Brown, D., Juhlin, C., Puchkov, V. (Eds.), Mountain Building in the Uralides: Pangea to Present: Geophysical Monograph, American Geophysical Union, v. 132, , p. 83–100.

Austrheim, H., 1991, Eclogite formation and dynamics of crustal roots under continental collision zones: Terra Nova, v. 3, p. 492-499.

Balling, N., 2000, Deep seismic reflection evidence for ancient subduction and collision zones within the continental lithosphere of northwestern Europe: Tectonophysics, v. 329, p. 269-300.

Baird, D.J., J.H. Knapp, D.N. Steer, L.D. Brown, and K.D. Nelson, 1995, Upper-mantle reflectivity beneath the Williston Basin, phase-change Moho, and the origin of intracratonic basins: Geology, v. 5, p. 431-434.

BABEL Working Group, 1990, Evidence for early Porterozoic plate tectonics from seismic reflection profiles in the Baltic Shield: Nature, v. 348, p. 34-38.

Berzin, R., Oncken, O., Knapp, J.H., Pérez-Estaún, A., Hismatulin, T., Yunusov, N., and Lipilin, A., 1996, Orogenic Evolution of the Ural Mountains: Results from an Integrated Seismic Experiment: Science, v. 274, p. 220-221.

Brown, D., Alvarez-Marrón, J., Pérez-Estaún, A., Gorozhanina, Y., Baryshev, V., and Puchkov, V., 1997, Geometric and kinematic evolution of the foreland thrust and fold belt in the southern Urals: Tectonics, v. 16, p. 551-562, doi: 10.1029/97TC00815.

Brown, D., Alvarez-Marron, J., Perez-Estaun, A., Puchkov, V., and Ayala, C., 1999, Basement influence on foreland thrust and fold belt development: an example from the southern Urals: Tectonophysics, v. 308, p. 459-472.

Brown, D., Carbonell, R., Kukkonen, I., Ayala, C., and Golovanova, I., 2003, Composition of the Uralide crust from seismic velocity (V p, V s), heat flow, gravity, and magnetic data: Earth and Planetary Science Letters, v. 210, p. 333-349.

Brown, D., Alvarez-Marron, J., Perez-Estaun, A., Gorozhanina, Y., and Puchkov, V., 2004, The structure of the south Urals foreland fold and thrust belt at the transition to the Precaspian Basin: Journal of the Geological Society, v. 161, p. 813-822, doi: 10.1144/0016-764903-174.

Brown, D., Juhlin, C., Ayala, C., Tryggvason, A., Bea, F., Alvarez-Marron, J., Carbonell, R., Seward, D., Glasmacher, U., Puchkov, V., and Perez-Estaun, A., 2008, Mountain building processes during continent–continent collision in the Uralides: Earth-Science Reviews, v. 89, p. 177-195.

Bousquet, R., Goffé, B., Henry, P., Le Pichon, X., and Chopin, C., 1997, Kinematic, thermal, and petrological model of the Central Alps: Lepontine metamorphism in the upper crust and eclogitisation of the lower crust: Tectonophysics, v. 273, p. 105-127.

Carbonell R., A. Perez-Estaun, J. Gallart, J. Diaz, S. Kashubin, J. Mechie, R. Stadtlander, A. Schultze, J. H. Knapp and A. Morozov, 1996, Crustal root beneath the Urals: Wide-angle seismic evidence: Science, v. 274, p. 222-224.

Carbonell, R., Lecerf, D., Itzin, M., Gallart, J., and Brown, D., 1998, Mapping the Moho beneath the southern Urals with wide-angle reflections: Geophysical Research Letters, v. 25, p. 4229-4232.

Carbonell, R., Gallart, J., Perez-Estaun, A., Diaz, J., Kashubin, S., Mechie, J., Wenzel, F., Knapp, J., 2000, Seismic wide-angle constraints on the crust of the Southern Urals: Journal of Geophysical Research, v. 105, p. 13755–13777.

Chemenda, A., Matte, P., and Sokolov, V., 1997, A model of Palaeozoic obduction and exhumation of high-pressure/low-temperature rocks in the southern Urals: Tectonophysics, v. 276, p. 217-227.

Christensen, N., and Mooney, W., 1995, Seismic velocity structure and composition of the continental crust: A global view: Journal of Geophysical Research: Atmospheres, p. 9761-9788.

Cook, F. A., D. S. Albaugh, L. D. Brown, S. Kaufman, J. E. Oliver and R. D. Hatcher, Jr., 1979, Thin-skinned tectonics in the crystalline southern Appalachians; COCORP seismic reflection profiling of the Blue Ridge and Piedmont: Geology, v. 7, p. 563-567.

Cook, F. A., White, D. J., Jones, A. G., Eaton, D. W., Hall, J., & Clowes, R. M., 2010, How the crust meets the mantle: Lithoprobe perspectives on the Mohorovičić discontinuity and crust–mantle transition: Canadian Journal of Earth Sciences, v. 47(4), p. 315-351.

Cox, M.J., 1999, Static Corrections for Seismic Reflection Surveys: Tulsa: Society of Exploration Geophysicists, v. 9.

Clowes, R.M., Burianyk, M.J.A., Gorman, A.R., et al., 2002, Crustal velocity structure from SAREX, the Southern Alberta Refraction Experiment: Canadian Journal of Earth Sciences, v. 39, p. 351–373.

Diaconescu, C.C., and Knapp, J.H., 2002, Role of a Phase: Change Moho in Stabilization and Preservation of the Southern Uralide Orogen, Russia, Mountain Building in the Uralides: Pangea to the Present: American Geophysical Union, p. 67-82.

Diakonova, A.G., Ivanov, K.S., Astafiev, P.F., Vishnev, V.S., and Konoplin, A.D., 2007, Resistivity pattern of crust and upper mantle in Southern Urals: Russian Geology and Geophysics, v. 48, p. 844-850, doi: http://dx.doi.org/10.1016/j.rgg.2007.09.005.

Eaton, D.W., 2006, Multi-genetic origin of the continental Moho: insights from Lithoprobe: Terra Nova, v. 18, p. 34-43, doi: 10.1111/j.1365-3121.2005.00657.x.

Echtler, H. P., M. Stiller, F. Steinhoff, A. Suleimanov, J. H. Knapp and J. Alvarez-Marron, 1996, URSEIS '95 Crustal architecture of the southern Urals by vibroseis CMP-profiling: Science, v. 274, p. 224-226.

Fichter, L.S., 2000, The Wilson Cycle and a Plate Tectonic Rock Cycle: (http://csmres.jmu.edu/geollab/fichter/Wilson/Wilson.html 2/24/2014).

Fountain, D. M., T. M. Boundy, H. Austrheim and P. Rey, 1994, Eclogite-facies shear zones deep crustal reflectors: Tectonophyics, v. 232, p. 411-424.

Furlong, K.P., and Fountain, D.M., 1986, Continental crustal underplating: Thermal considerations and seismic petrologic consequences: Journal of Geophysical Research: Solid Earth (1978–2012), v. 91, p. 8285-8294.

Fyfe, W.S., 1978, Evolution of Earth's crust — modern plate tectonics to ancient hot spot tectonics: Chemical Geology, v. 23, p. 89–114.

Fyfe, W.S., 1986, Fluids in Deep Continental Crust, in Reflection Seismology: The Continental Crust: American Geophysical Union, p. 33-39.

Fyfe, W.S., 1992, Magma underplating of continental-crust: Journal of Volcanology and Geothermal Research, v. 50, p. 33–40.

Gray, S.H., Maclean, G., and Marfurt, K.J., 1999, Crooked line, rough topography: advancing towards the correct seismic image: Geophysical Prospecting, v. 47, p. 721-733, doi: 10.1046/j.1365-2478.1999.00143.x.

Hamilton, W., 1970, The Uralides and the motion of the Russian and Siberian platforms: Geologic Society of America Bulletin, v. 81, p. 2553-2576.

Henstock, T. J., A. Levander, C. M. Snelson, G. R. Keller, K. C. Miller, S. H. Harder, A. R. Gorman, R. M. Clowes, M. J. A. Burianyk and E. D. Humphreys, 1998, Probing the Archean and Proterozoic lithosphere of western North America: GSA Today, v. 8, p. 1-5.

Hynes, A. and D. B. Snyder, 1995, Deep-crustal mineral assemblages and potential for crustal rocks below the Moho in the Scottish Caledonides: Geophysical Journal International, v. 123, p. 323-339.

Jarchow, C.M., G.A. Thompson, R.D. Catchings, and W .D. Mooney, 1993, Seismic evidence for active magmatic underplating beneath the Basin and Range Province, western United States: Journal of Geophyics Research: Solid Earth, v. 8, p. 22095-221081.

Jones, A.G., 1992, Electrical conductivity of the continental lower crust. In Continental lower crust. Edited by D.M. Fountain, R.J. Arculus, and R.W. Kay. Elsevier, Amsterdam: the Netherlands, Chapter 3, p. 81–143.

Jones, A.G., and Ferguson, I.J., 2001, The electric Moho: Nature, v. 409(6818), p. 331–333, doi:10.1038/35053053. PMID:11201739.

Juhlin, C., Brown, D., Rybalka, A., and Petrov, G., 2007, Moho imbrication in the Middle Urals: Terra Nova, v. 19, p. 189-194, doi: 10.1111/j.1365-3121.2007.00733.x.

Kashubin, S., Juhlin, C., Friberg, M., Rybalka, A., Petrov, G., Kashubin, A., Bliznetsov, M., and Steer, D., 2006, Crustal structure of the Middle Urals based on seismic reflection data: Geological Society of London, Memoirs, v. 32, p. 427-442.

Kissling, E., 1993, Deep structure of the Alps—what do we really know?: Physics of the Earth and Planetary Interiors, v. 79, p. 87-112, doi: http://dx.doi.org/10.1016/0031-9201(93)90144-X.

Klemperer, S.L., Hauge, T.A., Hauser, E.C., Oliver, J.E., and Potter, C.J., 1986, The Moho in the northern Basin and Range province, Nevada, along the COCORP 400N seismic reflection transect: Geological Society of America Bulletin, v. 97(5): p. 603–618. doi:10.1130/0016-7606(1986).

Knapp, J.H., D.N.Steer, L.D.Brown, R.Berzin, A.Suleimanov, M.Stiller, E.Ltischen, D.Brown, R.Bulgakov, and A.V.Rybalka, 1996, A lithosphere-scale image of the Southern Urals from explosion-source seismic reflection profiling in URSEIS'95: Science, 274, p. 226-228.

Knapp, J., Diaconescu, C.C., Bader, M., Sokolov, V., Kashubin, S., and Rybalka, A., 1998, Seismic reflection fabrics of continental collision and post-orogenic extension in the Middle Urals, central Russia: Tectonophysics, v. 288, p. 115-126.

Kukkonen, LT., L V. Golovanova, Y. V. Khachay, V. S. Druzhinin, A M. Kosarevand V. A., 1997, Schapov, Low geothermal heat flow of the Urals fold belt – implication of low heat production, fluid circulation or palaeoclimate?: Tectonophysics, v. 276, p. 63-85.

Laubscher, H., 1990, The problem of the Moho in the Alps: Tectonphysics, v. 182, p. 9-20.

Marquez, J., 2014, Seismic Interpretation; Reflection Seismics, v. 1, p. 65-69, http://dqwl.yangtzeu.edu.cn/maonb/jxnr/shuangyu/P79-82.pdf.

Marshak, S., 2011, Earth: Portrait of a Planet: New York, W. W. Norton & Company.

Matte, P., 2006, The Southern Urals: deep subduction, soft collision and weak erosion: Geological Society, London, Memoirs, v. 32, p. 421-426, doi: 10.1144/GSL.MEM.2006.032.01.25.

McBride, J.H., White, R.S., Smallwood, J.R. and England, R.W., 2004, Must magmatic intrusion in the lower crust produce reflectivity?: Tectonophysics, p. 388, doi. 10.1016/j.tecto.2004.07.055.

Meissner, R., T. Wever and R. Bittner, 1987, Results of DEKORP 2-S and other reflection profiles through the Variscides: Geophysics: Journals, Royal Astronomy Society, v. 89, p. 319-324.

Nedimovic, M.R., and West, G.F., 2003, Crooked-line 2D seismic reflection imaging in crystalline terrains: Part 1, data processing: Geophysics, v. 68, p. 274-285.

Nelson, K. D., J. H. McBride, J. A. Arnow, D. M. Wille, L. D. Brown, J. E. Oliver and S. Kaufman, 1987, Results of recent COCORP profiling in the Southeastern United States: Geophysics: Journals, Royal Astronomy Society, v. 89, p. 141-146.

Nelson, K.D., 1991, A unified view of craton evolution motivated by recent deep seismic reflection and refraction results: Geophysics Journal International, v. 105, p. 5-35.

Németh, B., Hajnal, Z., and Lucas, S.B., 1996, Moho signature from wide-angle reflections: preliminary results of the 1993 Trans-Hudson Orogen refraction experiment: Tectonophysics, v. 264, p. 111-121.

Perez-Estaun, A., Alvarez-Marron, J., Brown, D., Puchkov, V., Gorozhanina, Y., Baryshev,V., 1997, Along-strike structural variations in the foreland thrust and fold belt of the southern Urals: Tectonophysics, v. 276, p. 265-280.

Puchkov, V.N., 2009, The evolution of the Uralian Orogeny: Geological Society of London, Special Publications, v. 327, p. 161.

Puchkov, V., 2013, Structural stages and evolution of the Urals: Mineralogy and Petrology, v. 107, p. 3-37.

Poli, S. and M. W. Schmidt, 1997, The high-pressure stability of hydrous phases in orogenic belts: an experimental approach on eclogite-forming processes: Tectonophysics, v. 273, p. 169-184.

Prussen, E.I., 1991, The reflection Moho along the COCORP northwest U.S. transect, in Continental Lithosphere: Deep seismic Reflections: Geodynamics Ser., v. 22, edited by R. Meissner et al., American Geophyscial Union, Washington, D. C., p. 315-322.

Ryan, P., and Dewey, J., 1997, Continental eclogites and the Wilson Cycle: Journal of the Geological Society, v. 154, p. 437-442.

Schreyer W. and B. Stockhert, 1997, High-Pressure metamorphism in nature and experiment: Lithos, v. 41, p. 1-4.

Skripiy, A. A. and N. K. Yunusov, 1989, Tension and compression structures in the articulation zone of the Southern Urals and the East European Platform: Geotectonics, v. 23, p. 515-522.

Sokolov, V.B., 1992, Crustal structure of the Urals: Geotectonics, English Translation, v. 26, p. 357- 366.

Spadea, P., and D'Antonio, M., 2006, Initiation and evolution of intra-oceanic subduction in the Uralides: Geochemical and isotopic constraints from Devonian oceanic rocks of the Southern Urals, Russia: Island Arc, v. 15, p. 7-25, doi: 10.1111/j.1440-1738.2006.00514.x.

Spear, F. S., 1993, Metamorphic phase equilibria and pressure temperature-time paths: Monograph Series, International Mineral Society of America, Washington, D.C., p. 799.

Stadtlander, R., Mechie, J., and Schulze, A., 1999, Deep structure of the Southern Ural mountains as derived from wide-angle seismic data: Geophysical Journal International, v. 137, p. 501-515.

Steer, D.N., Knapp, J.H., Brown, L.D., and the URSEIS Working Group, 1996, Lithospheric evolution of the Urals: Mantle reflections of URSEIS '95: [abs.] Geologic Society of America: Abstract Program.

Steer, D.N., Knapp, J.H., Brown, L.D., Echtler, H.P., Brown, D.L., and Berzin, R., 1998, Deep structure of the continental lithosphere in an unextended orogen: An explosive-source seismic reflection profile in the Urals (Urals Seismic Experiment and Integrated Studies (URSEIS 1995)): Tectonics, v. 17, p. 143-157, doi: 10.1029/97TC03056.

Stein, Seth, Earth 202: Earth's Interior, 2014, http://www.earth.northwestern.edu/people/seth/202/new_2004/wilson_cycle.html.

Steinhart, J.S., 1967, Mohorovicic discontinuity: In International dictionary of geophysics. Edited by S.K. Runcorn: Pergamon Press, Oxford, UK, v. 2, p. 991–994.

Thouvenot, F., Kashubin, S.N., Poupinet, G., Makoviskiy, V.V., Kashubina, T.V., Matte, Ph., and Jenatton, L., 1995, The root of the Urals: evidence from wide angle reflection seismics: Tectonophysics, v. 250, p. 1-13.

Thybo, H., Maguire, P.K.H., Birt, C. and Perchue´ , E., 2000, Seismic reflectivity and magmatic underplating beneath the Kenya Rift: Geophysics Research Letters, v. 27, p. 2745–2748.

Thybo, H., and Artemieva, I.M., 2013, Moho and magmatic underplating in continental lithosphere: Tectonophysics, v. 609, p. 605-619.

Thybo, H., and Nielsen, C.A., 2012, Seismic velocity structure of crustal intrusions in the Danish Basin: Tectonophysics, v. 572, p. 64-75.

Tryggvason, A., Brown, D., and Pérez-Estaún, A., 2001, Crustal architecture of the southern Uralides from true amplitude processing of the Urals Seismic Experiment and Integrated Studies (URSEIS) vibroseis profile: Tectonics, v. 20, p. 1040-1052, doi: 10.1029/2001TC900020.

Warner, M. R., 1990a, Absolute reflection coefficients from deep seismic reflections: Tectonophysics, v. 173, p. 15-23.

Warner, M. R., 1990b, Basalts. water, or shear zones in the lower continental crust?: Tectonophysics, v. 173, p. 163-174.

White, R. S., 1988, The earth's crust and lithosphere: Journal of Petrology: Special Lithosphere Issue, p. 1- 10.

Yilmaz, O., 2001, Seismic data analysis, processing, inversion, and interpretation of seismic data: Tulsa, OK, Society of Exploration Geophysics.

Zonenshain, L. P., M. I. Kuzman and L. M. Natopov, 1990, Geology of the USSR: A plate-tectonic synthesis: Geodynamics, Ser. 21, American Geophysical Union, Washington, D.C., p. 25-54.

APPENDIX

INTERPRETATIONS

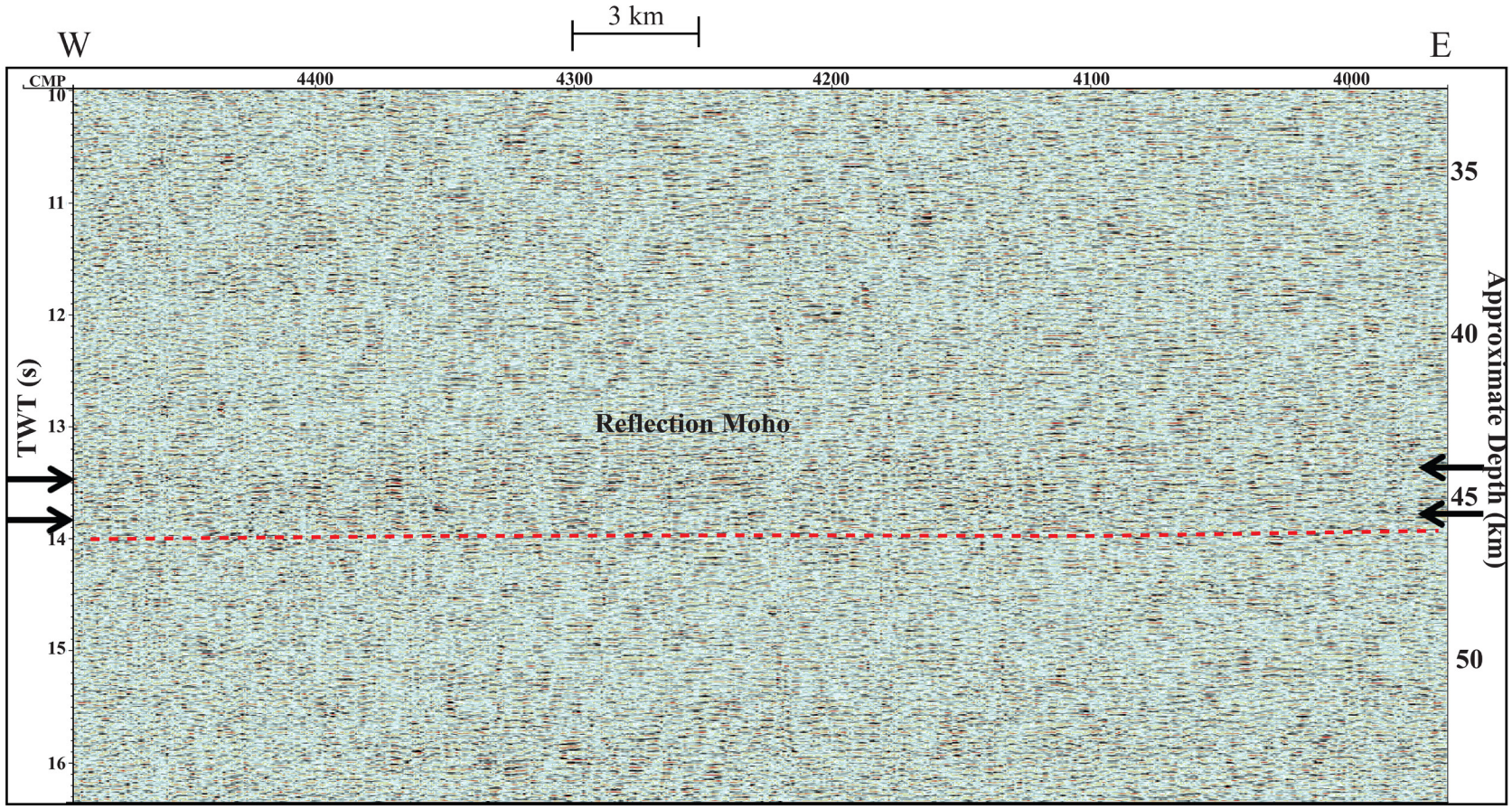

Figure A1. Zoomed image of the Moho beneath the western portion of the fold and thrust belt. The red dashed line at the base of the reflections represents the Moho boundary.

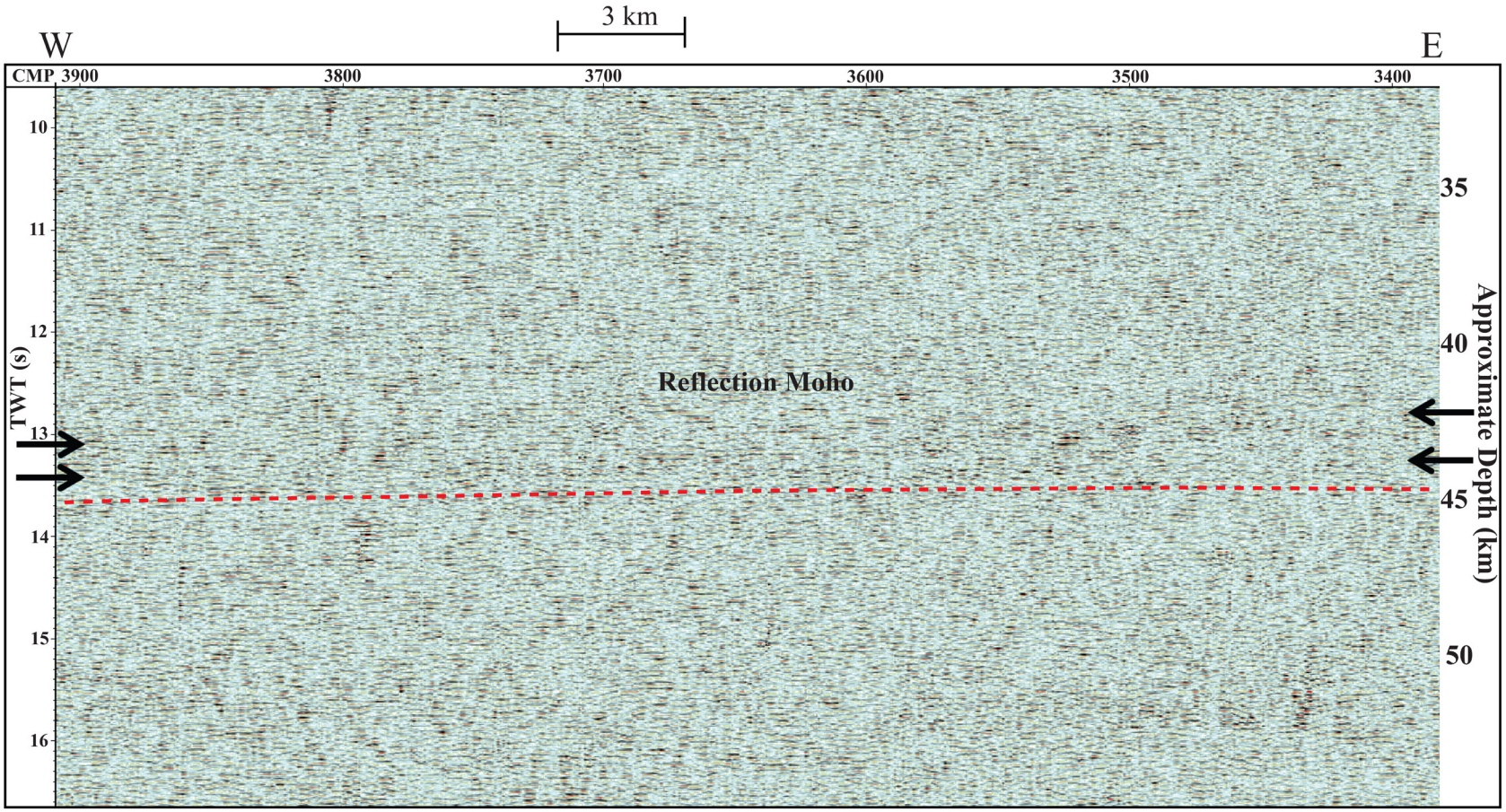

Figure A2. Zoomed image of the Moho beneath the western portion of the fold and thrust belt. The red dashed line at the base of the reflections represents the Moho boundary.

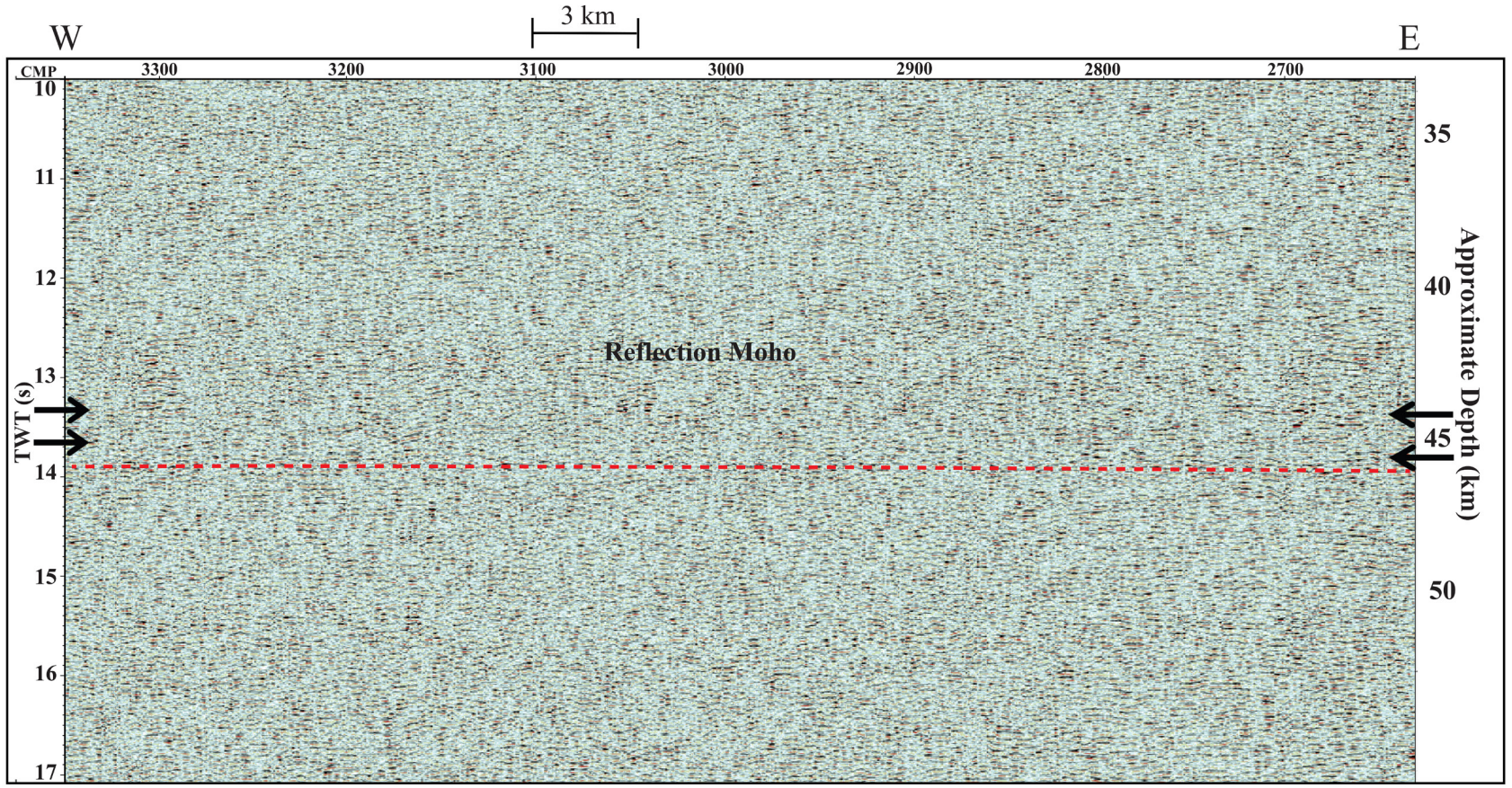

Figure A3. Zoomed image of the Moho beneath the west central portion of the fold and thrust belt. The red dashed line at the base of the reflections represents the Moho boundary.

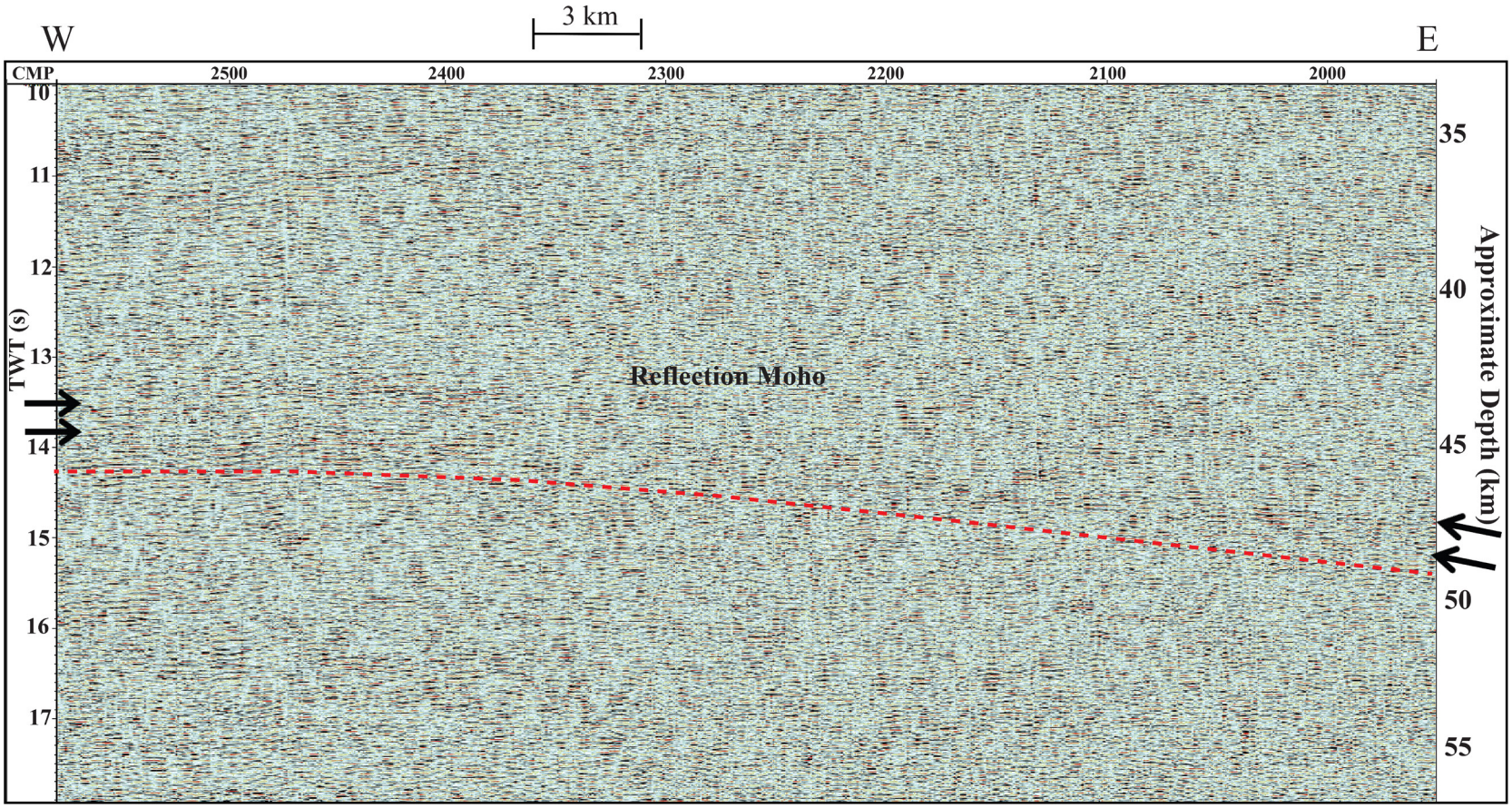

Figure A4. Zoomed image of the Moho beneath the east central portion of the fold and thrust belt. The red dashed line at the base of the reflections represents the Moho boundary.

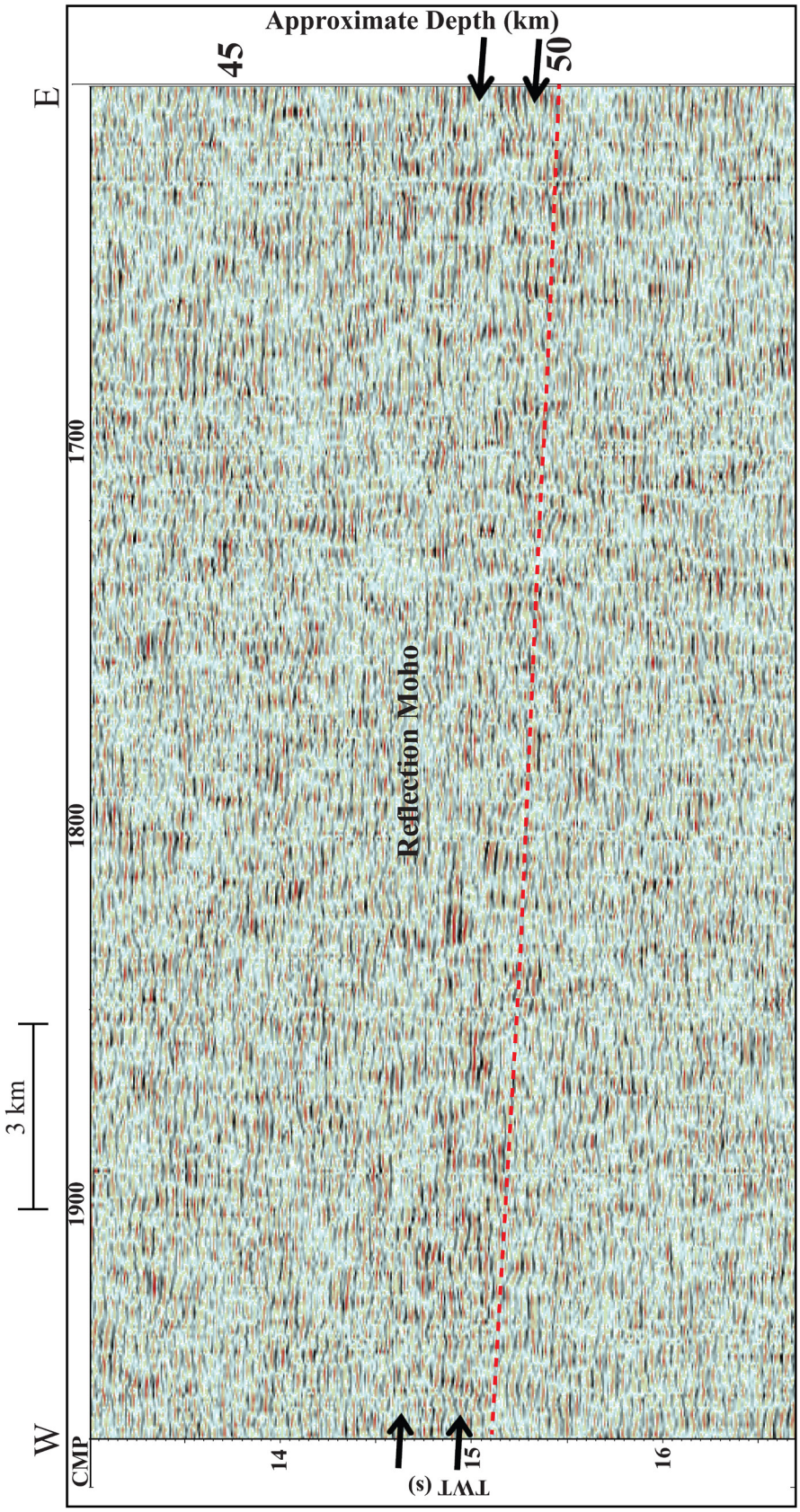

Figure A5. Zoomed image of the Moho beneath the eastern portion of the fold and thrust belt. The red dashed line at the base of the reflections represents the Moho boundary.

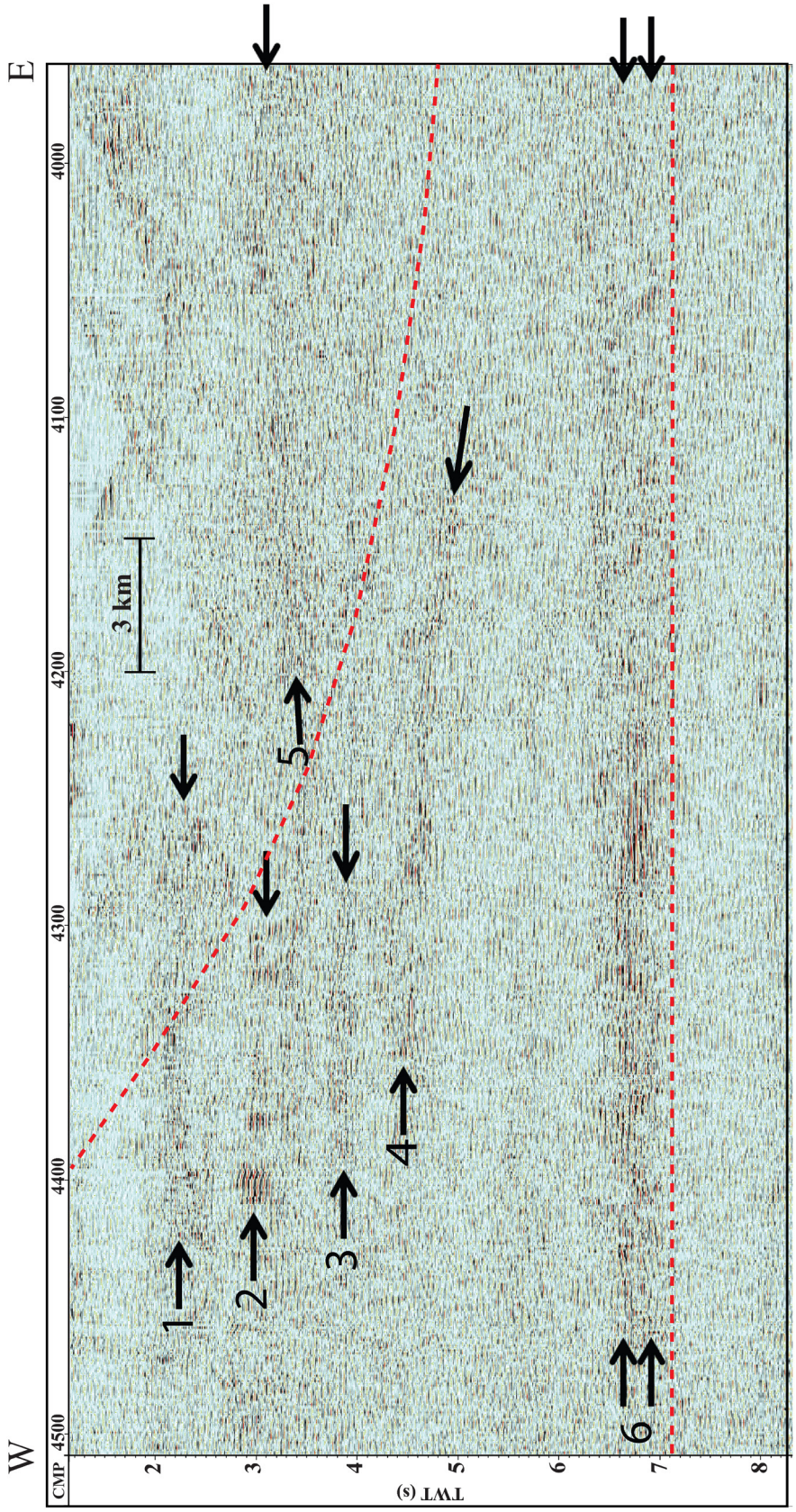

Figure A6. Interpretations of Box 1 from panel 1 of the stacked section. Red, dashed lines represent possible fault structures.

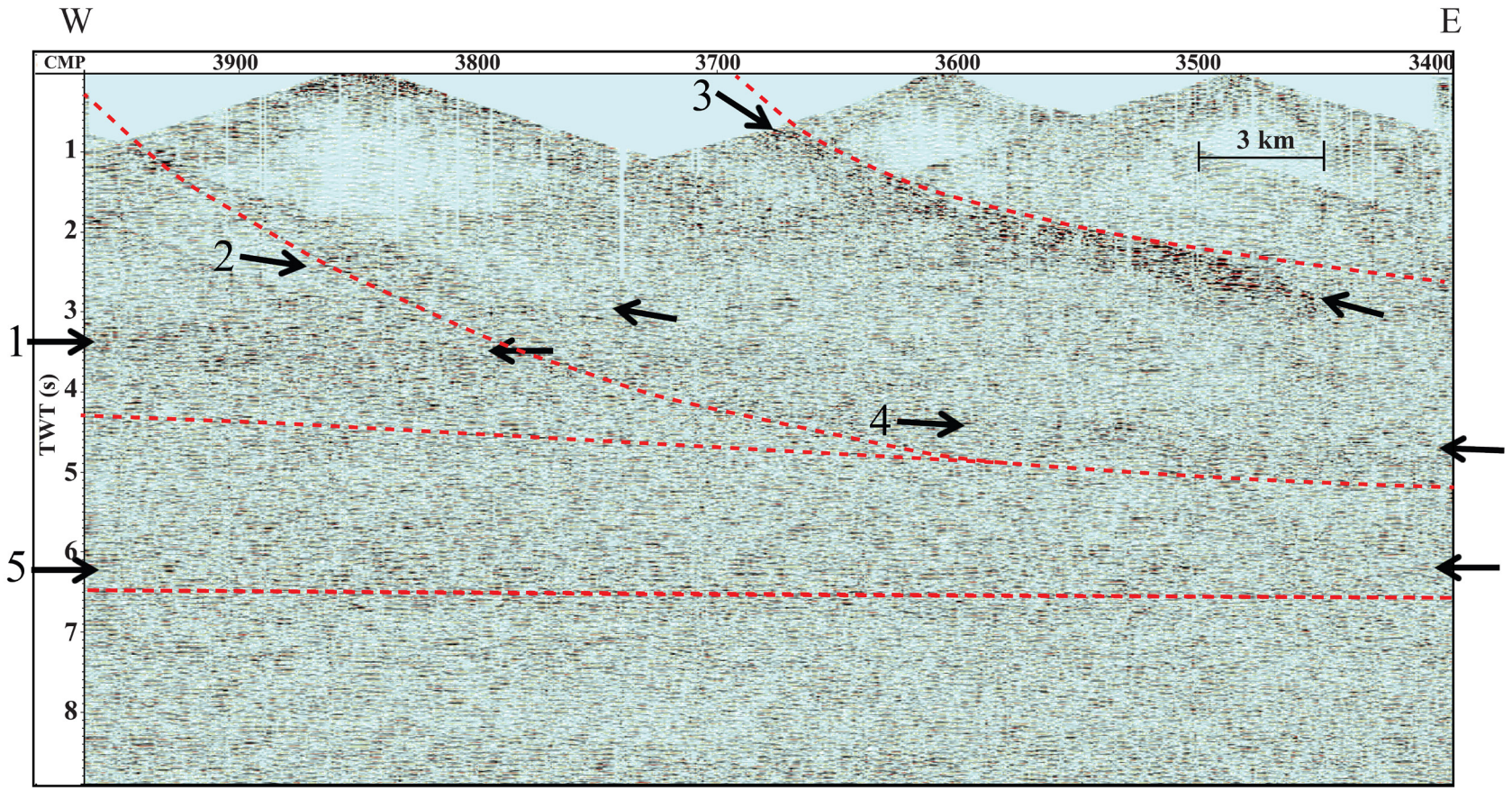

Figure A7. Interpretations of Box 2 from panel 1 of the stacked section. Red, dashed lines represent possible fault structures.

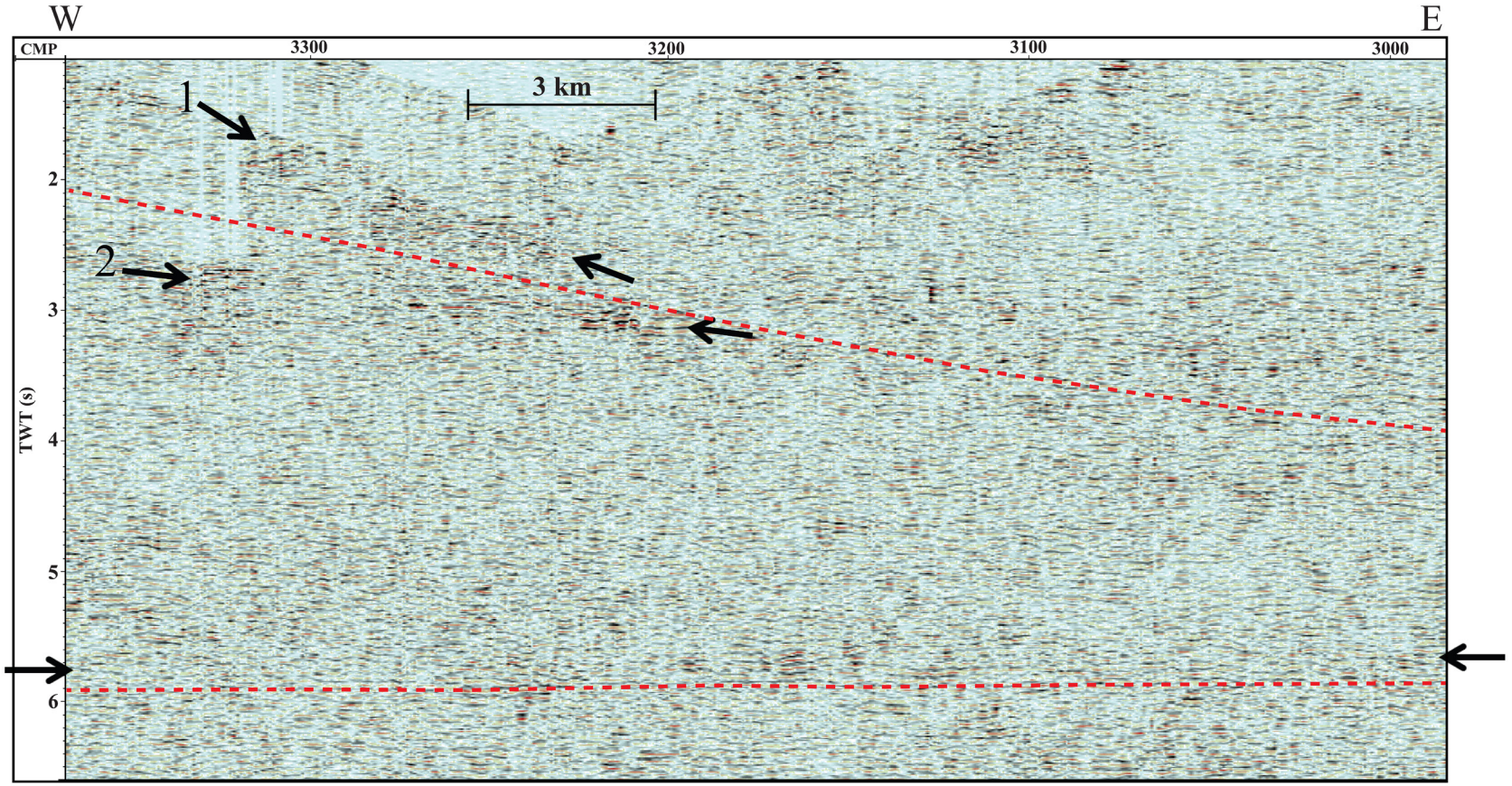

Figure A8. Interpretations of Box 1 from panel 2 of the stacked section. Red, dashed lines represent possible fault structures.

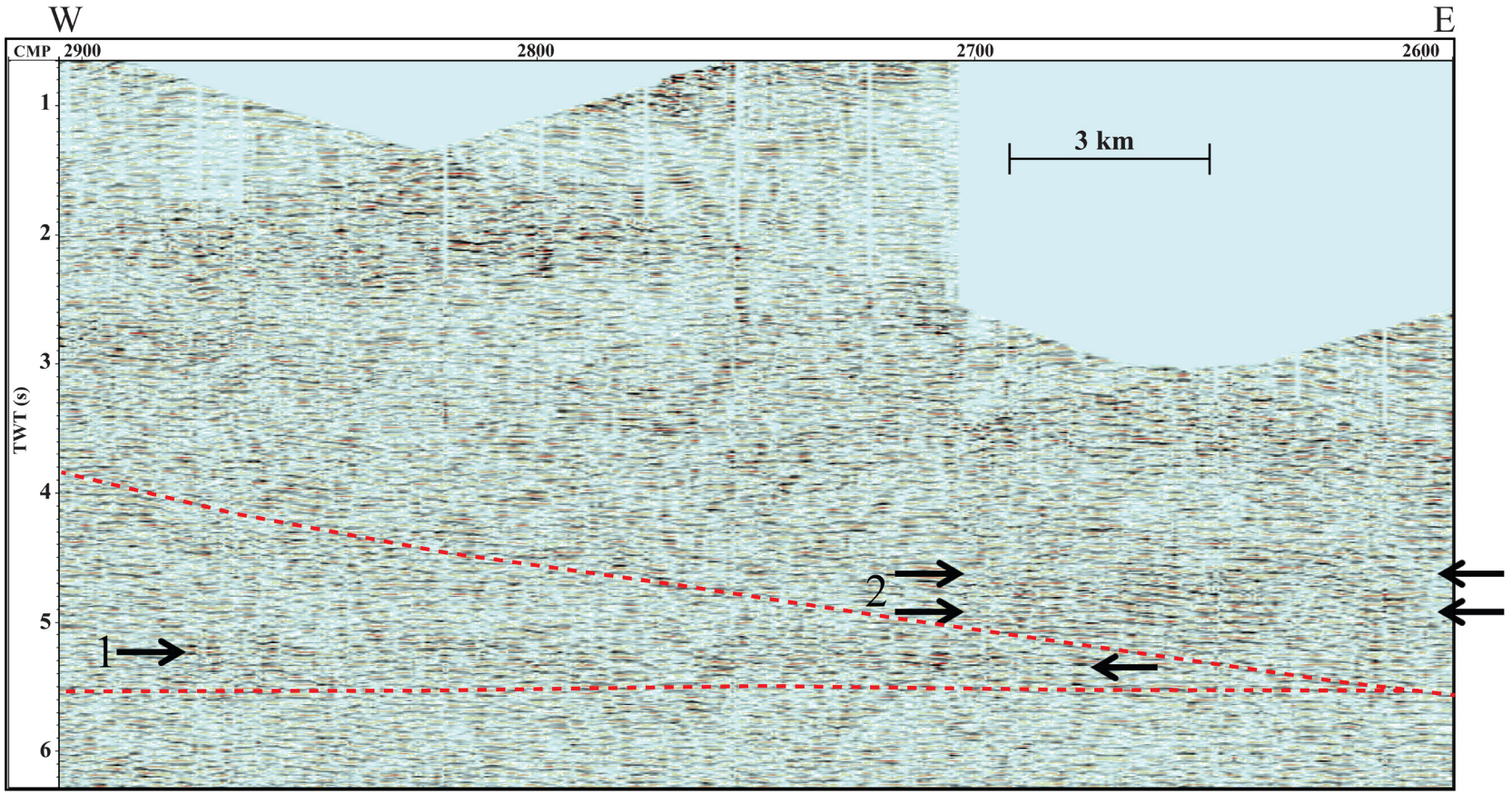

Figure A9. Interpretations of Box 2 from panel 2 of the stacked section. Red, dashed lines represent possible fault structures.

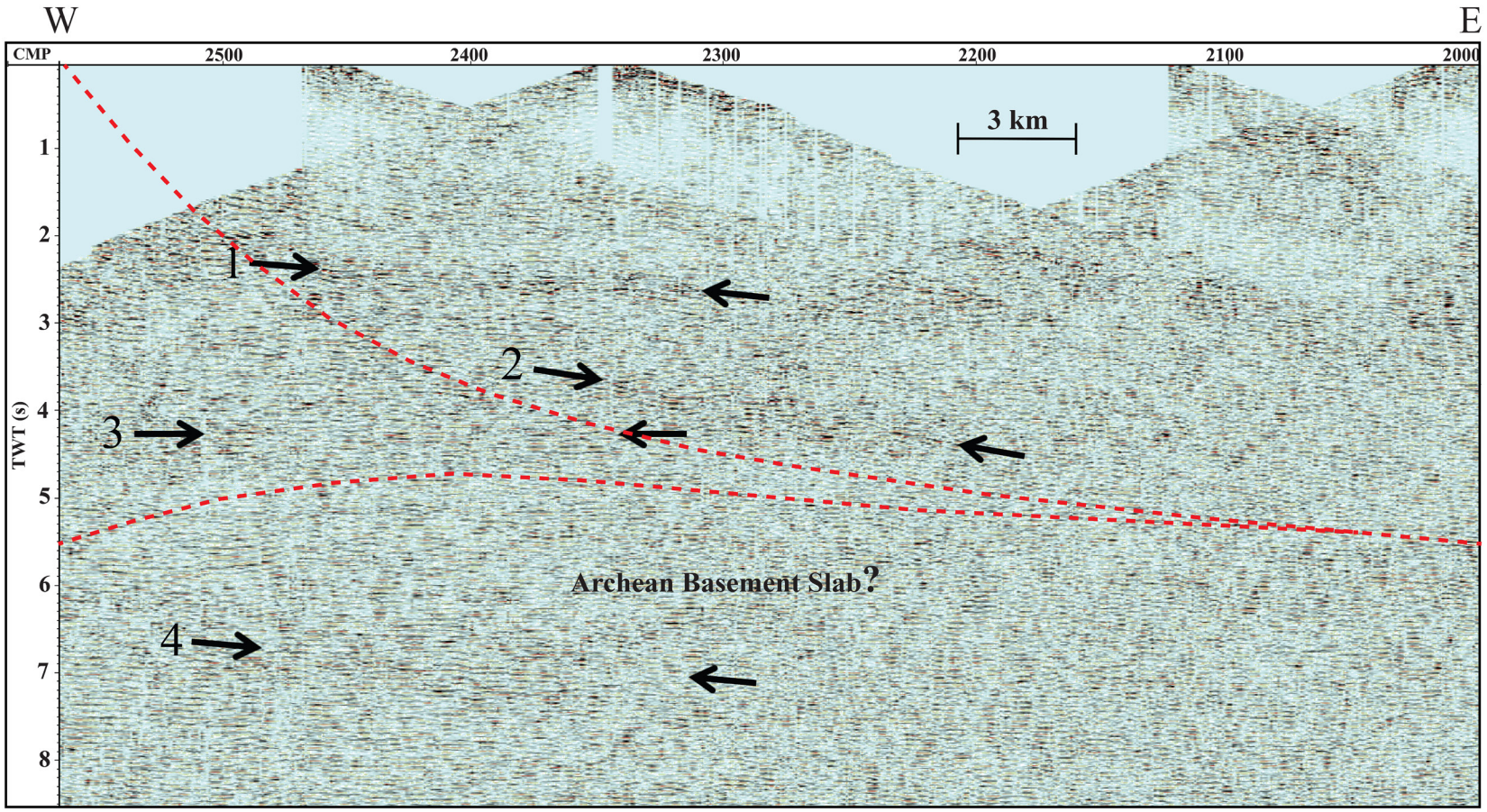

Figure A10. Interpretations of Box 3 from panel 2 of the stacked section. Red, dashed lines represent possible fault structures. The crust at less than 5 s TWT has been interpreted to be exhumed Archean basement which is consistent with previous interpretations (after Berzin et al., 1997).

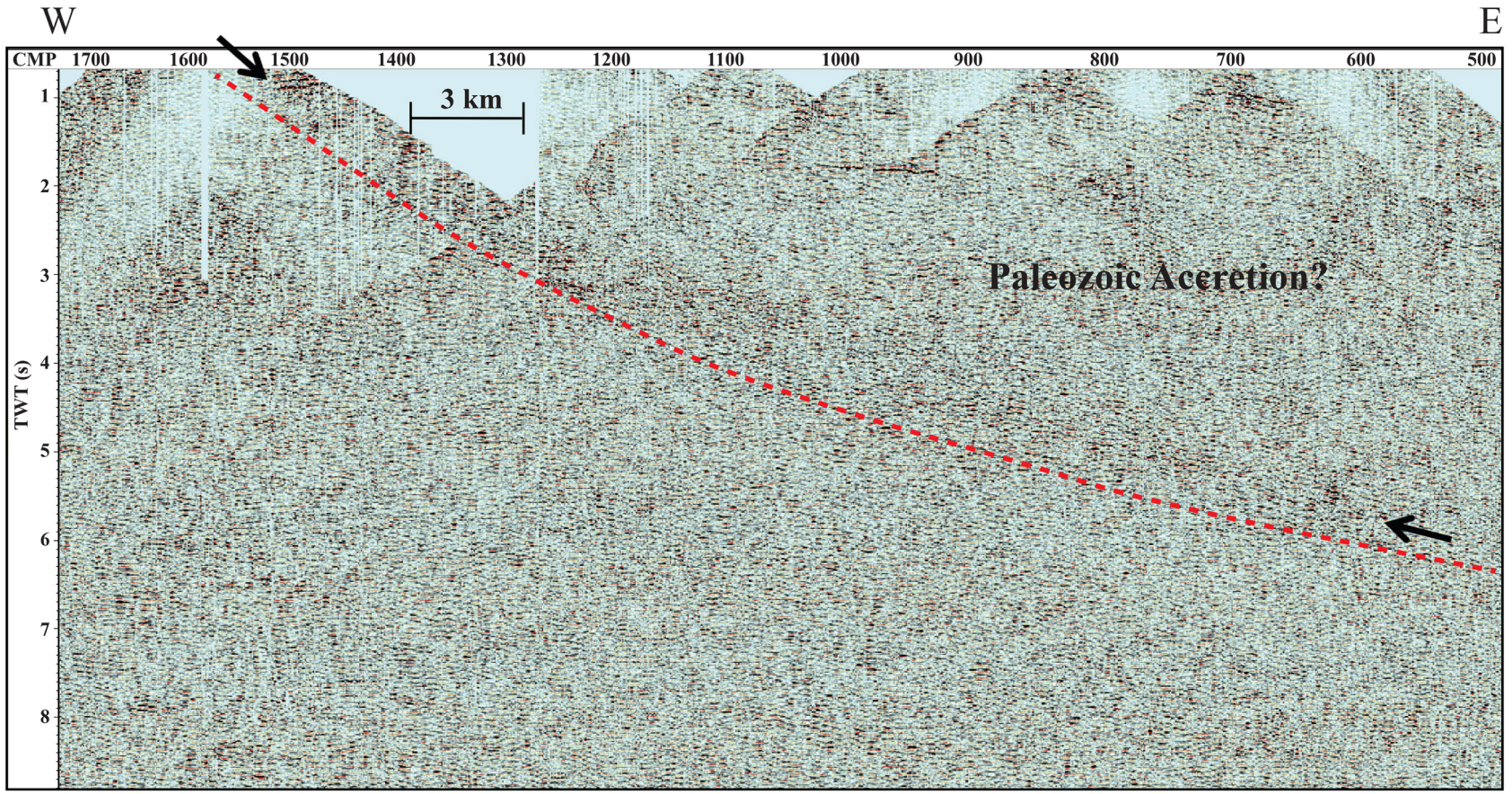

Figure A11. Interpretations of Box 1 from panel 3 of the stacked section. Red, dashed lines represent possible fault structures